The Pennsylvania State University

The Graduate School

College of Engineering

ULTRAFILTRATION OF HIGHLY CONCENTRATED MONOCLONAL ANTIBODY SOLUTIONS

A Dissertation in

Chemical Engineering

by

Elaheh Binabaji

Submitted in Partial Fulfillment
of the Requirements
for the Degree of

Doctor of Philosophy

May 2015

The dissertation of Elaheh Binabaji was reviewed and approved* by the following:

Andrew Zydney
Professor of Chemical Engineering
Dissertation Advisor
Chair of Committee

Themis Matsoukas
Professor of Chemical Engineering

Manish Kumar
Assistant Professor of Chemical Engineering

William Hancock
Professor of Bioengineering

Janna Maranas
Graduate Program Chair of the Department of Chemical Engineering

*Signatures are on file in the Graduate School

ABSTRACT

Monoclonal antibodies are currently the fastest growing segment of the pharmaceutical industry; these products are used in the treatment of a wide range of diseases including cancers and allergies. Antibody products are administered at high doses since the volume that can be delivered by injection is limited. Although ultrafiltration systems are used for final formulation of essentially all high value recombinant products, it is often challenging if not impossible to achieve the very high final formulation concentrations required for monoclonal antibody products. The overall objective of this thesis was to study and fundamentally understand the ultrafiltration behavior of highly concentrated monoclonal antibody solutions. This included: (1) evaluating the filtrate flux and maximum achievable antibody concentration during ultrafiltration of very high concentration (>200 g/L) antibody solutions, and (2) developing appropriate theoretical models to describe the ultrafiltration behavior in terms of independently measured biophysical properties of the antibody solution.

The osmotic pressure of a highly purified monoclonal antibody at concentrations up to 250 g/L was evaluated over a range of pH and ionic strength, and in the presence of specific excipients, using membrane osmometry. These data were used to calculate the second and third virial coefficients. The second virial coefficients were in good agreement with independent measurements from self-interaction chromatography using a newly developed approach to evaluate the column dead volume. The second virial coefficient was positive under all conditions, consistent with repulsive electrostatic interactions between the positively charged antibody molecules. In contrast, the third

virial coefficients were negative reflecting the presence of short-range attractive interactions between oppositely charged domains on adjacent proteins.

Viscosity data were obtained over a wide range of protein concentrations, solution pH, ionic strength, and in the presence of different excipients. The concentration parameter in the viscosity correlation appeared to be well-correlated with the values of the third virial coefficient, consistent with the importance of short range attractive interactions. The viscosity and osmotic pressure data were incorporated in a modified concentration polarization model that accounts for the effects of intermolecular protein-protein interactions in the highly-concentrated antibody solutions as well as the presence of a back-filtration phenomenon arising from the large pressure drop through the tangential flow filtration module. This model was in very good agreement with experimental data and was able to correctly predict the maximum achievable protein concentration during batch ultrafiltration experiments conducted over a wide range of conditions. These results provide important insights into the factors controlling the ultrafiltration behavior for highly concentrated antibody solutions as well as a framework for the development of improved ultrafiltration systems for use in bioprocessing applications.

TABLE OF CONTENTS

LIST OF FIGURES

LIST OF TABLES

ACKNOWLEDGEMENTS

First and foremost, I would like to thank my advisor, Dr. Andrew Zydney, for his valuable comments and inputs at all the stages of my doctoral study, his great encouragement and unlimited support. His help has been essential for the completion of this thesis and his mentorship has immeasurably influenced my personal development as a scientist. This has been nothing short of an incredible experience and I am forever amazed by his knowledge on such a wide range of topics and his ability to patiently help others. Thanks for always being so understanding during my graduate school days and I hope to have the great opportunity of collaborating with you in the future.

I would also like to thank my entire doctoral committee: Dr. Matsoukas, Dr. Kumar, and Dr. Hancock for their advice and encouragement throughout my studies, and for generously spending their time helping me to improve this work. I would also like to express my sincere gratitude to Dr. Borhan for all his invaluable help and support throughout my graduate study journey. Thanks for your incredible willingness to help. I am forever grateful for your advice and guidance.

During my studies at Penn State I have really enjoyed closely working with everyone in the Zydney research group. Particularly I want to thank Mahsa Rohani for teaching me the basics in lab – thanks for not only being an amazing friend through all these years but also for making me immediately feel part of the group. I would like to also especially thank Mahsa Hadidi for her friendship during these years and also for all the efforts to help me address our lab's safety issues during my time as safety officer. Since I have been back from my internship at MedImmune, it's been great to work with a

new group of lab-mates. I hope that I have been able to pass on some of what I've learned during my years working in the lab to the new members of the group. I have also enjoyed working with a number of very capable undergraduate students from the Chemical Engineering Department at Penn State, and I wish them all the best in their future careers. Specifically, I would like to thank Stephanie Nitopi for being such an amazing undergraduate researcher and for her contributions to Chapter 4 of this work. Thanks for all the things I learned by being your mentor and for many fun times both in the lab and otherwise. I wish you the best of luck both in your life and with your graduate studies at Stanford.

I also acknowledge the members of both the Curtis and the Kumar research group for giving me complete access to their laboratory equipment and for sharing their technical expertise. Specifically I would like to thank Trevor Zuroff in the Curtis research group for the time he spent to help me prepare for my comprehensive exam and his help regarding use of the HPLC system in their group. The administrative and technical staffs within the Chemical Engineering Department were extremely helpful. Many thanks to Mark Signs for his help using the equipment in the Fermentation Facility of the Huck Institutes of the Life Sciences. The rheology studies presented in Chapter 6 of this work not have been possible if it wasn't for the help of Dr. Ralph Colby in the Department of Materials Science and Engineering and his research group with using the RFSII system in their lab.

Funding for this work was provided by Amgen, Inc., and I have had the great opportunity of working with and benefiting from the guidance of our amazing collaborators at Amgen including Suma Rao and Junfen Ma which I am extremely

grateful for. Also, I would like to thank Amgen for the generous donation of the monoclonal antibody used in this work and Millipore for donation of the Pellicon 3 TFF cassettes and the membrane holder used in this work. I also received generous support from Penn State through the Walter L. Robb Family Chair.

None of this would have been possible without the constant encouragement and unlimited support of my dearest mom and dad, Zahra Nik hoosh and Mohammad Hossein Binabaji. I would never be where I am today without their lifelong love and guidance. My dad is my inspiration to continue my graduate studies in the United States and always pursuing my dreams, and my mom is my role model to patiently overcome the obstacles. Thank you both for everything you have done for me and for always believing in me. Thanks for always being there for me during the past 5.5 years that I was not able to see you and through both the good and the bad days of my graduate study journey. Thanks for trying to make each of those days better although I know it was even harder for you not being able to see me. I am truly blessed to have a wonderful sister and brother, Maryam and Soroosh, who I am indebted to for all their support and help over these years that I have been away from home. Thanks for being the most amazing siblings one can wish for and all the love and encouragement. Also, I would like to specially thank Arman Mirhashemi for his friendship and being such a constant source of inspiration. Thanks for being the best friend one can ever wish for and always making the time to listen to whatever I had to say and for being there for me and supporting me through this whole journey -- finishing this journey wouldn't have been possible without your help. Finally, I would like to thank Elnaz Kermani for being such a lovely friend and for making living in State College a whole lot easier for me.

Chapter 1

Introduction

1.1 Monoclonal Antibody Therapeutics

The past 3 decades have seen major developments in genetic engineering and recombinant DNA technology that have led to the production of a wide range of recombinant protein products that provide very targeted therapies with fewer side effects due to the unique biological activity and binding properties of these macromolecules. Protein therapeutics have been developed for the treatment of a wide range of diseases including AIDS, hepatitis, diabetes, arthritis, hemophilia, multiple sclerosis, cancer, infectious disease, cardiovascular ailments, etc. [1]. The early recombinant protein products were highly active hormones, cytokines, and clotting factors such as human growth hormone, α-, β-, and γ-interferons, thrombolytic agents, erythropoietin, and insulin. The first commercial recombinant human therapeutic, insulin (sold under the trade name Humulin®), was approved by the U.S Food and Drug Administration (FDA) in 1982 [2]. These bioproducts were used at relatively low doses and typically had annual production rates below 1 kg [3].

More recently, there has been a growing interest in the development of monoclonal antibody (mAbs) products due to their high target specificity in selectively binding to a target cell or molecule. In contrast to hormones (which are analogous to catalysts), antibodies act stoichiometrically and thus they require much higher dosing levels and batch sizes; current annual production requirements for some mAbs can be as high as 1000 kg. mAbs have been developed for the treatment of autoimmune disorders, solid and hematological cancers, allergies, and infectious diseases. mAbs act by activating immune system components, blocking receptors, or sequestering growth factors [4]. Current efforts are focused on antibody-drug conjugates in which the antibody provides the selective targeting while the conjugated drug provides the desired biological activity. From 1980 to 2005, a total of 206 unique therapeutic mAbs were studied in clinical trials with 12 anticancer mAbs approved for commercial use [5]. There are currently approximately 360 mAbs in clinical studies, with 30 in pivotal trials; more than 30 mAb therapeutics have already been approved for human use [6].

The market for monoclonal antibodies is the fastest growing segment of the pharmaceutical industry [7] with sales growing from less than $5 billion in 2000 to an expected level of $90 billion in 2017, giving a compound annual growth rate (CAGR) of 11.8%. The average development period from initiation of clinical studies to first U.S. approval was around 8.3 years for the 19 mAb products approved in the United States during the past decade (2004–2013) [8]. The key features of efficiency, quality, and safety required for successful commercialization and approval of mAb products are now well defined [9], leading to greater probability of clinical success and faster product development timelines than with other biopharmaceuticals.

Monoclonal antibodies (mAbs) are generally expressed in mammalian cell lines to obtain the correct glycosylation pattern and 3-dimensional structure. Continual advances in cell culture technology, including improvements in media for both the growth and production phase, feeding strategies, process design and control, and host cell engineering, have resulted in significant increases in product titers. Current mAbs are produced at concentrations of 3—5 g/L [10], which is an order of magnitude higher than typical titers of just a decade ago. Titers as high as 9.8 g/L have been achieved with a recombinant Chinese Hamster Ovary (CHO) line in a 21 day culture period [11].

The downstream purification process is designed to remove a wide range of undesired contaminants including cell debris, DNA, and host cell proteins (HCP). Current FDA criteria for final product purity recommend a final HCP concentration less than 10 ppm (part per million based on the mAb product), final DNA concentration less than 10 ng per dose of drug, and a final virus levels of less than 1 virus particle per million doses [12].

In order to achieve the high purity required for mAb products, a series of purification steps are used, each targeted to remove different classes of impurities. Figure 1.1 shows a schematic overview of a typical (consensus) process flowsheet used in downstream purification of monoclonal antibodies. The first step involves removal of cell debris and other large particulates, which is usually achieved by centrifugation often in combination with depth filtration (possibly using an added flocculation step). The next step is product recovery (or capture), which is most commonly achieved using protein A affinity chromatography. The eluted product from the protein A step is then subjected to different chromatography techniques for final polishing, e.g., ion-exchange

chromatography, hydrophobic interaction chromatography, and / or metal affinity mixed mode chromatography (e.g., using ceramic hydroxyapatite resin). A more detailed review of chromatography techniques used for bioseparations is provided by Jungbauer [13]. Virus clearance is usually achieved by a combination of pH inactivation and virus filtration. This purified stream is then formulated in an ultrafiltration / diafiltration system to place the molecule into the desired formulation buffer, achieve the desired final product concentration, and remove any small molecule impurities (e.g., buffer components used in previous chromatographic steps).

In 1997 Clark and Blanch [12] estimated that up to 80% of the total manufacturing cost is attributed to downstream purification processes while in 2001 Ladisch [14] reported this value to be 50-60%. This improvement could be partially due to recent advances in expression titers in the cell culture media [11] and developments in purification technologies. Model calculations presented by Kelly [11] indicate that the cost of production for a 1 g dose of an antibody product had decreased from approximately $134 in the 1990's to only $26 in 2007. These trends demonstrate that advances in production and purification technologies can have a significant affect on the cost of production and in turn the ability to make drug products available to more patients who need these therapeutic molecules.

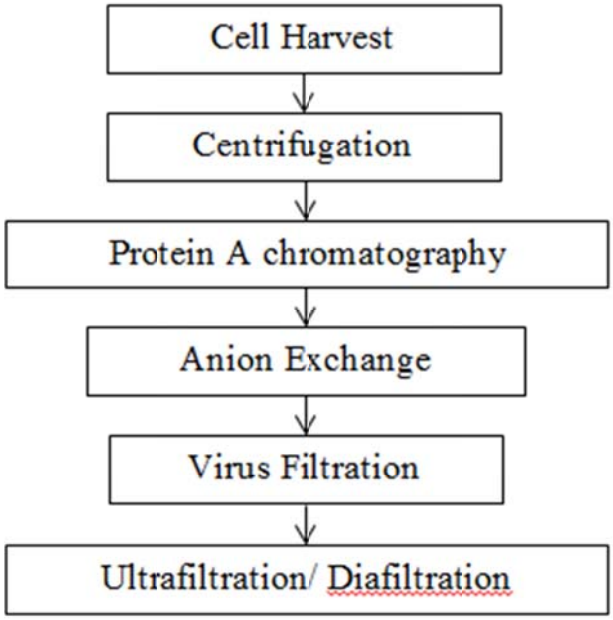

Figure 0.1 Typical process flow diagram for a mAb purification process (adapted from Kelly [11]).

One of the ongoing challenges in the production of mAb products is the difficulty in achieving the high final concentration needed for these products. mAbs are administered at high doses (defined as mg mAb/kg patient body weight) [15] via subcutaneous injection (SC) to achieve the desired therapeutic effect. The limited volume that can be delivered via SC injection (1-2 mL) has led to formulation of these products at very high concentrations, on the order of 100-200 g/L, and even higher concentrations are likely to be encountered in the future. Higher concentrations (and the correspondingly lower volumes) are also advantageous for intermediate solutions obtained throughout downstream processing due to easier and lower cost handling and storage [16, 17]. However, the high solution viscosity, protein instability, and very low filtrate flux have

created a range of problems in formulation and handling of these highly concentrated antibody products [17, 18].

1.2 Membrane Systems in Downstream Purification

Membrane processes have been used for bioseparations since well before the start of the modern membrane industry [19], and they played a major role in the purification of even the earliest biotechnology products [12, 20]. These processes are well suited for the biotechnology industry since they are robust, high throughput, easy to scale up, and they operate under mild conditions causing little degradation/denaturation of high value biological products [21]. Initially, the membrane processes used in the biotechnology were directly adopted from technology originally developed for other industries such as food processing [22]. Over the past 3 decades new membranes, modules, and membrane systems have been developed to specifically meet the requirements of the biotechnology industry. These developments have been facilitated by an improved fundamental understanding of mass transport during ultrafiltration and the effect of electrostatic interactions and concentration polarization on protein transmission [3].

Most membranes used in bioprocessing are produced from organic polymers such as polyamide, polysulfone, polyethersulfone, cellulose derivatives, and polyvinylidene fluoride. Regenerated cellulose membranes are extensively used for bioseparations since they are very hydrophilic, which leads to low levels of protein adsorption, fouling, and product denaturation. However, they are less stable to extremes of pH, cleaning agents, and temperature [21].

The most commonly used membrane processes for bioseparations are pressure-driven ultrafiltration, microfiltration, and virus filtration, all of which effect separations based primarily on the size of the product and impurities. Microfiltration membranes have pore size of 0.05 – 1 μm and are used for initial clarification to remove cells and cell debris while allowing protein and smaller molecules to pass through the membrane. Microfiltration involves a surface filtration in which the retained species are fully excluded from the membrane. In contrast, depth filtration systems retain undesired components throughout their porous structure by both adsorptive and size-based retention mechanisms [19]. Virus clearance is achieved by application of specifically designed membranes (virus filters) that have pore size between 20 and 70 nm. Ultrafiltration membranes have pore size between around 1 – 20 nm and are designed to provide high retention of proteins and other macromolecules.

The most commonly used technique for final formulation (buffer exchange) and concentration of essentially all recombinant protein products is ultrafiltration. Ultrafiltration was initially developed in the 1920's. John D. Ferry's review article in 1936 described the use of membrane technology for enzyme concentration, preparation of cell (and protein) free ultrafiltrates from biological solutions, analysis of bacteriophages and viruses, and sterile filtration [23]. However, the widespread use of ultrafiltration didn't start until the late 1960's with commercialization of asymmetric ultrafiltration membranes [21]. These asymmetric (anisotropic) membranes were able to overcome the major shortcomings of previous membranes by simultaneously increasing the permeate flux and mechanical stability. The thin skin layer at the upper surface has pores that provide the membrane its selectivity to achieve the desired separation while the support

layer underneath the skin has an open structure (larger pore size) that provides the required mechanical stability. This asymmetric structure gives the membrane much less resistance to filtration compared to isotropic (homogenous) membranes.

Commercial ultrafiltration systems are operated in cross flow mode, which is also known as tangential flow filtration (TFF). In these systems, the feed solution is pumped parallel to the membrane surface and thus perpendicular to the direction of the filtrate flow. This allows retained species to be swept along the membrane surface and out the device, which significantly increases the filtrate flux and reduces fouling [19, 24]. The most widely used cross flow systems include hollow fiber modules and TFF cassettes. TFF cassettes use a screened channel design that helps with mixing and flow distribution in the channel, leading to much higher mass transfer coefficients and consequently greater filtrate flux [25].

When applied for final formulation, ultrafiltration systems are used to separate undesired buffer components from the product and / or exchange the solution to achieve the desired buffer composition and to reach the final desired product concentration. In both cases the membrane is selected based on the molecular weight of the bioproduct as well as the permeability characteristics of the membrane as described by van Reis and Zydney [26] and Huisman et al. [27]. In diafiltration, the desired buffer is continuously added to the feed solution as filtrate is removed [28]. The number of volumetric equivalents (diavolumes) necessary to remove buffer components and ensure complete buffer exchange can be calculated from available models and confirmed by appropriate methods such as NMR [29]. In industry the incoming pool for formulation is first concentrated by ultrafiltration to an intermediate concentration (to minimize the required

buffer volume for the diafiltration), then buffer exchanged, and finally concentrated to achieve the required final concentration for formulation. The intermediate concentration and the number of diavolumes used for the diafiltration depend on both economics and the targeted small molecule removal [18].

Although previous studies have shown that ultrafiltration is much more attractive for final formulation than either size-exclusion chromatography [30] or lyophilization [18], there are significant challenges in applying these systems to very high concentration protein solutions. This includes limited product solubility, product losses during recovery, restrictive bulk mass transport of protein solutions at high concentrations, and high solution viscosity.

1.3 Thesis Program

Despite the increasing demand for very highly concentrated mAb formulations, there is currently no fundamental understanding of the ultrafiltration behavior of these highly concentrated solutions and what controls the maximum achievable protein concentration in these systems. It is well known that these concentrated protein solutions show thermodynamically non-ideal behavior where intermolecular interactions play a critical role [31, 32], although the specific impact of these interactions on mass transport during ultrafiltration remain to be determined. The overall objective of this thesis was to understand the factors controlling the filtrate flux and maximum achievable antibody concentration during ultrafiltration of highly concentrated mAbs (concentrations higher than 150 g/L) and to develop a theoretical framework that can predict the ultrafiltration

behavior at different conditions. This included: (1) obtaining quantitative data for ultrafiltration of a highly purified mAb solution at different conditions (2) evaluating intermolecular interactions in highly concentrated mAb solutions and its effect on filtrate flux, (3) determining and evaluating the key physical and operating properties controlling the maximum achievable concentration, (4) developing a model that describes the ultrafiltration behavior through the entire concentration range, and (5) providing a framework to guide further improvements in the filtrate flux and maximum achievable concentration.

Chapter 2 includes a brief review of the general theoretical background used to analyze the ultrafiltration data with a particular emphasis on bulk solute mass transport phenomena in membrane systems. This general framework was subsequently applied to examine the effects of key process variables on the system performance.

Chapter 3 includes the description of the apparatus, basic experimental systems, materials and methods used in the experimental studies performed in this thesis. Additional details on some of the experimental procedures are provided in the appropriate chapters.

Chapter 4 presents experimental data for the osmotic pressure of a monoclonal antibody solution for concentrations up to more than 200 g/L. Data were obtained over a range of solution conditions including different pH and salt concentrations and in the presence of different excipients. The extent of intermolecular interactions was estimated by evaluating the virial coefficients, with the results compared with model calculations and with independent results obtained by self-interaction chromatography.

Chapter 5 describes the methodology used to modify and improve self-interaction chromatography as a technique for the high-throughput evaluation of the second virial coefficients.

Chapter 6 presents experimental results for the viscosity behavior of monoclonal antibody solutions for concentrations up to more than 200 g/L. The viscosity data were fit to a semi-empirical model, with the results analyzed in terms of the intermolecular interactions to obtain additional insights into the rheological behavior.

Chapter 7 presents a modified polarization model that was used to describe the ultrafiltration behavior through the entire concentration range. This model accounts for the effects of intermolecular interactions on protein mass transfer as well as possible back-filtration in the TFF module. Back-filtration can occur near the exit of the module at high mAb concentrations due to the high viscosity and consequently large axial pressure drop over the length of the module.

Chapter 8 examines the effect of different buffer compositions and operating conditions on the filtrate flux during batch ultrafiltration of a monoclonal antibody up to concentrations higher than 200 g/L. Data were obtained in both flat sheet cassettes having different internal screens and in hollow fiber modules with different length. These results provide important insights into the key parameters that determine the filtrate flux and maximum concentration that can be achieved during ultrafiltration.

Chapter 9 summarizes the major contributions of this thesis and makes several recommendations for future studies on ultrafiltration processes for highly concentrated protein solutions.

Chapter 2

Theoretical Background

2.1 Introduction

This chapter reviews the theoretical models that have been developed to describe the basic mass transfer phenomena governing the behavior of ultrafiltration systems. Most of the discussion presented in this chapter is based on the reviews provided by Zeman and Zydney [33] and several dissertations published under the direction of Professor Andrew Zydney including the theses by Narahari Pujar [34], Senyo Opong [35], Skand Saksena [36], Jessica Molek [37], and Mahsa Rohani [38].

The overall performance of an ultrafiltration system is determined by the rate of solute transport from the bulk solution to the membrane surface and the rate of transport through the membrane pores (membrane transport). Some of the other factors that can be important in ultrafiltration include protein adsorption within the porous structure of the membrane and protein deposition which results in the formation of a protein deposit on the upper surface of the membrane [39]. However, the application of ultrafiltration systems for product formulation and concentration involves the use of membranes which

are fully retentive to the protein product; therefore, the rate of solute transport through the membrane pores is practically zero and protein adsorption within the pores is negligible.

This chapter discusses the theoretical background on transport phenomena that control the filtrate flux during ultrafiltration processes. Solvent transport through membranes is briefly discussed in section 2.2 and bulk mass transport phenomena are discussed in section 2.3. These discussions are intended to provide a general overview of the previous work; additional information on the theoretical approaches that have been specifically developed for ultrafiltration of highly concentrated solutions are presented in Chapter 7. The last part of this chapter includes a brief review of the theoretical analysis used to determine the net charge of the monoclonal antibody used in this work based on the known amino acid composition and electrophoretic mobility measurements. A more detailed discussion of protein net charge is available in Menon [40].

2.2 Membrane Transport

The transport characteristics of ultrafiltration membranes are typically described in terms of four macroscopic transport properties including the hydraulic permeability, the osmotic reflection coefficient, the solute diffusivity through pores, and the solute sieving coefficient. The hydraulic permeability is a measure of the resistance to solvent flow which depends primarily on the membrane porosity, pore radius, pore length, and tortuosity. The osmotic reflection coefficient determines the extent to which the solvent flow is reduced by osmotic pressure differences and is a complex function of the ratio of solute to pore size as well as the presence of any long range interactions between the

solute and pore. The solute diffusivity and sieving coefficient characterize the diffusive and convective solute flux through the membrane, respectively. However, for a fully retentive membrane, the rate of solute transport through the pore is negligible, corresponding to a sieving coefficient of zero and an osmotic reflection coefficient equal to one [41].

The Kedem-Katchalsky equations are commonly used to describe solvent transport through membranes as discussed elsewhere [42-44]. These equations are developed from the principles of irreversible thermodynamics, with the fluxes assumed to be linearly related to all of the driving forces [42]:

$$J_v = \frac{L_P}{\eta}\Delta P_{TM} + \frac{L_{PD}}{\eta}\Delta\Pi \tag{2.1}$$

where ΔP_{TM} and $\Delta\Pi$ are the transmembrane and osmotic pressure differences across the membrane, respectively, η is the solution viscosity, and J_v is the volumetric filtrate flux across the membrane (volumetric filtrate flow rate divided by the membrane area giving units of m/s). Equation (2.1) can be rewritten in terms of the osmotic reflection coefficient (σ_0) as:

$$J_v = \frac{L_P}{\eta}\left(\Delta P_{TM} - \sigma_0\Delta\Pi\right) \tag{2.2}$$

The osmotic reflection coefficient is thus related to the Kedem-Katchalsky coefficients as [45]:

$$\sigma_0 = -\frac{L_{PD}}{L_P} \tag{2.4}$$

L_p is the membrane hydraulic permeability which depends on the membrane properties. For a membrane with uniformly distributed cylindrical pores, the filtrate flux can be evaluated directly from the Hagen-Poiseuille equation as:

$$J_v = \frac{\varepsilon r_p^2}{8\eta\delta_m}\Delta P_{TM} \tag{2.5}$$

where r_p is the pore radius, ε is the porosity of the membrane (pore area per unit cross-sectional area of the membrane), and δ_m is the membrane thickness. Thus the membrane hydraulic permeability can be related to the properties of the membrane as:

$$L_P = \frac{\varepsilon r_p^2}{8\delta_m} \tag{2.6}$$

Equation (2.5) is valid when pore end effects are negligible, i.e. $\delta_m >> r_p$, which is true for all commercially available ultrafiltration membranes.

2.3 Bulk Mass Transport

During ultrafiltration, the applied pressure gradient across the membrane causes a convective flow from the bulk solution toward the membrane and through the pores. This pressure driven flow causes the accumulation of retained proteins on the upstream surface of the membrane. This phenomenon is generally referred to as concentration polarization, with the solute concentration having its maximum value immediately adjacent to the membrane (C_w), decreasing with increasing distance from the membrane surface (moving toward the bulk solution), and becoming approximately equal to the bulk solution concentration (C_b) at a distance equal to the concentration boundary layer thickness (δ).

The extent of concentration polarization is determined by the balance between solute convective flow towards the membrane and the rate of solute diffusion away from the membrane, which depends on the device operating conditions (e.g., stirring speed or shear rate) and module geometry. Figure 2.1 shows a schematic representation of the concentration polarization phenomenon and solute transport within the concentration polarization boundary layer.

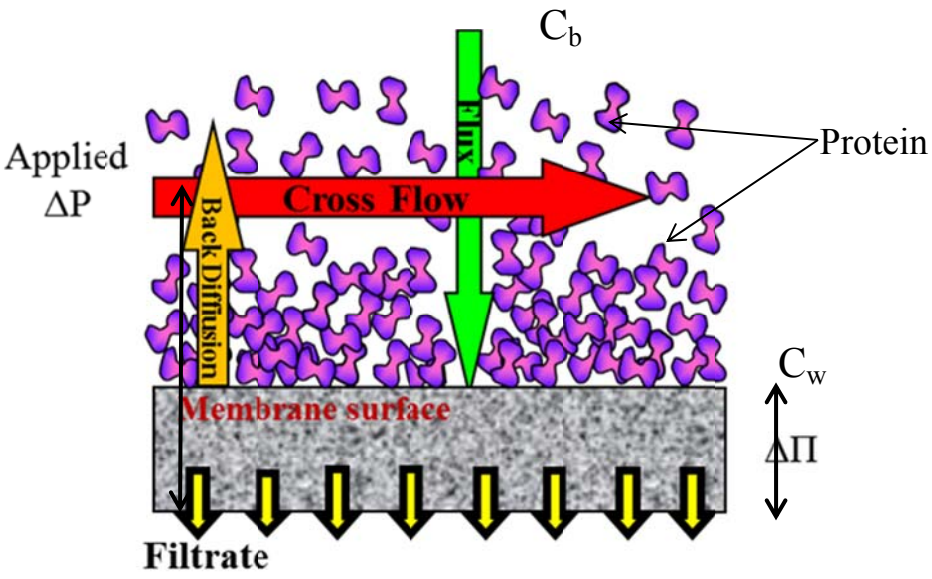

Figure 2.1 Schematic of concentration polarization phenomenon during protein ultrafiltration.

The accumulation of solute adjacent to the membrane and the consequent concentration gradient creates a driving force for back diffusion of solute molecules away from the membrane surface and into the bulk solution. In addition, the high osmotic pressure associated with this highly concentrated layer increases the osmotic pressure difference across the membrane thereby reducing the net rate of solvent transport

(Equation 2.2). At low transmembrane pressures, where concentration polarization effects are small, the filtrate flux is directly proportional to the effective pressure driving force. As the applied transmembrane pressure (ΔP_{TM}) is increased, the extent of concentration polarization will increase. This increase in protein concentration at the surface of the membrane reduces the filtrate flux by increasing the osmotic pressure at the feed side of the membrane [46]. In addition, the accumulated solute can, under some circumstances, form a dense cake or gel layer that provides an additional hydraulic resistance to the solvent flow [47]. At very high transmembrane pressures, the rate of solute transport back into the bulk solution can become limiting, with the filtrate flux approaching a value that becomes independent of the applied transmembrane pressure. The high protein concentration at the membrane surface can also increase the extent of membrane fouling leading to an increase in the membrane resistance (decrease in membrane permeability).

The solute concentration profiles in the bulk solution are described by the governing species continuity equation:

$$\frac{\partial C}{\partial t}+\frac{\partial}{\partial x}(UC)+\frac{\partial}{\partial y}(VC)=\frac{\partial}{\partial y}\left(D\frac{\partial C}{\partial y}\right) \tag{2.7}$$

where U and V are the fluid velocities in the y (normal to the membrane) and x (tangential) directions in a parallel plate membrane device, C is the local solute concentration, and D is the solute diffusion coefficient. Note that solute diffusion in the x-direction is assumed to be negligible compared to the rate of solute convection in that direction due to the high axial velocities. The 3-dimensional version of Equation (2.7) would be required to describe solute transport in a module with an internal screen (or spacer) due to the complex secondary flows generated by the screen. Equation (2.7) can

be solved by applying appropriate boundary conditions describing the continuity in filtrate and solute flux at the solution-membrane interface:

$$V = -J_v \qquad \text{at} \qquad y = 0 \text{ (membrane surface)} \qquad (2.8)$$

$$VC_w - \left(D\frac{\partial C}{\partial y} \right)_w = -N_s \qquad \text{at} \qquad \text{y = 0 (membrane surface)} \qquad (2.9)$$

where J_v and N_s are the filtrate flux and solute flux through the membrane. The negative signs in Equations (2.8) and (2.9) are due to the fact that V is in the negative y direction while J_v and N_s are traditionally taken as having positive values. N_s is equal to zero for a fully retentive membrane.

In order to actually solve Equation (2.7), one needs to know the detailed velocity profiles, which are coupled to the solute concentration profiles due to the dependence of the solution viscosity on the protein concentration. Solutions of the governing mass transfer equations are available for a number of simplified systems in which the solution viscosity and solute diffusivity are constant (independent of solute concentration) and the flow is fully developed. Detailed numerical solutions are also available which account for at least some of these additional phenomena, but these are typically impractical to use for the design and analysis of commercial-scale membrane systems.

2.3.1 Stagnant Film Model

In order to simplify the analysis of solute mass transfer in real membrane devices, the most common approach is to use a one-dimensional stagnant film model to develop an approximate solution to the governing equations. At steady state, the solute flux

through the membrane and into the filtrate solution is set equal to the net solute flux toward the membrane:

$$J_v C_f = J_v C + D\frac{\partial C}{\partial y} \tag{2.10}$$

where C is the local solute concentration at a positive position, y, above the membrane, D is the solute diffusivity, and C_f is the concentration of solute in the filtrate. Equation (2.10) can be integrated across the concentration polarization boundary layer (from $y = 0$ where $C = C_w$ to $y = \delta$ where $C = C_b$) giving the following expression for the filtrate flux:

$$J_v = \frac{D}{\delta}\ln\left(\frac{C_w - C_f}{C_b - C_f}\right) \tag{2.11}$$

Equation (2.11) is usually referred to as the simple concentration polarization (or stagnant film) model; it has been used extensively to describe solute and solvent transport in a variety of ultrafiltration systems. A more detailed discussion of this model, including the validity of the one-dimensional transport analysis, is provided by Zydney [48]. Equation (2.11) can be simplified for a fully retentive membrane ($C_f = 0$), with the filtrate flux being proportional to the logarithm of the bulk solute concentration.

The ratio of the solute diffusion coefficient to the boundary layer thickness (D/δ) is typically set equal to the solute mass transfer coefficient, k, which is a function of the solute diffusivity and the hydrodynamics of the device. The mass transfer coefficient can, at least in principle, be obtained by solving the appropriate mass transfer equations for the system geometry of interest or from appropriate empirical correlations. This is discussed in more detail in Section 2.3.4.

2.3.2 Osmotic Pressure Model

Despite the extensive use of the stagnant film model for the analysis of solute transport in membrane devices, there is still disagreement over the mechanism by which the accumulated solute limits the filtrate flux [46, 49]. One possible explanation for the limiting flux is the decrease in the effective driving force (ΔP_{TM} - $\Delta\Pi$) due to the significant increase in osmotic pressure at the high solute concentrations at the membrane surface, even for solutions of large macromolecules [31, 50]. In this case, any further increase in ΔP_{TM} is balanced by a corresponding increase in $\Delta\Pi$ in a way that the filtrate flux remains essentially constant (at the limiting flux) independent of the applied transmembrane pressure.

Although the filtrate flux in the osmotic pressure model can be evaluated from Equation (2.2), the osmotic pressure term, $\Delta\Pi$, is not known a priori and is typically much larger than that evaluated using the bulk solute concentration due to concentration polarization. The osmotic pressure is typically expressed in the form of a virial expansion as a function of the solute concentration [31]; this is discussed in more detail in Chapter 4. The filtrate flux in the osmotic pressure model is thus evaluated by simultaneously solving Equation (2.2) and Equation (2.11) for C_w and J_v (with $C_f = 0$ for a fully retentive membrane) and with $\Delta\Pi = \Pi_w$ (a function of C_w).

The osmotic pressure model has been used in multiple studies to explain the filtrate flux in ultrafiltration including results in stirred cells [51], in unstirred systems [31, 52], and in a rotary disk membrane filter [50]. Although this model gives good qualitative agreement with experimental data, both Robertson [53] and Vilker et al. [31]

found that a much larger value of the diffusion coefficient than that determined from direct diffusivity measurements was required to obtain quantitative agreement with experimental data. In contrast, Kozinski and Lightfoot [50] obtained good agreement with experimental data using an average value of the diffusion coefficient (based on the bulk and wall concentrations). Vilker et al. [51] found that the flux for BSA solutions was larger at pH values far away from the isoelectric point (e.g., at pH 7.4), which they attributed to the concentration and pH dependence of the BSA diffusivity, although this hypothesis was not verified experimentally. This is discussed in more detail in Chapter 8.

It is important to note that the filtrate flux predicted by the osmotic pressure model never actually attains a true pressure-independent value unless the solute concentration within the boundary layer undergoes a phase transition causing the effective osmotic pressure to increase without bound. This phenomenon is often referred to as gelation, with the filtrate flux now limited by the properties of the gel layer that forms on the membrane surface This is discussed in more detail by Zeman and Zydney [33] as summarized in the next section.

2.3.3 Gel Polarization Model

In the gel polarization model, the solute concentration at the membrane surface (C_w) is assumed to attain a constant (maximum) value at high ΔP_{TM} that is determined by the physical characteristics of the gel (C_g). This gel layer provides an additional hydrodynamic resistance to flow in series with that of the membrane. The filtrate flux is given by Equation (2.1) accounting for the total resistance in the system:

$$J_v = \frac{\Delta P_{TM} - \Delta\Pi}{R_m + R_g} \tag{2.12}$$

where R_m=1/L_P is the membrane resistance and R_g is the resistance of the gel layer. Most applications of the gel model assume that $\Delta\Pi \approx 0$, although this isn't required. Thus, within the pressure-independent regime, any increase in ΔP_{TM} is simply balanced by an increase in the gel layer resistance with the filtrate flux remaining constant.

The gel polarization model has been used by used by several investigators [54-56] to explain filtrate flux data in ultrafiltration, although the calculated values of the gel layer concentration are often inconsistent with independent measurements of the properties of the macromolecular solution. For example, the gelation concentration obtained for albumin by extrapolating a plot of the limiting filtrate flux versus ln(C_b) to zero filtrate flux ranges from as low as 17.4 wt % [57] to as high as 58 wt % [54] with most of the data falling between 30 to 40 wt % [55, 58]. While these values appear to depend on device geometry and shear rate, many of the C_g values reported in the literature are significantly smaller than the known gelation concentration for the given protein molecule [51, 59], suggesting that the gel layer may not exist as a distinct thermodynamic phase [39].

2.3.4 Mass Transfer Coefficient

As discussed previously, the ratio of the solute diffusion coefficient (D) to the boundary layer thickness (δ) is typically set equal to the solute mass transfer coefficient. The mass transfer coefficient in open cross flow devices (no screens), either parallel plate

cassettes or hollow fiber modules, is generally evaluated using the Leveque approximation developed from the corresponding heat transfer problem [60]:

$$k = 0.538\left(\frac{D^2\gamma_w}{x}\right)^{1/3} \tag{2.13}$$

where γ_w is the wall shear rate and x is the distance measured along the axial flow-path of the membrane device. The solute diffusion coefficient is typically evaluated using the Stokes-Einstein equation:

$$D = \frac{k_B T}{f} = \frac{k_B T}{6\pi r_s \eta} \tag{2.14}$$

where f is the frictional coefficient, k_B is the Boltzmann constant (1.39×10^{-23} J/K), T is the solution temperature, η is the solution viscosity, and r_s is the hydrodynamic radius of the solute. The solute diffusion coefficient and consequently the mass transfer coefficient depend on solute concentration, solution pH, and solution ionic strength due to the effects of intermolecular interactions.

There have been a number of efforts in the literature to address the concentration dependence of the mass transfer coefficient. For example, Aimar and Field [61] took into account the high viscosity in the solution near the membrane surface by proposing a correction factor of $(\mu_b/\mu_w)^{0.27}$ for the mass transfer coefficient. Similarly, Gekas and Hallstrom [62] suggested multiplying available mass transfer coefficients (developed based on constant physical properties and in turbulent flow) by a correction factor of the form $(Sc_b/Sc_w)^{0.11}$ where Sc_w and Sc_b are the Schmidt numbers at the wall and in the

bulk solution, respectively. The use of the Schmidt numbers accounts for the concentration dependence of the viscosity and the diffusion coefficient.

Zydney [63] used a different approach in which the concentration dependence of the diffusion coefficient was directly incorporated into the differential form of the mass balance, with the resulting ordinary differential equation integrated over the boundary layer thickness. Bowen and Williams [64] developed a model for the pressure dependence of the filtrate flux in a cross-flow system by focusing on the detailed dependence of both the osmotic pressure and diffusion coefficient on the local solute concentration. Their model was able to properly describe the filtrate flux behavior in a rectangular channel for different physicochemical conditions. Saksena and Zydney [65] developed a numerical solution of the governing continuity equations in a stirred cell system by accounting for both the thermodynamic and hydrodynamic consequences of protein-protein interactions. This detailed model provided an improved description of the concentration profiles for protein mixtures where intermolecular interaction effects were significant. More details regarding the concentration dependence of the mass transfer coefficient are provided in Chapters 7 and 8.

2.4 Protein Net Charge Analysis

2.4.1 Protein Charge Calculation from Amino Acid Composition

Protein molecules consist of a sequence of amino acids folded into a specific three dimensional structure. Most of the amino acid residues that are ionizable (charged) are located on the external surface of the protein. The protein surface charge density is

determined by the dissociation of these residues along with the binding of any ions from the bulk electrolyte. The dissociation equilibrium of a typical amino acid residue (for example, an α-carboxylic acid) is described by the intrinsic dissociation constant of that ionizable group:

$$K_{\text{int}}^{i} = \frac{\left[R-COO^{-}\right]\left[H^{+}\right]}{\left[R-COOH\right]} \tag{2.15}$$

Equation (2.15) can be rewritten in terms of the pH, the total number of amino acids of that type (n_i), and the number of dissociated groups (r_i):

$$pH = pK_{\text{int}}^{i} + \log\frac{r_i}{\left(n_i - r_i\right)} \tag{2.16}$$

where pH = -log[H^+] with [H^+] being the local concentration of H^+ at the protein surface and pK^i_{int} = -log[K^i_{int}]. Due to the electrostatic interactions between the charged amino acid residues on the surface of the protein and the charged hydrogen ions in solution, the local concentration of H^+ at the protein surface is different than the bulk H^+ concentration (H_b^+). This effect can be described using a classical Boltzmann distribution:

$$H^{+} = H_b^{+}\exp\left(\frac{-e\Psi_s}{k_B T}\right) \tag{2.17}$$

where e is the electron charge (1.602×10^{-19} C) and ψ_s is the electrostatic potential at the protein surface:

$$\Psi_s = \frac{eZ}{4\pi\varepsilon r_s\left(1+\kappa r_s\right)} \tag{2.18}$$

where Z is the net charge (evaluated as the number of electronic charges) on the protein surface, ε is the electrical permittivity of the solution (7.09×10^{-8} C/ m for water at 298 K), and κ is the inverse of the Debye length defined as:

$$\kappa^{-1} = \left(\frac{\varepsilon RT}{F^2 \sum z_i^2 C_i} \right)^{1/2} \tag{2.19}$$

where F is Faraday's constant (9.65×10^4 C/mol), R is the ideal gas constant (8.314 J/mol.K), z_i is the ion valence, and C_i is the ion concentration. The inverse Debye length for a 20 mM solution is 5.15×10^8 m^{-1}. Equation (2.18) is developed assuming that the protein is a hard sphere with the electrical charge distributed uniformly over the spherical surface [66]. The protein net charge (Z) is equal to the difference between the maximum number of positive charges (N-terminal amine, lysine, arginine, and histidine) and the sum of all the dissociated groups:

$$Z = Z_{maz}^{+} - \sum_{i=1}^{n} r_i \tag{2.20}$$

Equations (2.16) to (2.20) are solved iteratively to evaluate the net charge as a function of the bulk pH and solution ionic strength (which determines the Debye length). More details on the development of these equations is available in Menon and Zydney [67]. A list of pK_a values for the various amino acids is given in Appendix A.

Typical results for the net protein charge as a function of solution pH are shown in Figure 2.2 for the model monoclonal antibody used in this work at three different buffer salt concentrations (ionic strength). The blue curve shows the model calculations in the absence of any charge regulation effects, i.e. assuming that the local H^+ concentration (and thus the local solution pH at the protein surface) is equal to that in the

bulk solution. The protein isoelectric point (pI), the pH at which the net protein surface charge is zero, is predicted to be 8.4 ± 0.1, which is in good agreement with the reported value (8.2 ± 0.1) for this molecule. This small discrepancy could be due to ion binding interactions or to a shift in the pK_a of certain amino acids due to local charge-charge interactions [68, 69].

As shown in Figure 2.2 the protein charge increases with decreasing pH due to further protonation of the various ionizable groups on the protein surface. At pH < pI the protein net charge increases with increasing salt concentration, while the opposite behavior is predicted for pH > pI due to charge regulation effects. As mentioned previously, the electrostatic interactions between H^+ ions in the bulk solution and the protein surface cause the local pH at the protein surface to be different from the bulk pH. These electrostatic interactions are shielded at higher salt concentrations. Therefore, at pH < pI, where the protein has a net positive charge, the H^+ ions are repulsed from the protein surface ($H_b^+ > H^+$), with this effect being reduced at higher salt concentrations. On the other hand, at pH > pI the protein is negative and attracts H^+ to the protein surface thus lowering the local pH.

Figure 2.2 also compares the calculated values of the net protein charge with the experimentally determined values using electrophoretic mobility measurements as explained in the next section and discussed briefly in Chapter 4.

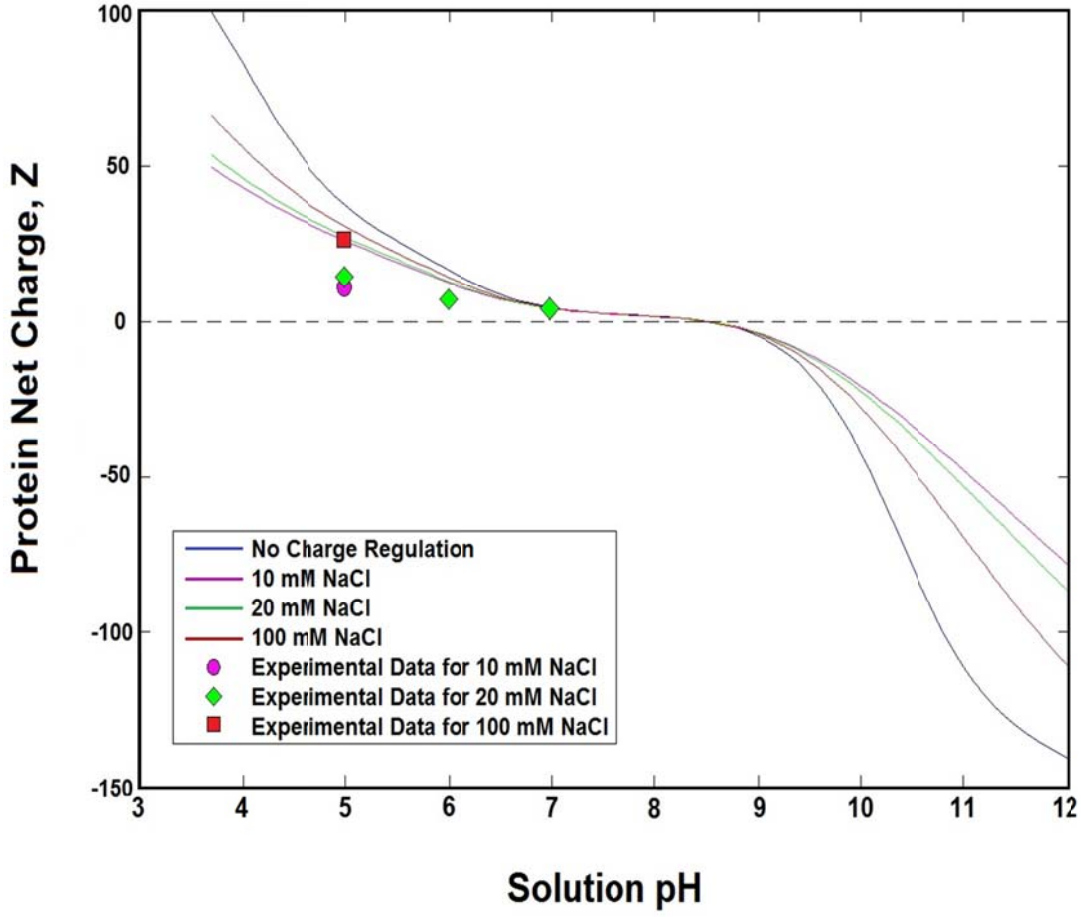

Figure 2.2 Calculated net charge of the monoclonal antibody as a function of solution pH at different ionic strengths compared with experimental results from electrophoretic mobility measurements. The blue curve represents calculated values of the net protein charge assuming the H^+ concentration at the protein surface equals that in the bulk.

2.4.2 Protein Charge from Electrophoretic Mobility Measurements

In the presence of an applied electric field, suspended charged particles in an electrolyte solution are attracted toward the opposite electrode while the hydrodynamic (viscous) forces associated with the movement of the particle tend to oppose this motion.

When these two opposing forces are equal, the particle moves with a constant velocity described by the electrophoretic mobility (equal to the ratio of the velocity to the applied electric field). The calculation of the net protein charge from the measured electrophoretic mobility requires a model for electrophoretic motion. A large number of theoretical analyses have been presented in the literature for the electrophoretic mobility, with the differences lying primarily in the approximations made in evaluating the electrical interactions. These differences include both the detailed structure of the equilibrium electrical potential (e.g., the use of low electrical potential, small Debye length, or flat plate approximations) and the distortion of the equilibrium structure associated with the particle and fluid motion during electrophoresis. The simplest approach is to treat the protein as a non-conducting charged sphere with a uniform surface charge density. A relationship between the electrophoretic mobility and the potential at the surface of the sphere is obtained by solving the governing equations for the electrical drag forces acting on the particle [66]. In the simplest limiting case, when the electrical double layer thickness is much smaller than the protein radius (i.e. $\kappa r_s \geq 1$), the electrophoretic mobility (μ_E) is given by the Helmholtz-Smoluchowski equation:

$$\mu_E = \frac{\varepsilon \zeta}{\eta} \tag{2.21}$$

where ζ is the electrostatic potential at the protein surface, ε is the electrical permittivity of the solution, and η is the solution viscosity [70].

If the electrical double layer is much larger than the particle radius (i.e. $\kappa r_s \leq 1$), the electrophoretic mobility is given by the Debye-Huckel equation assuming that the potential is low:

$$\mu_E = \frac{2}{3}\frac{\varepsilon\zeta}{\eta} \tag{2.22}$$

Henry [71] obtained a more complete solution for the electrophoretic mobility that accounts for the distortion of the electric field lines by the presence of the particle, with the resulting expression valid over the entire range of Debye length:

$$\mu_E = \frac{2}{3}\frac{\varepsilon\zeta}{\eta} f_H(\kappa r_s) \tag{2.23}$$

where f_H is Henry's function which accounts for the finite double layer thickness:

$$\begin{aligned} f_H(\kappa r_s) = 1 &+ \frac{1}{16}(\kappa r_s)^2 - \frac{5}{48}(\kappa r_s)^3 - \frac{1}{96}(\kappa r_s)^4 + \frac{1}{96}(\kappa r_s)^5 \\ &+ \left[\frac{1}{8}(\kappa r_s)^4 - \frac{1}{96}(\kappa r_s)^6\right]\exp(\kappa r_s)\int_{\infty}^{\kappa r_s}\frac{\exp(-t)}{t}dt \end{aligned} \tag{2.24}$$

where t is a dummy variable over which the integration is performed.

The electrostatic potential at the surface can be used to evaluate the net protein charge using Equation (2.18) giving:

$$Z = \frac{6\pi\eta(1+\kappa r_s)r_s}{ef_H}\mu_E \tag{2.25}$$

A more detailed discussion on the evaluation of the electrophoretic mobility is provided by Menon [40] and Molek [37].

Chapter 3

Materials and Methods

3.1 Introduction

This chapter describes the general materials and methods used for the experimental studies included in this thesis. Additional details on specific materials, apparatus, and procedures are provided in the subsequent chapters as appropriate.

3.2 Experimental Materials

3.2.1 Buffer Solutions

Appropriate buffers were used to control the pH of the protein solutions. All buffers were prepared using the methods described by Beynon and Easterby [72] with the solution ionic strength evaluated as:

$$I = \frac{1}{2}\sum_i z_i^2 C_i \qquad (3.1)$$

where z_i and C_i are the valence and total concentration of each ion, respectively. Buffer solutions were prepared by dissolving pre-weighed amounts of the appropriate salts in

deionized distilled water obtained from a NANOpure® Diamond water purification system (Barnstead Thermolyne Corporation, Dubuque, IA) with resistivity greater than 18 MΩ-cm. All salts were analytical reagent grade. The solution pH was measured using a Model 402 Thermo Orion pH meter (Beverly, MA) and was adjusted using 1 M hydrochloric acid or sodium hydroxide as required. The solution conductivity was evaluated using a Model 105A plus Thermo Orion conductivity meter (Beverly, MA) referenced to 25°C. All solutions were pre-filtered through 0.2 μm pore size Supor® 200 membranes (Pall Corp., Ann Arbor, MI) with 47 mm diameter using a vacuum pump to remove any particulates and un-dissolved salts prior to use. The concentrations of buffer components used in the most common buffers are shown in Table 3.1.

Table 3.1 Components for different buffers used in experiments.

Buffer	Ionic Strength	pH	Acid	Acid (mol/L)	Base	Base (mol/L)	Salt	Salt (g/L)
Acetate	10 mM	5	CH_3COOH	0.0017	$NaCH_3COO$	0.0032	NaCl	0.392
Acetate	20 mM	5	CH_3COOH	0.0016	$NaCH_3COO$	0.0033	NaCl	0.975
Acetate	100 mM	5	CH_3COOH	0.0015	$NaCH_3COO$	0.0034	NaCl	5.652
Phosphate	20 mM	6	NaH_2PO_4	0.0044	$Na_2HPO_4•7H_2O$	0.005	NaCl	0.810
Phosphate	20 mM	7	NaH_2PO_4	0.0025	$Na_2HPO_4•7H_2O$	0.0024	NaCl	0.590

3.2.2 Protein Solutions

A highly purified monoclonal antibody was received from Amgen (frozen) with a concentration of approximately 20 g/L. The monoclonal antibody was obtained just prior

to final formulation (e.g., after Protein A chromatography and at least one ion exchange step) and has a molecular weight of 141,959 Da and an isoelectric point (pI) of 8.16. The exact structure and sequence of the monoclonal antibody is unknown. The antibody was kept frozen at -80 °C and thawed by first equilibrating for 1 day at -20 °C and then 2 days at 4 °C. The antibody was placed in the desired buffer solution by diafiltration through fully retentive Ultracel™ composite regenerated cellulose membranes with either 10 or 30 kDa nominal molecular weight cut-off (Millipore Corp., Bedford, MA) as explained in Section 3.3.4. After the diafiltration, the monoclonal antibody was concentrated to approximately 20 g/L. The final solution ionic strength was achieved by dilution with appropriate buffer. This approach minimized errors associated with buffer partitioning during the ultrafiltration / diafiltration [33]. The solution pH was then evaluated using a Model 402 Thermo Orion pH meter (Beverly, MA) and adjusted as needed by adding small amounts of 0.5 M solutions of the appropriate acid or base (e.g., HCl or NaOH). The solution was then filtered through a 0.2 μm pore size Supor® 200 membrane (Pall Corp., Ann Arbor, MI) to remove any un-dissolved salt, particulate matter, or insoluble protein aggregates that might have formed or been introduced during the preparation steps. The resulting solution was frozen and stored in 100 mL aliquots at -80 °C for long term use. These aliquots were thawed using the approach described previously along with a final incubation at room temperature (for 1 hr). Protein solutions were kept at 4 ^{o}C between experiments (maximum storage time of one week).

3.2.3 Excipients

Excipients are natural or synthetic substances that are included in drug product formulations to assist with product stability, prevent denaturation and aggregation over the expected shelf life, and / or enhance the therapeutic effect, drug absorption, or solubility. Various types of excipients are used in bioprocessing, including sugars, amino acids, and surfactants. Excipients are usually added to the product during the formulation step via diafiltration and therefore their presence within this step can have a significant influence on the ultrafiltration/diafiltration behavior. The excipients examined in this thesis were sucrose (Sigma, S-2395), L-proline (SPECTRUM, P1434), and arginine-HCl (JT Baker, 2067-06), all USP grade. Figure 3.1 shows the structure of these molecules as provided by the manufacturers.

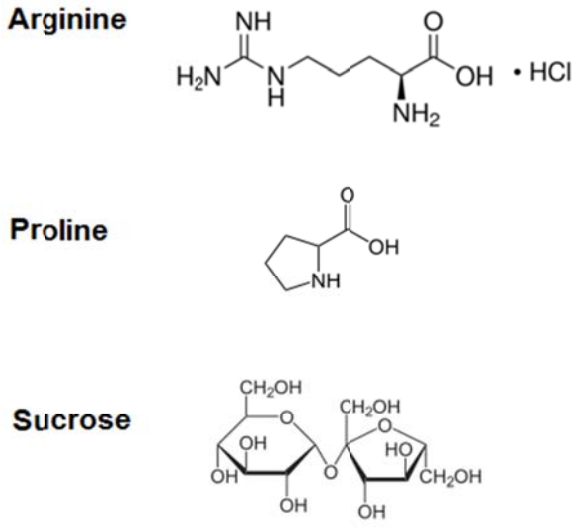

Figure 3.1. Chemical structure of arginine-HCl, L-proline, and sucrose. Adapted from manufacturers' websites.

3.2.4 Dextran Solutions

Dextrans are neutral polymers of glucose, joined by α-1,6 linkages; possible branches can attach to the main chain via α-1,3 linkages as shown in Figure 3.2. Dextrans are synthesized naturally by a strain of lactic acid bacteria (*Leuconostoc mesenteroides*). Dextran standards of specific molecular weight are typically produced by partial hydrolysis of the natural product.

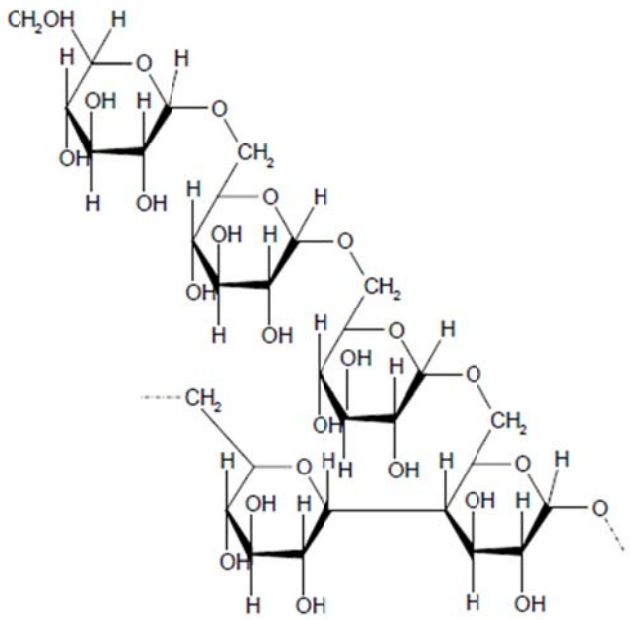

Figure 3.2 Chemical structure of dextran. Adapted from Burns [73].

Dextran standards have been used extensively in the past for size-based characterization of chromatography columns and membranes since they do not have any ionizable side groups; thus, their interactions are typically based entirely on their relative

size. The Stokes radius (r_s) for the dextran standards can be evaluated using the Stokes-Einstein equation as correlation [74]:

$$r_s = 0.0488 MW^{0.437} \tag{3.2}$$

Narrow molecular weight dextran standards were used for calibration in size exclusion chromatography and to find the dextran with equivalent hydrodynamic volume as the monoclonal antibody; this was used to measure the dead column volume in self-interaction chromatography experiments as described in Chapter 5. Blue dextran with 1000 kDa molecular weight (Catalog number D5751 from Sigma, St. Louis, MO) was used as a fully excluded solute in self-interaction chromatography experiments. Dextran solutions were prepared by dissolving pre-weighed amounts of powdered dextran (from Sigma Chemical, St. Louis, MO and American Polymer Standards, Mentor, OH) in the desired buffer solution. All the dextran solutions were pre-filtered through a 0.22 μm Acrodisc® syringe filter (PALL Corp., Ann Arbor, MI) immediately prior to use.

3.2.5 Ultrafiltration Membranes

All filtration experiments, diafiltrations, and osmotic pressure measurements performed in this thesis were done using Ultracel™ composite regenerated cellulose membranes with nominal molecular weight cut-offs (MWCO) of 30 kDa (and in some cases 10 kDa for early diafiltrations) in the form of either flat sheets or TFF cassettes, both provided by Millipore Corp. (Bedford, MA). The nominal molecular weight cut-off refers to the molecular weight of a solute which has approximately 90% rejection as determined by the manufacturer. The effective pore size for the Ultracel™ membranes

was estimated from the hydraulic permeability (L_p) using Equation (2.6) using a membrane porosity of $\varepsilon = 0.5$ [75] and a membrane thickness of $\delta_m = 0.8$ µm, which gives pore radii of 2.4 nm for the 10 kDa membrane and 3.2 nm for the 30 kDa membrane. The Ultracel membranes have an asymmetric structure. The thin skin and upper porous region are made of cellulose which is cast on a thicker more porous support of polyethylene. Figure 3.3 shows a scanning electron microscopy image (SEM) of the cross section of the composite regenerated cellulose membrane (adapted from manufacturer's website).

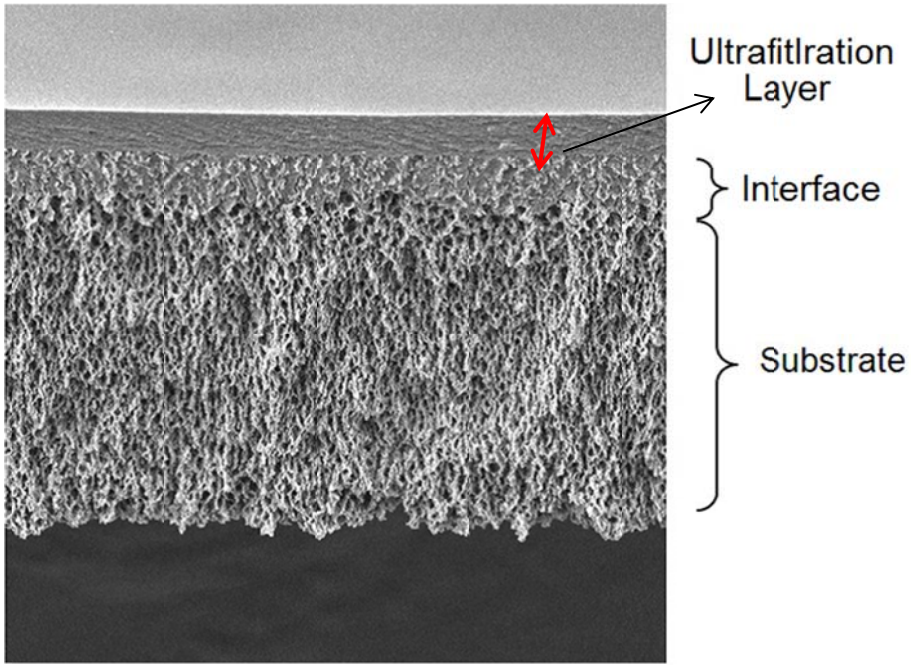

Figure 3.3. SEM image of an Ultracel™ membrane cross-section (adapted from Ruanjaikaen, 2013)

The regenerated cellulose skin is approximately 0.5 - 1.0 µm thick (not visible in the SEM). The cellulose layer has a large number of surface hydroxyl groups which

makes it very hydrophilic leading to low levels of protein adsorption and fouling during ultrafiltration.

Flat sheet membranes were used for the osmotic pressure measurements (as explained briefly in Section 3.3.5 and in more detail in Chapter 4) and in initial diafiltration processes (Section 3.3.4). Membrane disks of desired diameter (based on the size of the stirred cell or osmometer) were cut from the flat sheets using a stainless-steel cutting device fabricated in our laboratory. All membranes were soaked in isopropanol for 45 min to remove any wetting/storage agents prior to use. The membranes were then thoroughly rinsed with at least 100 L/m^2 of deionized (DI) water. The membranes were stored in appropriate buffer or in 0.1 NaOH at 4 ^oC to prevent collapse of the membrane pore structure by drying and to minimize bacterial growth.

Pellicon^{TM} 3 tangential flow filtration modules (Millipore Corp. Bedford, MA) having 88 cm^2 membrane area were used for ultrafiltration experiments (including both batch ultrafiltration and total recycle experiments). These modules are around 20 cm in effective length with the channel width estimated to be around 2.2 cm. The channel height was estimated as $h = 0.024$ cm based on manufacturer's data for the feed channel hold-up volume (1.5 mL) assuming that the spacer occupies 30% of the channel. Modules were used with both C (Millipore, P3C030C00) and D screens (Millipore, P3C030D00). These screens enhance mass transfer by breaking up the growth of the concentration polarization boundary layer. The D screen cassettes are more open in structure; they are specifically designed for more viscous solutions. Figure 3.4 shows a schematic of a Pellicon 3 cassette. Cassettes were installed in a cassette holder and prepared using the procedures provided by Millipore; the experimental set-up is described in Section 3.3.2.

All modules were initially flushed with at least 500 mL of DI water to remove the shipping/storage solution and thoroughly wet the membrane pore structure. The modules were then flushed with 300 mL of the specific buffer to be used in the protein ultrafiltration experiment. After completion of the experiment, the module was first flushed with buffer to wash out any protein solution left in the system and then flushed with 500 mL of DI water and finally cleaned by recirculating a solution of 0.3 N NaOH at pH 10.5 for 30 min. The module was then filled with 0.1 N NaOH and stored in containers filled with the same solution at 4 ^{o}C between experiments. Modules were discarded after 1 month or if the permeability drops below 70% of the initial permeability and could not be restored after cleaning.

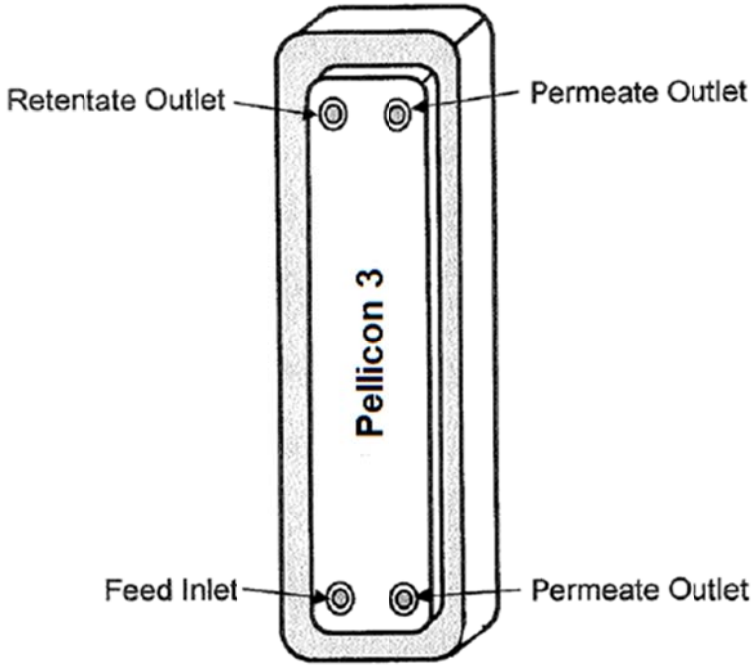

Figure 3.4 Schematic of the Pellicon 3 tangential flow filtration module.

A limited number of ultrafiltration experiments were performed using MicroKros® hollow fiber modules with 30 kDa modified polyethersulfone (mPES) membranes having 0.5 mm inner diameter with lengths of 20, 40, and 65 cm corresponding to membrane areas of 19, 38, and 61 cm^2 (Spectrum Labs, C02-E030-05-N). Figure 3.5 shows a schematic of a MicroKros® module. All hollow fiber modules were initially flushed with DI water at 5 psi, collecting at least 200 mL of filtrate, to remove the shipping/storage solution. The module was then rinsed with a solution of 50% isopropanol at 3-4 psi for an hour to thoroughly wet the membrane pore structure followed by at least 500 mL of DI water at 5 psi to thoroughly remove the alcohol. The membrane hydraulic permeability was then measured using DI water; modules were only used if the permeability was in the range suggested by the manufacturer (> 20 $L/m^2/hr/psi$). The module was then flushed with 100 mL of the specific buffer to be used in the protein ultrafiltration experiment. After each experiment, the module was first flushed with buffer to wash out any protein solution left in the system and then flushed with 300-400 mL of DI water followed by cleaning with 0.5 N NaOH for 1 hour. Modules were stored in DI water at 4°C as suggested by the manufacturer.

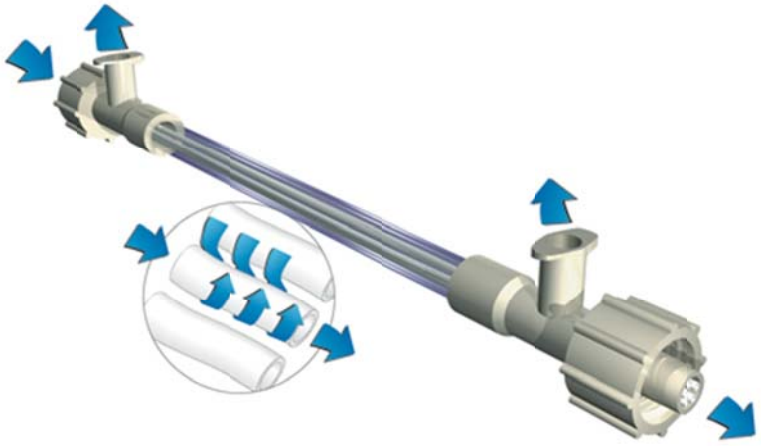

Figure 3.5 Schematic of the MicroKros hollow fiber module. Adapted from manufacturer (http://www.spectrumlabs.com/filtration/mPES.html#MicroKros).

3.3 Experimental Methods

3.3.1 Stirred Cell Set-up

Osmotic pressure measurements at high protein concentrations (>100 g/L) were performed using an Amicon 8200 stirred cell with effective membrane area of 28.7 cm^2 and 200 mL volume (Millipore Corp., Bedford, MA). The experimental set-up is shown in Figure 3.6. A membrane disk of 6.35 cm diameter was cut and placed in the bottom of the stirred cell directly on top of a porous layer of Tyvek® (of the same size) which was used as a support to minimize deformation of the membrane at high pressures. The membrane was held in place by a rubber o-ring that provided a leak-free seal.

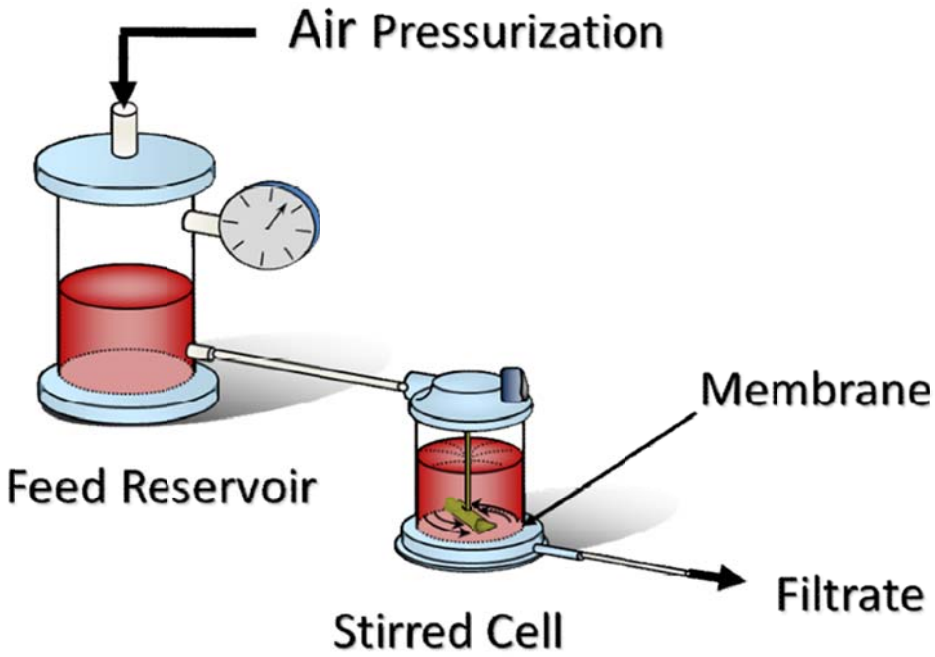

Figure 3.6. Schematic of experimental set-up used for osmotic pressure experiments. Adapted from Bakhshayeshirad [76].

The entire apparatus was then filled with the appropriate monoclonal antibody solution and connected to an air-pressurized acrylic solution reservoir to apply the desired transmembrane pressure via a pressure regulator (Scott Specialty gases, Plumsteadville, PA). The applied pressure was measured using a digital pressure gauge (Ashcroft, Model 0518, 0-30 psi) connected to the reservoir; the pressure on the filtrate side was atmospheric. The outlet of the stirred cell was connected to a narrow tube (1 mm diameter) to measure the very small filtrate flux at pressures close to the osmotic pressure (as explained in more detail in Chapter 4).

3.3.2 Osmotic Pressure Measurements

A number of different methods are available for measuring the osmotic pressure of a given solution including vapor pressure lowering, freezing point depression, and boiling point elevation, all of which depend on the number (molal) concentration of dissolved solutes in solution. However, the measured freezing point depression for a protein solution will be determined primarily by the large number of salt ions and buffer components in the solution, making it nearly impossible to determine the contribution of the protein. The same is true for the other colligative properties (e.g., vapor pressure lowering and boiling point elevation). Since the goal of these studies was to determine the effects of the monoclonal antibody on the thermodynamic behavior of the concentrated protein solution, it was necessary to use an approach that eliminated most (if not all) of the contributions from the salt and buffer components.

The osmotic pressure of the monoclonal antibody solution was thus measured using membrane osmometery with an Ultracel^{TM} 30 kDa membrane that is fully retentive to the monoclonal antibody but completely non-retentive to the salts and excipients. Based on the Kedem-Katchalsky equation (Equation 2.2), the filtrate flux through a membrane with a protein solution on one side and a buffer solution on the other side is zero if the applied transmembrane pressure is the same as the osmotic pressure difference across the membrane. Therefore for each buffer condition and protein concentration the osmotic pressure can be found by monitoring the filtrate flux across a membrane as a function of the transmembrane pressure to find the value of the transmembrane pressure corresponding to zero filtrate flux.

The apparatuses used for this purpose were either a stirred cell (as shown in Figure 3.6) or a membrane osmometer (as shown in Figure 4.1) where the positive and negative values for filtrate flux were evaluated by measuring the movement of the fluid in the outlet capillary. Additional experimental details are provided in Chapter 4.

3.3.3 Tangential Flow Filtration Set-up

Figure 3.7 shows the experimental set up used for all ultrafiltration experiments performed in this thesis. A positive displacement pump (Masterflex, Gelsenkirchen, Germany) was used to pump the monoclonal antibody solution from the feed reservoir into the membrane cassette.

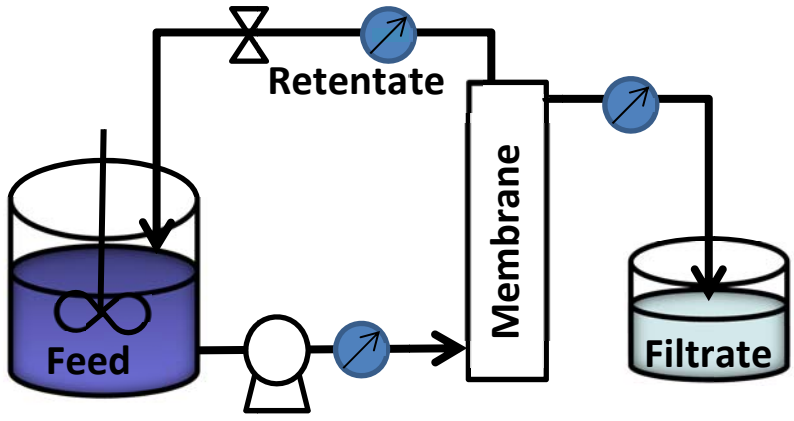

Figure 3.7. Schematic diagram of the tangential flow filtration set-up for batch ultrafiltration

The pump was initially calibrated using the specific tubing employed in the pump. High pressure tubing (L/S 15, Masterflex, Gelsenkirchen, Germany) was used for the

feed and retentate lines due to the high system pressures obtained during ultrafiltration with high monoclonal antibody concentrations. The pressures on the feed and retentate side were measured using analog high-pressure liquid pressure gauges (Ashcroft, 0-60 psi) while the pressure on the filtrate side was atmospheric. The Pellicon 3 module was assembled in the module holder and oriented vertically. The hollow fiber modules were also used vertically. The lower filtrate outlet was kept closed with the filtrate collected from the top filtrate port. All connections were sealed to avoid any leakage during the experiments. The feed solution was mixed using a magnetic stirrer bar. More details on the ultrafiltration experiments are provided in Chapter 8.

3.3.4 Membrane Hydraulic Permeability

The membrane hydraulic permeability (L_P) was evaluated by measuring the filtrate flux as a function of transmembrane pressure for at least four pressures (in the range of 1-10 psi) using DI water. The filtrate flux was determined by timed collection of the filtrate using a Model AG104 digital balance (Mettler Toledo, Columbus, OH) with accuracy of 0.1 mg. The permeability was evaluated from the slope of the filtrate flux (J_v) versus transmembrane pressure (ΔP_{TM}) data as:

$$L_p = \frac{\eta_{water} J_v}{\Delta P_{TM}} \tag{3.4}$$

where η_{water} is the viscosity of the water at the temperature of the experiment. The hydraulic permeability measurements were typically performed before and after each

experiment; the decrease in permeability provided a measure of the extent of undesired fouling during the experiments.

3.3.5 Diafiltration

Since the monoclonal antibody was received in a poorly defined buffer solution, diafiltration was performed to place the protein in the desired buffer. The ultrafiltration set-up shown in Figure 3.7 was used for the diafiltration with the volume of the solution in the feed tank kept constant by continuous addition of the desired buffer to the feed tank. The protein solution was pumped into the module from the feed tank using a peristaltic pump at a constant flow rate. The filtrate was collected in a separate tank. Samples were taken from the feed tank throughout the diafiltration for subsequent evaluation of the concentration of antibody dimers and higher order oligomers.

3.4 Assays

3.4.1 UV Spectrophotometery

The antibody concentration was measured using either a SPECTRAmax Plus 384 UV-Vis spectrophotometer (MD Corp., Sunnyvale, CA) or a NanoDrop 2000c spectrophotometer (Thermo Scientific, Waltham, MA) with the absorbance measured at a wavelength of 280 nm (corresponding to the natural absorbance of the aromatic groups in the tryptophan residues). The absorbance per cm for a 1 g/L solution of the monoclonal antibody in water was taken as 1.5882 (provided by Amgen). This absorbance coefficient

was used to evaluate the protein concentration directly from the absorbance in the NanoDrop; a calibration curve was used for the plate reader in the SPECTRAmax Plus. The calibration curve was constructed from a series of standard solutions of known concentration (determined by UV absorbance in the NanoDrop). More details on the protein concentration measurements are provided in the appropriate chapters.

3.4.2 Size Exclusion Chromatography

Size exclusion chromatography was used to determine the radius of the monoclonal antibody and to evaluate the concentration of antibody dimers and higher order oligomers. An Agilent 1100 Series high performance liquid chromatography (HPLC) system (Agilent Technologies, Palo Alto, CA) was used with a Superdex 200, 10/300 GL analytical column (13 μm particle size, fractionation of globular proteins with MW in the range of $1\times10^4 – 6\times10^5$ Da, fractionation of dextrans with MW in the range of $1\times10^3 – 1\times10^5$ Da, and 1.3×10^6 Da MW exclusion limit for globular proteins) obtained from GE Healthcare (Uppsala, Sweden). The chromatography system was operating using ChemStation software version A.04.08 (Agilent Technologies). The mobile phase was a 50 mM phosphate buffer at pH 7 containing 0.15 M NaCl with a flow rate of 0.3 mL/min. The running buffer was passed through a degasser to eliminate air bubbles and the column was flushed with a minimum of 2 column volumes. This also served to flush the sample and reference cells in the detectors. Column equilibration was verified by monitoring the baseline for the system detectors. 75 μl of the sample (with concentration of approximately 1 g/L) was injected over a period of 30 s. Sample detection was

performed using an Agilent 1100 series refractive index detector (RID) for dextrans and an Agilent 1200 series UV-Vis detector (VWD) at 280 nm for the monoclonal antibody, with the two detectors operated in series. The concentration of dimers and higher order oligomers was evaluated from the area of the corresponding peak determined by integration using the ChemStation software.

3.4.3 Self-interaction Chromatography

The second virial coefficient of the monoclonal antibody was evaluated by self-interaction chromatography (SIC). SIC was initially introduced by Patro and Przybycien [77] and the protocols were later developed by Tessier [78]. In this technique, protein molecules of interest are immobilized on chromatography beads with formyl groups on their surface through a chemical reaction with the protein's amine groups. The beads are then packed into a 1 mL chromatography column and a sample of the same protein is then run through the column. The difference between the protein retention volume and the retention volume of an equivalent non-interacting molecule (in our case a dextran standard with the same hydrodynamic volume) under the same condition gives a measurement of the two body interactions in the system (i.e. the second virial coefficient, B_2). As shown in Figure 3.8 the interactions between the antibody molecules in the bulk solution and those attached to the beads in the packed column.

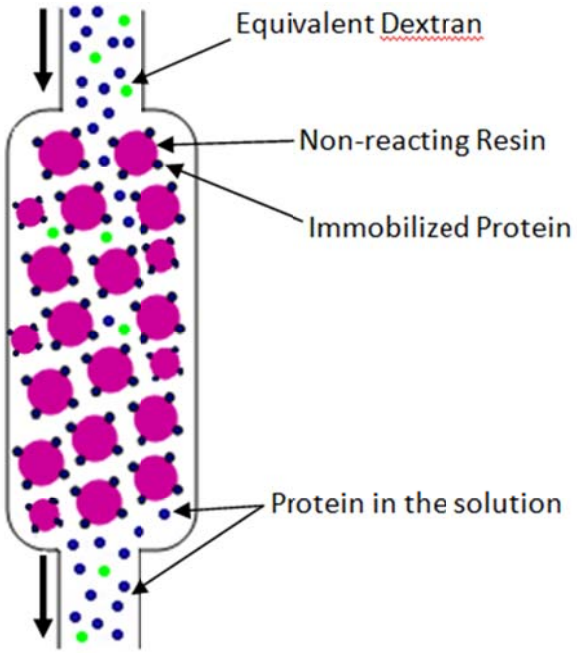

Figure 3.8. Schematic of self-interaction chromatography technique

SIC experiments were performed using an Agilent 1100 Series high performance liquid chromatography (HPLC) system (Agilent Technologies, Palo Alto, CA) that is fully automated making this method a valuable high throughput tool for evaluating B_2 values over a wide range of conditions. Additional experimental details are described in Chapter 5 while more details regarding the initial technique development and theoretical background can be found in the work by Tessier [78].

Chapter 4

Osmotic Pressure of Highly Concentrated Monoclonal Antibody Solutions

Note: Most of material presented in this chapter was previously published in: E. Binabaji, S. Rao, A.L. Zydney, The osmotic pressure of highly concentrated monoclonal antibody solutions: Effect of solution conditions, Biotechnology and Bioengineering, 111 (2014) 529-536.

4.1 Introduction

Therapeutic antibodies are currently used to treat a variety of diseases including cancer and many autoimmune disorders [79]. Antibodies are typically administered subcutaneously from devices at very high concentrations to achieve the desired therapeutic affect given the limited volumes that can be provided via subcutaneous delivery [15]. The behavior of these highly concentrated protein solutions can have a significant impact on the purification [51, 63, 65, 80, 81], formulation [18], and stability [82] of monoclonal antibody products.

A variety of methods have been used to evaluate intermolecular interactions in protein solutions including static light scattering [83], small-angle x-ray scattering [84, 85], sedimentation equilibrium [86-88], self-interaction chromatography [89], rheological

measurements [90], and fluorescence anisotropy and circular dichroism [91]. Osmotic pressure measurements are particularly useful in studying the behavior of highly concentrated protein solutions since the data can also provide a measure of higher order (multi-body) interactions [31, 92-94]. In addition, the osmotic pressure has a direct effect on the filtrate flux during protein ultrafiltration due to the reduction in the effective pressure driving force across the membrane, particularly at high degrees of concentration polarization [51, 95].

There have, however, been relatively few studies of the osmotic pressure for highly concentrated protein solutions (C > 50 g/L). Vilker et al. [31] evaluated the osmotic pressure of bovine serum albumin at concentrations up to 475 g/L, and this remains one of the classical studies in this field. Prausnitz's group evaluated the osmotic pressure of lysozyme [94, 96] and α-chymotrypsin [97], but the data were limited to concentrations well below 100 g/L. Yousef et al. [98] evaluated the osmotic pressure of serum IgG at very high protein concentrations. However, serum IgG is a heterogeneous mixture of immunoglobulins with isoelectric points ranging from 5.8 – 8.5, making it impossible to extrapolate these results to the behavior of a well-defined monoclonal antibody. In addition, the data were obtained at only a single pH (7.4) and at relatively high ionic strength (0.13 M NaCl), neither of which is typical of current antibody formulations. Perkins et al. [95] presented data for the osmotic pressure of a purified antibody up to concentrations of 200 g/L, but the data were limited to a single buffer condition (5 mM acetate at pH 5 with 150 mM NaCl), and no attempt was made to use the data to evaluate the intermolecular interactions. More recently, Salinas et al. [99] evaluated the osmotic pressure and second virial coefficient of a monoclonal antibody at

pH 6 over a range of conditions, but the data were limited to antibody concentrations below 100 g/L.

The objective of the work described in this chapter was to obtain quantitative data for the osmotic pressure of a highly purified monoclonal antibody at concentrations as high as 250 g/L and over a range of buffer conditions. The net protein charge in the different buffer solutions was evaluated from electrophoretic light scattering data, with the results used to evaluate the Donnan contribution to the osmotic pressure. The oncotic pressure data (after subtracting the Donnan contribution) were analyzed using a virial expansion, with the calculated values of the second virial coefficient compared with independent measurements obtained using self-interaction chromatography (data discussed in more detail in Chapter 5). These results were used to obtain insights into the nature of the intermolecular interactions in these concentrated solutions, while also providing the type of osmotic pressure data that are needed for the analysis of the filtrate flux in antibody ultrafiltration processes.

4.2 Materials and Methods

4.2.1 Osmotic Pressure Measurements

The protein osmotic pressure was evaluated using both a membrane osmometer (shown schematically in Figure 4.1) and a stirred ultrafiltration cell. The osmometer consists of two Plexiglas chambers, each with a volume of approximately 12 mL and a cross-sectional area of 3.1 cm^2. An Ultracel^{TM} composite regenerated cellulose membrane with 30 kDa nominal molecular weight cut off (Millipore) was cut from a large flat sheet

and sealed in a Plexiglas holder on top of a porous Tyvek support using o-rings. The membrane holder was placed between the two chambers and the entire assembly was screwed together. One chamber was filled with the antibody solution through the relatively large inlet port; this port was closed immediately after filling. The other chamber was filled with protein-free buffer solution and any entrapped air was removed. All experiments were performed at room temperature (23 ± 2 ºC).

The chamber containing the protein solution was attached to an air-pressurized reservoir, with the volumetric filtrate flux (J_v) evaluated at a given pressure (determined using a digital pressure gauge) from measurements of the volume change in a capillary tube attached to the outlet. The steady-state filtrate flux was evaluated at several applied pressures, with the data analyzed using the Kedem-Katchalsky equation (Equation 2.2). The 30 kDa Ultracel membranes used in this work had $\sigma_0 > 0.99$ for the 142 kDa monoclonal antibody. The osmotic pressure was calculated from the value of the applied pressure at which $J_v = 0$ as determined from a linear regression fit to the flux versus pressure data.

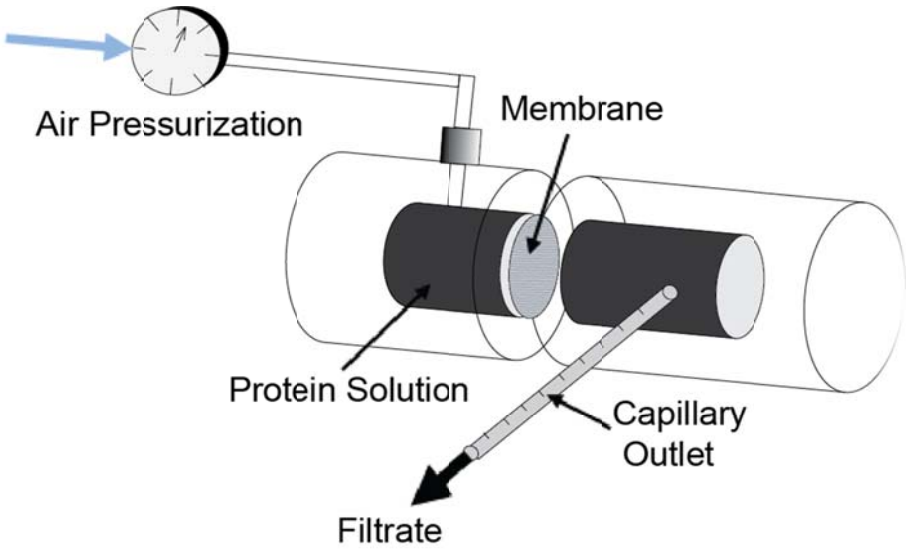

Figure 4.1. Schematic drawing of the membrane osmometer.

The membrane osmometer provided highly accurate data at low to moderate protein concentrations, but was difficult to use at very high antibody concentrations due to the long time required for the flux to obtain its steady-state value. The osmotic pressure of the more highly concentrated antibody solutions was instead evaluated using a stirred ultrafiltration cell (Millipore Corp.) following the approach described by Perkins et al. [95]. Data were obtained with a 10 kDa Ultracel^{TM} membrane (Millipore Corp., Bedford, MA). A 2 mm diameter capillary tube was connected to the filtrate exit port. The stirred cell was air pressurized, with the pressure manually adjusted until there was no movement of the meniscus in the capillary (corresponding to $J_v = 0$).

4.2.2 Protein Charge

The net protein charge in the different buffer conditions was evaluated from electrophoretic light scattering data obtained using a Malvern Zetasizer Nano (Worcestershire, UK). In contrast to titration, the electrophoretic light scattering data provide a direct measure of the protein mobility including the effects of anion (or cation) binding in the different buffer solutions. 5 g/L solutions of the monoclonal antibody were loaded in clear disposable capillary cells (Malvern, DTS 1061). The electrophoretic mobility was determined by Laser Doppler Velocimetry at constant voltage, with results reported as an average over at least 20 runs using five repeat measurements for each buffer condition. The measured electrophoretic mobility (μ_E) was used to evaluate the protein zeta potential (ζ) using Henry's equation (Equations 2.23 and 2.24) as explained in Section 2.4.2. The net protein charge (Z) was then evaluated directly from the measured zeta potential (ζ) using Equation 2.3 and 2.25 which gives [100]:

$$Z = \frac{4\pi\varepsilon r_s\left(1+\kappa r_s\right)}{e}\zeta \tag{4.1}$$

where Equation (4.1) is developed for a uniformly charged sphere at small surface potentials; the maximum value of ζ in our system was less than 13 mV.

4.2.3 Self-Interaction Chromatography

Self-interaction chromatography (SIC) was initially introduced by Patro and Przybycien [77] and was further developed by Tessier et al. [89] as a method to evaluate protein–protein interactions. The monoclonal antibody was randomly immobilized on the

surface of a Toyopearl AF Formyl 650M resin (Tosoh Bioscience LLC, Tokyo, Japan) by reaction of the free amine groups on the antibody with the reactive aldehyde group on the resins [101]. The surface-modified resin particles were packed into a Tricorn® 5/50 column (GE Healthcare, Tyron PA) connected to an Agilent 1100 series chromatography system (Agilent Technologies, Palo Alto, CA). A 50 μm sample of the antibody solution was injected into the column after it was equilibrated with the desired buffer, with the retention volume evaluated at an eluent flow rate of 0.1 mL/min. The second virial coefficient (B_2) was evaluated from the difference in the measured retention volume for the antibody and for a 50 kDa molecular weight dextran with hydrodynamic volume equivalent to that of the antibody following the procedures developed by Tessier [101]. Additional details on the self-interaction chromatography are provided in Chapter 5.

4.3 Results and Analysis

4.3.1 Osmotic Pressure

Typical data for the filtrate flux as a function of the applied transmembrane pressure in the membrane osmometer are shown in Figure 4.2 for antibody concentrations of 19, 36, and 61 g/L. In each case, the flux was evaluated until the system attained a steady-state, requiring as much as 150 min for the more highly concentrated antibody solutions. This long equilibration time is associated with the development of the concentration polarization boundary layer adjacent to the membrane.

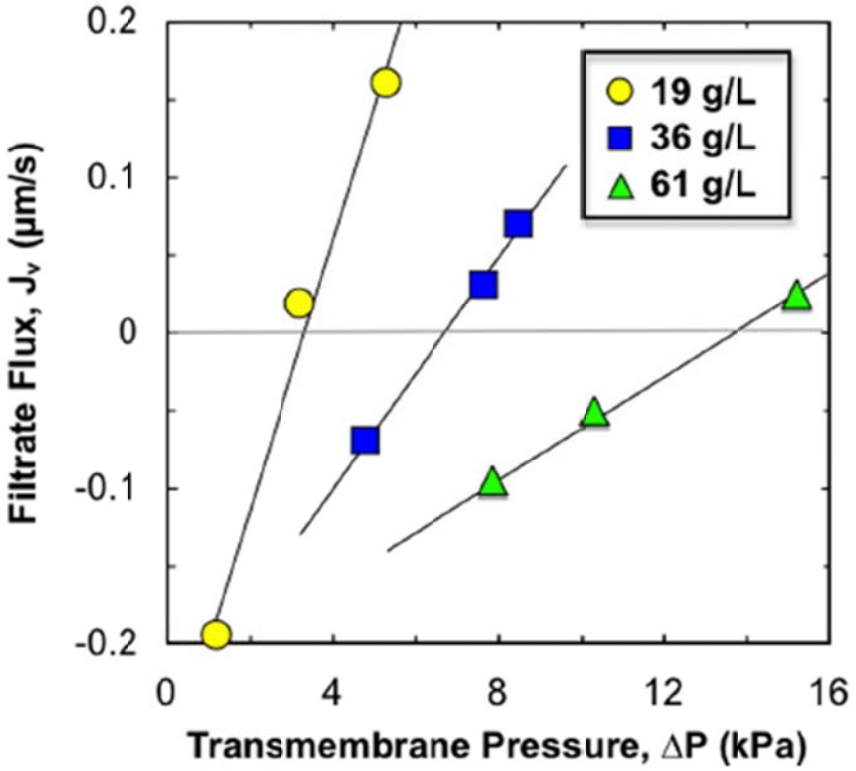

Figure 4.2. Filtrate flux as a function of applied transmembrane pressure in the membrane osmometer for monoclonal antibody solutions in 5 mM acetate buffer with 10 mM NaCl at pH 5. Lines are linear regression fits to the data. The intercepts on the x-axis correspond to the osmotic pressure.

The filtrate flux data were analyzed using the Kedem-Katchalsky equations (Equation 2.2), with the slope and intercept evaluated from a linear regression fit to the data (with r^2 values greater than 0.98 at each concentration). The osmotic pressure difference across the membrane was then calculated from the x-intercept (equal to the ratio of the best fit values of the y-intercept to the slope assuming that the osmotic reflection coefficient is equal to one) giving $\Delta\Pi$ = 3.1 ± 0.2 kPa (0.45 psi) for the 19 g/L solution and 14 ± 1 kPa (2 psi) for the 61 g/L solution. The measured osmotic pressure difference across the membrane is equal to the osmotic pressure corresponding to the concentration of the antibody solution

in the feed chamber since the antibody concentration in the filtrate is zero, i.e., $\Pi_{filtrate} = 0$). The measured osmotic pressure does depend on the salt concentration due to the Donnan effect, the unequal partitioning of the charged ions between the two chambers due to the presence of the charged protein. This is discussed in more detail subsequently.

The reduction in slope with increasing protein concentration is due to concentration polarization effects in the upstream chamber of the membrane as discussed by Opong and Zydney [41]. Concentration polarization causes the protein concentration at the membrane surface (C_w) to be greater than the protein concentration in the bulk solution (C_b), with the magnitude of this effect related to the bulk mass transfer coefficient in the solution chamber. The actual osmotic pressure difference across the membrane, which is determined by C_w (and not C_b), can be evaluated using the first term in a Taylor series expansion around the bulk protein concentration as:

$$\Pi_w = \Pi_b + \left(\frac{d\Pi}{dC}\right)_{C_b} \left(C_w - C_b\right) \tag{4.2}$$

where C_w can be found in terms of the bulk mass transfer coefficient, filtrate flux, and C_b using the first term in the Taylor series expansion for the simple stagnant film model (Equation 2.11):

$$C_w = C_b + C_b\left(\frac{J_v}{k}\right) \tag{4.3}$$

Substituting Equations (4.2) and (4.3) into Equation (2.2) gives the following expression for the flux:

$$J_v = \left[\frac{L_P}{1 + \frac{L_p C_b}{k} \left(\frac{d\Pi}{dC} \right)_{C_b}} \right] \left[\Delta P_{TM} - \Delta \Pi_b \right] \tag{4.4}$$

Thus the effective permeability, $L_{p,eff}$ as given by the expression in the brackets that multiples ΔP_{TM} - $\Delta \Pi_b$, decreases with increasing bulk protein concentration due to concentration polarization. Note that the measured values of the osmotic pressure are unaffected by any concentration polarization effects since polarization disappears in the limit of zero flux [41].

The measured values of the protein osmotic pressure in acetate buffer at pH 5 are summarized in Figure 4.3 for solutions containing 10, 20, and 100 mM NaCl. The data at low antibody concentrations were obtained in the membrane osmometer (open symbols) while the results at high concentrations are primarily from the stirred ultrafiltration cell (filled symbols). The data in the two systems are in good agreement, providing further support for the methodology used to evaluate the osmotic pressure over the full range of antibody concentrations.

The osmotic pressure increases strongly at very high protein concentrations, attaining a value above 60 kPa at a concentration of 230 g/L in the 10 mM solution. The osmotic pressure decreases with increasing solution ionic strength due to the reduction in repulsive intermolecular interactions. This is discussed in more detail subsequently. The measured osmotic pressure in the 100 mM NaCl solution at an antibody concentration of 195 g/L is 23 kPa, which is considerably larger than the value of 6.5 kPa reported by Perkins et al. [95] at relatively similar conditions (pH 5, 150 mM acetate buffer). The

source of these differences is unknown but is likely related to the different physical characteristics of the monoclonal antibodies examined in these studies. Note that Perkins et al. provide no information on the nature of the antibody used in their work, including either the pI or net protein charge.

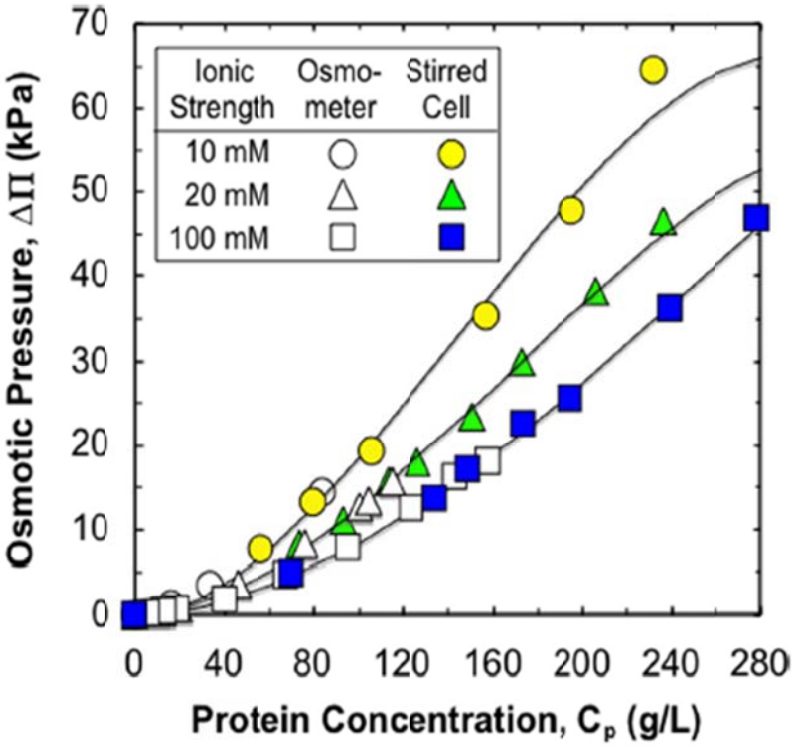

Figure 4.3. Osmotic pressure at pH 5 as a function of protein concentration for solutions of the monoclonal antibody in acetate buffer with different NaCl concentrations. Solid curves are model calculations given by Equation (4.5).

Figure 4.4 shows data for the osmotic pressure at different pH in the presence of 20 mM NaCl; 5 mM acetate buffer was used at pH 5 while 5 mM phosphate buffer was used at pH 6 and pH 7. The osmotic pressure decreases with increasing pH, i.e., as the pH

approaches the protein isoelectric point (pI = 8.16). This effect is quite pronounced at high antibody concentrations, with the osmotic pressure decreasing from more than 55 kPa at pH 5 to less than 20 kPa at pH 7 for an antibody concentration of approximately 250 g/L. The osmotic pressure data at pH 7 are nearly linear over the entire concentration range, while the results at pH 5 are highly concave up. This is discussed in more detail subsequently.

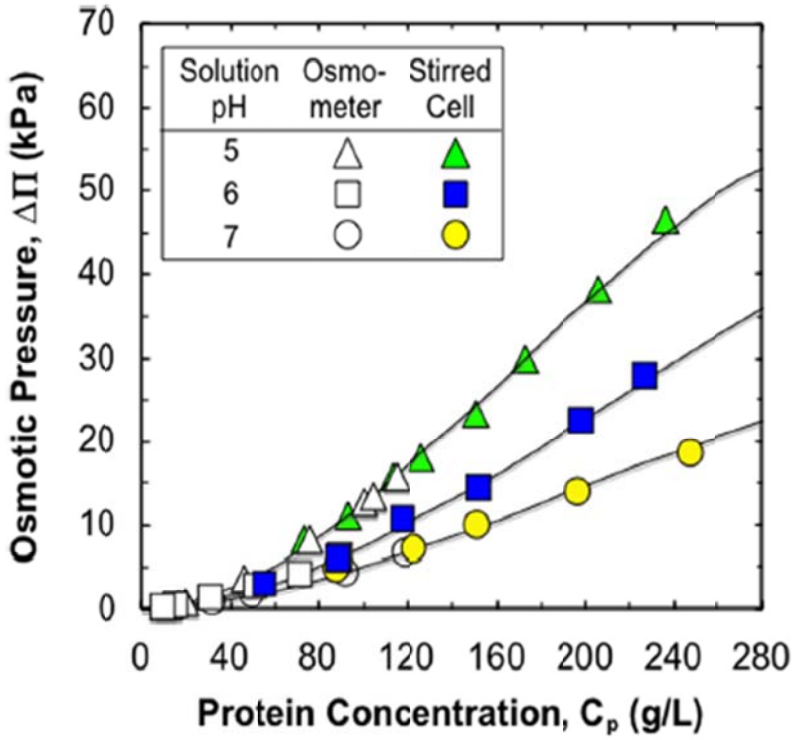

Figure 4.4. Osmotic pressure as a function of protein concentration at pH 5 (acetate buffer) and pH 6 and 7 (phosphate buffer) with 20 mM ionic strength. Solid curves are model calculations given by Equation (4.5).

4.3.2 Virial Coefficients

The osmotic pressure of the concentrated antibody solutions is due to the sum of the osmotic pressure associated with intermolecular interactions between the proteins and solvent (often referred to as the colloidal osmotic pressure or the oncotic pressure) and the osmotic pressure arising from the difference in micro-ion concentrations across the membrane (the Donnan contribution). The Donnan contribution is directly related to the net protein charge (Z) and the resulting uneven distribution of salt ions between the two chambers needed to ensure electroneutrality on both sides of the membrane. The data in Figures 4.3 and 4.4 were analyzed using the expression [93]:

$$\Pi = RT\left\{2\left[\left(\frac{ZC_p}{2M_p}\right)^2 + m_s^2\right]^{\frac{1}{2}} - 2m_s\right\} + RT\left(B_1C_p + B_2C_p^2 + B_3C_p^3 + etc\right) \qquad (4.5)$$

where C_p and M_p are the protein concentration and molecular weight and m_s is the molar salt concentration. The B_i are virial coefficients; B_1 is directly related to the effective protein molecular weight while B_2 and B_3 can be expressed as integrals over the potential energy of interaction between the proteins [31, 93].

The oncotic pressure was calculated from the measured osmotic pressure by subtracting off the Donnan contribution based on the first term in Equation (4.5) with the net protein charge in the different buffer conditions given in Table 4.1. The Donnan contribution was relatively small at high ionic strength and at pH near the protein isoelectric point, but could be as large as 17 kPa at low salt and pH 5. The results for the

different ionic strength solutions at pH 5 in acetate buffer are shown in Figure 4.5 as the reduced oncotic pressure:

$$\frac{\Pi_{onc}}{C_p} = RT\left(B_1 + B_2 C_p + B_3 C_p^2 + etc\right) \tag{4.6}$$

The data at the different ionic strength have a very similar intercept on the y-axis, consistent with a constant value of the first virial coefficient (B_1), independent of solution ionic strength. The data at low antibody concentrations are linear, with the slope decreasing with increasing ionic strength. The oncotic pressure data at high antibody concentrations are clearly non-linear due to the significant contributions of the higher order terms in the virial expansion (Equations 4.5 and 4.6).

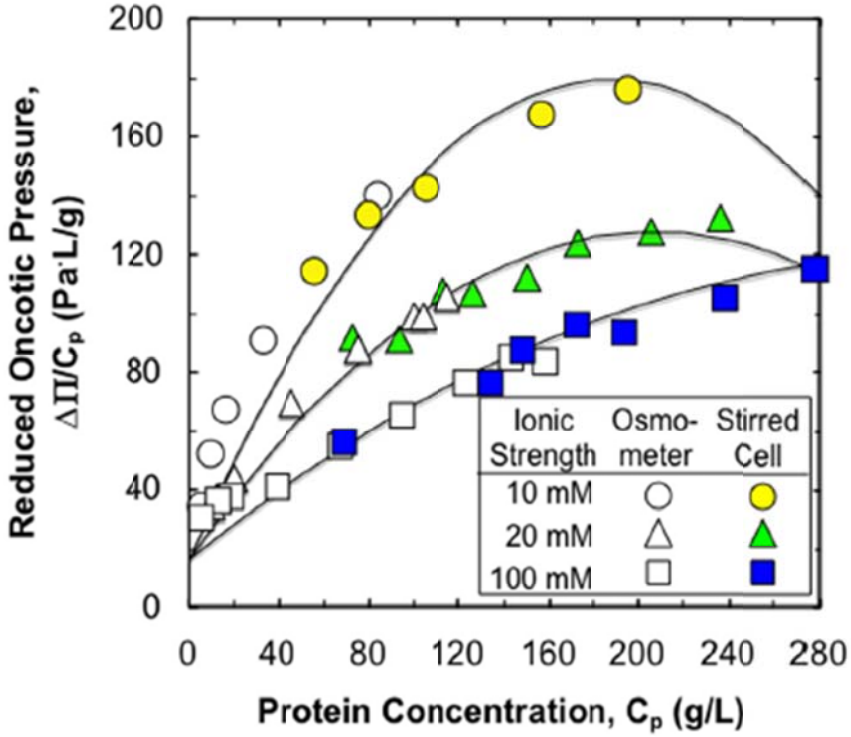

Figure 4.5. Reduced oncotic pressure as a function of protein concentration for monoclonal antibody solutions in 5 mM acetate buffer at pH 5 with different NaCl concentrations. Solid curves are model calculations given by Equation (4.6).

The best fit values of the second and third virial coefficients were evaluated by fitting the reduced oncotic pressure data to a second order polynomial using Mathematica with B_1 set equal to $1/M_p$. The antibody molecular weight was taken as that of the protein monomer (M_p = 142 kDa) since the concentration of dimers and higher order oligomers was less than 3% at all buffer conditions. Model fits constructed with B_1 taken as an adjustable parameter gave effective protein molecular weights between 86 and 129 kDa. However, the use of B_1, B_2, and B_3 as adjustable parameters significantly reduced the accuracy of the calculated values of the higher order virial coefficients. The solid curves

in Figure 4.3 to 4.5 are the model calculations given by Equation (4.5) using the best fit values of B_2 and B_3 given in Table 4.1. The error limits were determined using Mathematica (for the osmometry data) or by propagation of error analysis (for the SIC).

Table 4.1 Monoclonal antibody virial coefficients and charge in 5 mM phoshpate buffer at different pH and salt concentrations.

Buffer Condition	B_2 (osmometry) $\left(\frac{\mathbf{mL.mol}}{\mathbf{g^2}}\right) \times \mathbf{10^4}$	B_2 (SIC) $\left(\frac{\mathbf{mL.mol}}{\mathbf{g^2}}\right) \times \mathbf{10^4}$	B_2 (theory) $\left(\frac{\mathbf{mL.mol}}{\mathbf{g^2}}\right) \times \mathbf{10^4}$	B_3 (osmometry) $\left(\frac{\mathbf{mL^2.mol}}{\mathbf{g^3}}\right) \times \mathbf{10^7}$	Z
pH 5, 10 mM	7.1 ± 1.3	3.5 ± 0.3	3 ± 0.2	- 19 ± 7	12 ± 1
pH 5, 20 mM	4.4 ± 0.4	3.1 ± 0.3	2 ± 0.2	-11 ± 2	14 ± 1
pH 5, 100 mM	2.5 ± 0.4	2.4 ± 0.3	0.8 ± 0.2	-4 ± 2	24 ± 1
pH 6, 20 mM	2.6 ± 0.3	2.2 ± 0.3	0.9 ± 0.2	-4 ± 2	6 ± 1
pH 7, 20 mM	1.7 ± 0.1	1.9 ± 0.3	0.3 ± 0.2	-3 ± 1	3 ± 1

* Error limits on B_2 and B_3 were determined using Mathematica (for the osmotic pressure data) or by propagation of error analysis (for Z values).

The discrepancies between the model and the data are magnified in Figure 4.5 due to the use of the reduced oncotic pressure since this parameter is calculated by dividing the osmotic pressure by the protein concentration in the solution. The overall fit could also be improved by including higher order terms in the virial expansion (Equation 4.6). The best fit value of the second virial coefficient decreases with increasing ionic strength, going from a value of $B_2 = 7.1 \pm 1.3 \times 10^{-4}$ mL.mol/g^2 at pH 5 and 10 mM NaCl to 2.4 ±

0.4×10^{-4} mL.mol/g^2 in the 100 mM NaCl solution, consistent with a reduction in the magnitude of the repulsive interactions due to electrostatic shielding.

The best fit value of B_2 at pH 7 (approximately one pH unit below the pI of 8.16) is $1.7 \pm 0.1\times10^{-4}$ mL.mol/g^2 which is larger than the purely steric contribution to the second virial coefficient [102]:

$$B_2 = \frac{16}{3}\left(\frac{\pi r_s^3 N_{Av}}{M_p^2}\right) \tag{4.7}$$

where N_{Av} is Avogadro's number. Equation (4.7) gives $B_2 = 0.8\times10^{-4}$ mL mol / g^2 using $r_s = 5.4$ nm where the effective protein radius was evaluated using size exclusion chromatography using dextran standards for the calibration [103]. This value is in good agreement with literature data [104]. The difference between the experimental value of B_2 and the purely steric value is likely due to the presence of repulsive electrostatic interactions in the low ionic strength solution (20 mM) in combination with the non-spherical shape of the antibody. For example, Vilker et al. [31] showed that the excluded volume term for a prolate ellipsoid with aspect ratio of 3.2 was 42% larger than that for a hard sphere with equivalent volume.

In contrast to the results for the second virial coefficients, the third virial coefficients are all negative (leading to the downward curvature in Figure 4.5), which suggests an attractive (multi-body) interaction at very high protein concentrations. This is consistent with the reversible self-association of both serum IgG [87] and IgG_1 monoclonal antibodies [105] at high protein concentrations observed in sedimentation equilibrium and light scattering experiments, respectively. The absolute value of B_3

decreases with increasing ionic strength and solution pH, suggesting that this attraction may be electrostatic in nature. This is discussed in more detail subsequently.

The fourth column in Table 4.1 shows model calculations for the second virial coefficients developed using the potential of mean force for charge–charge electrostatic interactions between hard spheres [106]:

$$B_2 = B_{HS} + 2\pi \int_{2r_s}^{\infty} \left\{ 1 - \exp\left[\frac{-W_{ij}(r)}{k_B T} \right] \right\} r^2 dr \tag{4.8}$$

where k_B is Boltzmann's constant, T is the absolute temperature, r is the radial distance measured from the center of the protein, and W_{ij} is the potential of mean force:

$$W_{ij}(r) = \frac{(Ze)^2}{\varepsilon r} \times \frac{\exp[-\kappa(r - 2r_s)]}{(1 + \kappa r_s)^2} \tag{4.9}$$

where Z is the protein charge, e is the electronic charge, ε is the dielectric constant for the media, and κ is the inverse Debye length. Equations (4.8) and (4.9) have been used extensively for the evaluation of the second virial coefficient of a range of proteins [31, 92, 93]. The calculated values of B_2 are significantly smaller than the experimental results. The discrepancy at high pH and high salt are likely due to errors in the evaluation of the hard-sphere contribution to the second virial coefficient as discussed previously. The discrepancy at pH 5 and low ionic strength may be due to the breakdown in the Debye–Huckel approximation (assumption of low surface potential) that is inherent in the development leading to Equation (4.9).

4.3.3 Self-Interaction Chromatography

The second virial coefficients for the monoclonal antibody in different buffer conditions were also evaluated using self-interaction chromatography (SIC) based on the difference in retention volume of the antibody when interacting with the protein immobilized on the resin (V_r) and when eluting under non-interacting conditions (V_o):

$$k' = \frac{V_r - V_0}{V_0} \tag{4.10}$$

as discussed in Chapter 5. The second virial coefficient is linearly proportional to k' [89, 101]:

$$B_2 = B_{HS} - \frac{k'}{\rho_s \phi} \tag{4.11}$$

where B_{HS} is the protein excluded volume (or hard sphere) contribution given by Equation (4.7), ϕ is the effective phase ratio (equal to the accessible surface area divided by the mobile phase volume), and ρ_s is the amount of immobilized protein per unit pore surface area (evaluated as $\rho_s = 1.4\times10^{15}$ molecule/m^2 from a mass balance on the protein solution used for the immobilization reaction). ϕ was evaluated as 10.9 m^2/mL following the procedures and data in DePhillips and Lenhoff [107] as discussed in Chapter 5. SIC measurements were performed in triplicate with the retention volume calculated from the location of the peak maximum.

The calculated values of the second virial coefficients from the SIC data are summarized in the third column of Table 4.1. The B_2 values determined from SIC are in excellent agreement with results from the osmotic pressure data at pH 6 and 7 and at pH

5 and 100 mM NaCl. However, the SIC values are considerably smaller than those determined from osmometry at pH 5 and low salt concentration. This under-estimation of the second virial coefficient in SIC can arise from the complete exclusion of the antibody from the smaller pores due to the very strong electrostatic repulsion exclusion effects between the protein in solution and the protein immobilized on the resin under these conditions. This is discussed in more detail in Chapter 5.

4.3.4 Excipients

A number of different excipients are often added to concentrated antibody solutions to increase protein stability, reduce dimer formation, and prevent protein aggregation [108]. Experimental studies were performed to evaluate the effects of arginine-HCl, sucrose, and L-proline on both the osmotic pressure and the second virial coefficient. Data were obtained at pH 5 using sodium acetate buffer with 20 mM NaCl and a 300 mM concentration of the desired excipient with results shown in Figure 4.6. The osmotic pressure was reduced in the presence of all three excipients, with the most significant effects seen at antibody concentrations greater than 150 g/L. For example, the osmotic pressure at an antibody concentration of approximately 240 g/L varied from 41 kPa in the presence of arginine-HCl to 44 kPa in presence of L-proline to 48 kPa in presence of sucrose compared to 50 kPa in the pure acetate buffer.

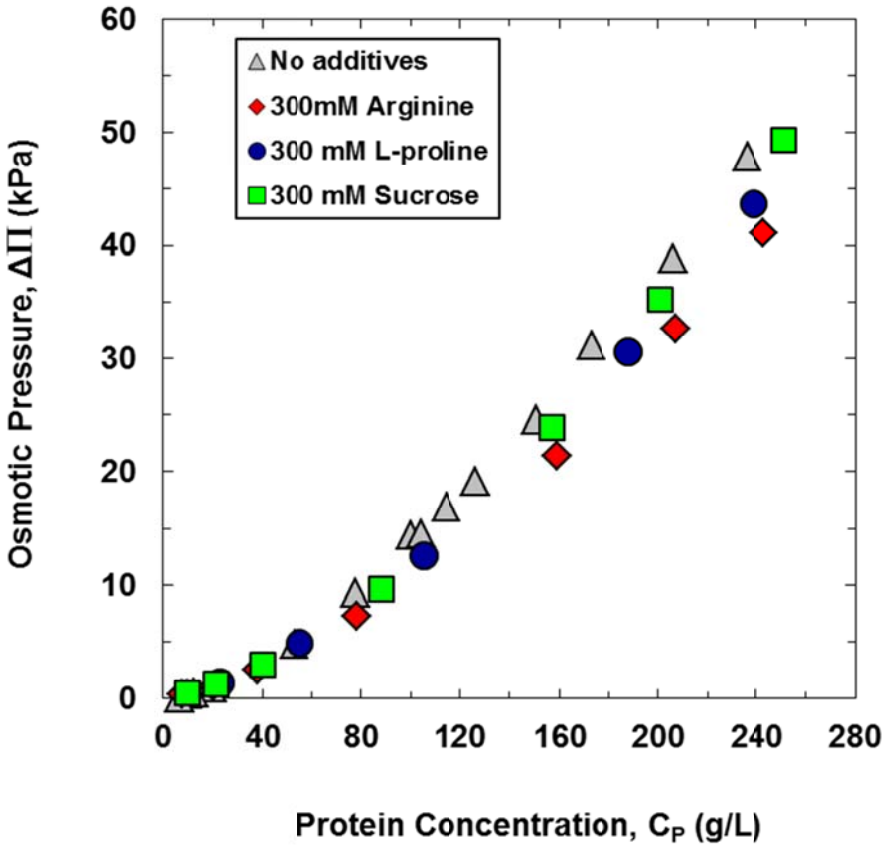

Figure 4.6. Osmotic pressure as a function of protein concentration at pH 5 (acetate buffer) with 20 mM ionic strength and in the presence of 300 mM of different excipients.

The calculated values of the second and third virial coefficients in the presence of the different excipients are summarized in Table 4.2. The addition of sucrose and L-proline caused a small reduction in the B_2 values determined from membrane osmometry, although this effect was of only marginal statistical significance. However, this reduction is more pronounced in the case of arginine-HCl with B_2 determined from membrane osmometry decreasing from 4.4×10^{-4} mL.mol/g^2 to 3.5×10^{-4} mL.mol/g^2. There was a

small reduction in the magnitude of the third virial coefficient in the presence of all 3 excipients, which would be consistent with a small reduction in the attractive multi-body interactions, although this effect was again only of marginal statistical significance. Additional studies would be required to evaluate the significance of this effect on the stability and physical properties of these highly concentrated antibody solutions. The effect of these excipients on the antibody viscosity is discussed in Chapter 6.

Table 4.2. Effect of excipients on the virial coefficients for the monoclonal antibody.

Excipient	B_2 (osmometry) $\left(\frac{\mathbf{mL.mol}}{\mathbf{g^2}}\right) \times \mathbf{10^4}$	B_2 (SIC) $\left(\frac{\mathbf{mL.mol}}{\mathbf{g^2}}\right) \times \mathbf{10^4}$	B_3 (osmometry) $\left(\frac{\mathbf{mL^2.mol}}{\mathbf{g^3}}\right) \times \mathbf{10^7}$
None	4.4 ± 0.4	3.1 ± 0.3	-11 ± 2
Sucrose	4.0 ± 0.4	2.8 ± 0.3	-9 ± 2
L-Proline	4.1 ± 0.1	2.8 ± 0.3	-10 ± 2
Arginine-HCl	3.5 ± 0.1	2.5 ± 0.3	- 9 ± 2

* Error limits on B_2 and B_3 were determined using Mathematica (for the osmotic pressure data) or by propagation of error analysis (for Z values).

4.4 Conclusions

The experimental data presented in this chapter provide the most extensive measurements of the osmotic pressure of a highly purified monoclonal antibody solution, including results at very high protein concentrations and over a range of pH and ionic strength. The osmotic pressures at typical formulation conditions (pH 5 and 10 mM ionic strength) are substantially larger than those reported previously at pH 7 and high ionic strength. For example, the osmotic pressure at 230 g/L was 45 kPa compared to a value

of only 6.9 kPa from Yousef et al. [98] for serum IgG at a similar concentration but at pH 7.4 and 130 mM NaCl. However the serum IgG examined by Yousef et al. [98] was polyclonal with a range of isoelectric points from 5.8 – 8.5. Note that the calculated value of the Donnan contribution for the antibody examined in this work at pH 5 and 10 mM NaCl was 7.0 kPa, which is larger than the measured osmotic pressure reported by Perkins et al. [95] under similar conditions.

The calculated values of the second virial coefficient determined from the osmotic pressure data (after subtracting off the Donnan contribution) were in relatively good agreement with independent measurements of the second virial coefficient evaluated using self-interaction chromatography. The differences seen at very low ionic strength are likely due to the complete exclusion of the protein molecules from the smaller pores in the SIC resin.

The osmotic pressure data at high protein concentrations can also be used to evaluate the third virial coefficient, which is usually inaccessible with other experimental methods used to study protein–protein interactions. The plots of the reduced osmotic pressure are clearly concave down, particularly at low ionic strength, consistent with negative values of the third virial coefficient. Previous work by Scherer et al. [105] showed that a plot of the reciprocal of the apparent molecular weight of an IgG1 monoclonal antibody determined by light scattering was concave down at low ionic strength (provided in the supplementary material of that reference), consistent with a negative value of the third virial coefficient, which the authors modeled using an adhesive hard-sphere model. These attractive interactions likely arise from

configurations in which local oppositely charged regions of different antibodies interact with high geometric complementarity.

The magnitude of the attractive third virial coefficient decreased with increasing ionic strength and solution pH and was slightly reduced in the presence of arginine, an excipient commonly used to stabilize antibody formulations. However, the effect of these excipients on the osmotic pressure was relatively small compared to the two-fold reduction in viscosity reported by Maeder et al. [108] for a highly concentrated polyclonal immunoglobulin solution. The effects of different excipients on the viscosity of these highly concentrated antibody solutions is discussed in more detail in Chapter 6.

Chapter 5

Self-interaction Chromatography for Evaluating Intermolecular Interactions via Second Virial Coefficient Measurement

Note: Most of material presented in this chapter was previously published in: E. Binabaji, S. Rao, A.L. Zydney, Improved Method for Evaluating the Dead Volume and Protein–Protein Interactions by Self-Interaction Chromatography, Analytical Chemistry, 85 (2013) 9101-9106.

5.1 Introduction

Self-interaction chromatography (SIC) is a widely-used method for studying protein–protein interactions that are important in protein formulation [18, 109-111], crystallization [83, 112-116], purification [80, 83, 109-116], and in understanding protein aggregation in both *in vitro* and *in vivo* systems. Self-interaction chromatography was first introduced by Patro and Przybycien [77]. Tessier et al. [89] subsequently showed that the measured retention coefficient (k') could be used to calculate the second virial coefficient (B_2) as:

$$B_2 = B_{HS} - \frac{k'}{\rho_s \phi} \tag{5.1}$$

where ϕ is the effective phase ratio, equal to the accessible surface area divided by the mobile phase volume, ρ_s is the amount of protein immobilized per unit pore surface area, and B_{HS} is the hard sphere contribution to the virial coefficient. B_2 provides a measure of the potential of mean force for two-body interactions, which is directly related to the magnitude of the intermolecular interactions between proteins in the solution of interest.

SIC has been used to evaluate the second virial coefficient for BSA [114, 115], lysozyme [89, 111, 112, 117, 118], α-chymotrypsinogen [89], and monoclonal antibodies [110, 113, 119] among others, with results in good agreement with independent estimates of B_2 from static light scattering [120], neutron scattering [120], small-angle x-ray scattering [84, 85, 121], low-angle laser light scattering [122, 123], size-exclusion chromatography [124], and membrane osmometry. In comparison to other methods, SIC uses much smaller quantities of protein (typically less than 1 mg), it generally requires less time, and it is easily automated. Recent studies have examined a number of factors that influence the performance of SIC including the degree of immobilization [89, 118], the possibility of multi-body interactions [118], the properties of the basin resin [112], and the orientation of the immobilized protein [125].

One of the other challenges in evaluating the second virial coefficient using SIC is the evaluation of the dead volume, V_o, in the expression for the retention coefficient:

$$k' = \frac{V_r - V_0}{V_0} \tag{5.2}$$

where V_r is the retention volume of the protein of interest and V_o is the retention volume of a non-interacting molecule of the same size as the protein. It is not possible to evaluate V_o from data with a small (non-interacting) solute (e.g., acetone) because the small solute

can access much more of the pore space than the protein due to the large difference in physical size. This effect becomes even more pronounced when using SIC for large proteins like monoclonal antibodies.

Tessier et al. [89, 114] evaluated V_o by multiplying the measured retention volume for acetone by the ratio of the retention volumes for the protein and acetone in a second column containing identical chromatographic particles but without any immobilized protein:

$$V_0 = V_{acetone}\left(\frac{V'_{protein}}{V'_{acetone}}\right) - V_{immobilized} \tag{5.3}$$

where the primes refer to the measured retention volumes in the dead column and $V_{immobilized}$ is the volume occupied by the immobilized protein molecules in the first column, typically estimated by dividing the measured mass of immobilized protein by the protein density .

Although Equation (5.3) has been widely used to evaluate V_o in previous studies of SIC, there are a number of concerns with this approach. First, Equation (5.3) requires the use of a second chromatographic column, significantly increasing the time for the experimental measurements. Second, the use of the ratio of the retention volumes in the second column as a correction factor is only appropriate if there are no interactions between the protein and the stationary phase (in the absence of immobilized protein) and if the two columns have equivalent packing characteristics. Third, the estimation of the volume of immobilized protein requires an accurate value for the protein density.

The objective of the studies described in this chapter was to develop a more accurate approach for evaluating the dead volume in SIC through the use of a dextran

standard, with the same effective size as the protein, as the non-interacting molecule. This completely eliminates the need for a second column, reducing the experimental time and improving the accuracy of the SIC measurements. The effectiveness of this approach was demonstrated for a monoclonal antibody under conditions dominated by repulsive interactions, with the calculated values of the second virial coefficient in good agreement with independent measurements obtained by membrane osmometry.

5.2 Experimental Procedures

5.2.1 Protein and dextran

Experiments were performed using a highly purified monoclonal antibody provided by Amgen, Inc. with molecular weight of 142 kDa and isoelectric point of 8.16. The antibody was stored at -80 °C and slowly thawed prior to use. The antibody was placed in the desired buffer by diafiltration through a fully retentive Ultracel™ composite regenerated cellulose membrane with 10 kDa nominal molecular weight cut-off (Millipore Corp., Bedford, MA) as described in Chapter 3. Narrow dextran standards with polydispersity < 1.5 and with molecular weights of 33, 42, 62, and 80 kDa (from American Polymer Standards, Mentor, OH) and 50 kDa (Sigma Aldrich) were dissolved in the appropriate buffer solution.

Buffered salt solutions were prepared by dissolving appropriate amounts of sodium acetate (Sigma, S7670), sodium phosphate monobasic (Sigma, S9638), and / or sodium phosphate dibasic (Sigma, S7907) in deionized water obtained from a NANOpure® Diamond water purification system (Barnstead Thermolyne Corporation,

Dubuque, IA) with a resistivity greater than 18 MΩcm. The ionic strength was adjusted using NaCl (BDH Chemicals, BDH0286), and the pH was adjusted using 0.1 N NaOH or HCl as needed.

Antibody concentrations were determined spectrophotometrically using a SPECTRAmax Plus 384 UV-vis spectrophotometer (MD Corp., Sunnyvale, CA) with the absorbance measured at 280 nm. Samples were diluted as needed to ensure that the measured absorbance was in the linear range (absorbance between 0.1 and 0.4). Actual concentrations were evaluated by comparison of the absorbance with that of known protein standards, with results reported as the mean ± standard deviation for a minimum of four repeat measurements.

5.2.2 Column preparation

The monoclonal antibody was randomly immobilized on the surface of a Toyopearl AF Formyl 650M resin (Tosoh Bioscience LLC, Tokyo, Japan) by reaction of the free amine groups with the reactive aldehyde group on the resins [114]. Approximately 3 mL of the resin were first washed four times using 50 mL of deionized water with the particles collected by centrifugation. The resin particles were then rinsed with 50 mL of 0.1 M potassium phosphate buffer at pH 7.5. The collected particles were added to 10 mL of a 5 g/L solution of the monoclonal antibody in 0.1 M potassium phosphate buffer at pH 7.5. Approximately 90 mg of sodium cyanoborohydride was added to the solution (with extreme caution) to initiate the reaction. The mixture was incubated at room temperature with constant agitation provided by a rotary shaker

(Innova 4000, New Brunswick Scientific). The amount of protein immobilized on the particles was calculated from the difference in protein concentration in the reaction solution before and after reaction.

The particles with immobilized protein were washed four times with 200 mL of phosphate buffer. The particles were then added to a 15 mL solution of 1 M ethanolamine at pH 8 to cap any unreacted aldehyde groups. Approximately 20 mg of sodium cyanoborohydride was also added to the mixture to initiate the reaction. The reaction mixture was incubated at room temperature for four hours, and the particles were then washed again with 1 M NaCl at pH 7 to remove any unbound protein.

Approximately 2.5 mL of resin particles were prepared as a 50% slurry and packed into a Tricorn® 5/50 column (GE Healthcare, Tyron PA) at a flow rate of 3 mL/min for 15 min, with the flow rate reduced and maintained at 0.5 mL/min for an additional two hours to insure uniform packing. The quality of the column packing was evaluated by injecting a 1% acetone solution; columns were only used if the acetone gave a sharp symmetric Gaussian peak with the peak width (at half height) less than 0.5 mL at an eluent flow rate of 0.1 mL/min.

5.2.3 Self-interaction Chromatography

Self-interaction chromatography was performed using an Agilent 1100 series chromatography system (Agilent Technologies, Palo Alto, CA). The column was first equilibrated with 10 column volumes of the buffer of interest at a flow rate of 0.1 mL/min. A 50 μL sample of the antibody, acetone, or dextran was injected into the

column, with the retention volume evaluated at an eluent flow rate of 0.1 mL/min. The column was then washed with 5 mM phosphate buffer at pH 7 with 1 M NaCl for four column volumes followed by seven column volumes of 5 mM phosphate buffer at pH 7 (with no additional salt) before re-equilibrating with a new buffer. All retention volumes were evaluated in triplicate with results reported as the mean ± standard deviation. The column was stored at 4 ºC when not in use. Data were also obtained with a "dead column" packed with the same particles, with the aldehyde groups capped by reaction with sodium cyanoborohydride and ethanolamine but without any immobilized protein.

The same chromatography system was used for size-exclusion chromatography but with a Superdex^{TM} 200 10/300 GL column (GE Healthcare, 17-5175-01). 50 mM sodium phosphate buffer at pH 7 with 150 mM NaCl was used as the eluent at a flow rate of 0.3 mL/min.

5.3 Results

5.3.1 Dead Volume

Our initial efforts to evaluate the column dead volume (V_o) were based on the use of a "dead column" packed with the Toyopearl AF Formyl 650M resin in which the aldehyde groups were capped by reaction with sodium cyanoborohydride and ethanolamine but without any immobilized protein following the procedures described by Tessier et al. [89]. However, measurements obtained on multiple dead columns, prepared and packed following identical procedures, showed a range of $V'_{protein}/V'_{acetone}$ values from

0.78 to 0.79, resulting in a 0.017 mL difference in the calculated dead volumes given by Equation (5.3). This small (1.7%) variation in the dead volume led to more than a 30% variation in the calculated values of k' (given by Equation 5.2) and in turn the second virial coefficient (given by Equation 5.1).

It is also possible to obtain a rough estimate of the dead volume using a simple partitioning model. The mean value of the acetone retention volume in the dead column was 1.3 mL. The protein retention volume for a resin with uniform cylindrical pores can be estimated as:

$$V'_{protein} = V'_{pore}\left(1 - \frac{r_s}{R}\right)^2 + V'_{void} \tag{5.4}$$

where r_s is the protein radius and R is the pore radius. Equation (5.4) gives $V'_{protein}$ = 1.21 mL using r_s = 5.43 nm for the monoclonal antibody and R = 73.9 nm for the 650M resin [114] assuming that the acetone volume is equally distributed between the pore space (V'_{pore}) and the inter-particle void volume (V'_{void}). Similar results were obtained by integrating over the pore size distribution [107]. Although Equation (5.4) is an only an approximation, the very large difference between the calculated value of $V'_{protein}$ and the value measured experimentally using the dead column ($V'_{protein}$ = 1.02 mL) suggests that the use of the dead column may not provide an accurate estimate of $V'_{protein}$. This could be due to the presence of non-specific interactions between the antibody and the resin in the dead column.

A similar approach can be used to estimate the accuracy of the dead volume calculated using Equation (5.3). The surface coverage of the immobilized protein was

evaluated as 13% of a monolayer based on the mass uptake of antibody during the immobilization reaction using an internal surface area per settled particle volume of 9 m^2/mL based on the inverse size exclusion chromatography data presented by DePhillips and Lenhoff [108]. The column containing the resin with immobilized protein is assumed to be identical to the dead column with V_{void} = 0.65 mL and V_{pore} = 0.62 mL accounting for the reduction in pore volume associated with the immobilized protein. The dead volume for this column can then be evaluated theoretically using Equation (5.4) as V_o = 1.18 mL using R = 68.5 nm. In contrast, the calculated value of V_o from Equation (5.3) is 0.96 mL using the experimental values for $V'_{protein}$ and $V'_{acetone}$. Similar calculations using the theoretical values for $V'_{protein}$ give V_o = 1.15 mL, both of which are in poor agreement with the model calculation.

An alternative approach to evaluating the dead volume in the protein-immobilized column is to use a non-interacting solute that has the same effective volume as the protein of interest. Dextrans have been used extensively as non-interacting solutes in inverse size exclusion chromatography to evaluate the pore size distribution of different chromatographic resins [107], suggesting that they might be appropriate in SIC as well. Previous studies of the effects of dextran on protein solubility [126] are consistent with an excluded volume effect, suggesting that there are no specific dextran-protein interactions in these systems. Table 5.1 shows data for the measured retention volume of a series of narrow molecular weight dextran standards in a Superdex^{TM} 200 resin packed in a 10/300 GL column. The final column shows the calculated value of the Stokes radii for the different dextrans evaluated using the correlation [74]:

$$r_s = 0.0488 MW^{0.437} \tag{5.5}$$

The last row of Table 5.1 shows results for the monoclonal antibody. The retention volume for the antibody is essentially identical to that of the 50 kDa dextran standard which has a weight average molecular weight of 48,600 Da; the Stokes radius for the antibody was evaluated as r_s = 5.43 nm by interpolation of the size exclusion chromatography results. The results in Table 5.1 suggest that the 50 kDa dextran standard can be used as a non-interacting molecule with equivalent effective size to the antibody to evaluate the dead volume in the protein immobilized column.

Table 5.1 Retention volumes for the dextran standards and the monoclonal antibody determined from size-exclusion chromatography using the Superdex column.

Species	Retention Volume (mL)	Radius (nm)[a]
Dextran 33 kDa	13.6 ± 0.1	4.63
Dextran 42 kDa	12.9 ± 0.1	5.15
Dextran 50 kDa	12.5 ± 0.1	5.45
Dextran 62 kDa	12.0 ± 0.1	6.09
Dextran 80 kDa	11.4 ± 0.1	6.81
Monoclonal Antibody	12.6 ± 0.1	5.43

[a]Dextran radius estimated from the molecular weight using Equation (5.5).

Figure 5.1 shows typical chromatograms for the 50 kDa dextran and acetone. The running buffer for the dextran was a 50 mM phosphate buffer with 150 mM NaCl to minimize any electrostatic interactions associated with the charged antibody within the

resin pores. The measured retention volume for the dextran is 1.186 mL compared to 1.265 mL for the acetone in a protein immobilized column with 13% surface coverage. The acetone retention volume was independent of the buffer concentration. The dextran retention volume (1.186 mL) is in very good agreement with the value of V_o calculated from the cylindrical pore model (1.18 mL), providing further support for the use of the dextran as a non-interacting solute.

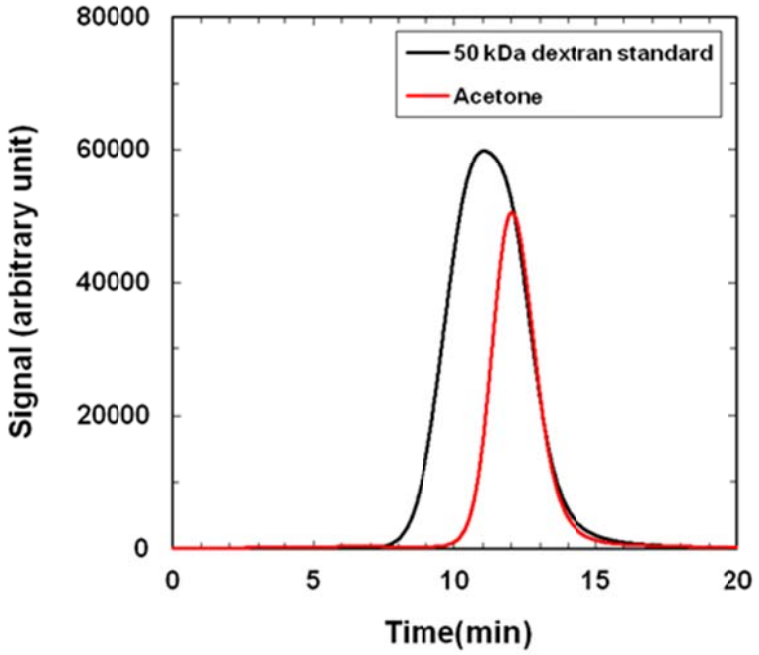

Figure 5.1. Comparison of acetone and the 50 kDa dextran elution peaks in the protein-immobilized column.

5.3.2 Second Virial Coefficients

The bottom panel of Figure 5.2 shows the measured retention volumes for the monoclonal antibody in a protein-immobilized column with 13% surface coverage at pH 5 for solutions prepared using a 5 mM acetate buffer with different amounts of added NaCl. These conditions are similar to that used for many monoclonal antibody formulations, with the intermolecular interactions dominated by repulsive interactions. The data are plotted as a function of solution ionic strength calculated based on the known amounts of acetate and NaCl (neglecting any contribution from the protein).

The protein retention volume was calculated from the location of the peak maximum due to the presence of significant peak tailing in some of the runs. This tailing is likely due to mass transfer limitations or non-specific interactions with the base matrix, as observed previously by Ahamed et al. [119] under similar conditions, and thus does not provide a measure of the magnitude of the protein-protein interactions in this system. Ahamed et al. [119] also used the peak maximum in their analysis of protein-protein interactions using SIC. In each case, data were obtained for three repeat measurements, with results reported as the mean retention volume. The data were highly reproducible, with standard deviations between repeat measurements of less than 0.02 mL (approximately 2%).

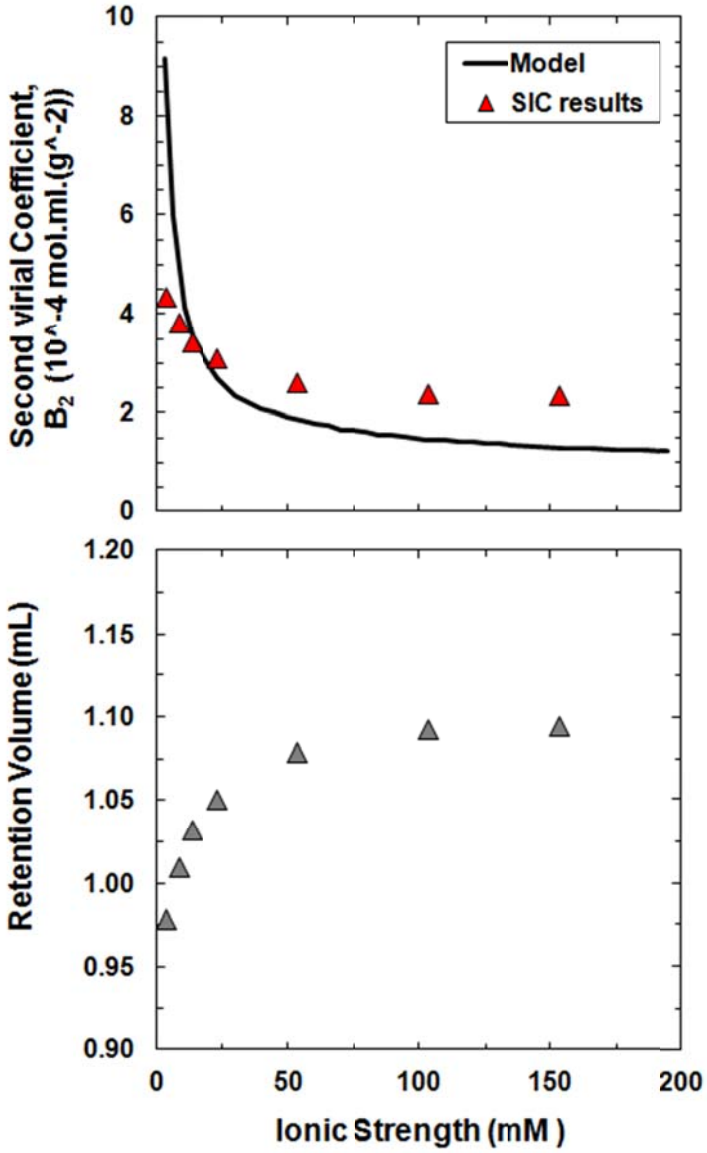

Figure 5.2. Retention volume (bottom panel) and second virial coefficient (upper panel) as a function of ionic strength for the monoclonal antibody in 5 mM acetate buffer at pH 5. The solid curve in the upper panel is a model calculation for the second virial coefficients developed using the potential of mean force for charge–charge electrostatic interactions between hard spheres.

The antibody retention volume increased from 0.979 to 1.095 mL as the ionic strength was increased from 3 mM to 153 mM. This increase in retention volume is

consistent with a reduction in electrostatic exclusion (repulsion) of the positively-charged antibody from the positively-charged pores of the antibody-immobilized column due to the increase in electrostatic shielding provided by the bulk electrolyte. The measured retention volumes appear to approach a constant value at high ionic strength, with $V_{protein}$ = 1.095 mL being slightly smaller than the dead volume determined from the 50 kDa dextran (V_o = 1.186 mL). This is discussed in more detail below.

The upper panel in Figure 5.2 shows the second virial coefficients calculated directly from Equation (5.1) using the retention coefficients given by Equation (5.2) and the measured retention volumes of the antibody and the 50 kDa dextran. The surface density of the immobilized antibody was evaluated from a simple mass balance on the protein solution used for the immobilization reaction giving 1.4×10^{15} molecule/m^2. The effective phase ratio was estimated from data for the pore size distribution of the Toyopearl AF Formyl 650M particles evaluated by DePhillips and Lenhoff [107] using inverse size-exclusion chromatography with a range of different molecular weight dextrans. Since the maximum possible immobilization density corresponds to a protein monolayer, all pores with $R >> 3r_s$ will be accessible to the antibody (corresponding to 7.4 m^2/mL). Tessier [101] assumed that an effective protein monolayer corresponded to approximately 30% surface coverage. Since the density of immobilized antibody in this work was only 13%, a significant fraction of smaller pores should also be accessible. This additional pore volume was estimated as 0.13/0.30 = 0.43 of the pores with radii between r_s and $3r_s$. This gives a total accessible area of ϕ = 10.9 m^2/mL. The protein excluded volume (B_{HS}) was estimated as [102] (equivalent to Equation 4.7):

$$B_{HS} = \frac{16}{3}\left(\frac{\pi r_s^3 N_{Av}}{M_p^2}\right) \tag{5.6}$$

where N_{AV} is Avogadro's number and M_p is the antibody molecular weight. The protein radius was taken as r_s = 5.43 nm independent of ionic strength based on the SEC data in Table 5.1.

The second virial coefficient decreases with increasing solution ionic strength, consistent with the increase in electrostatic shielding of the intermolecular repulsive interactions between the positively-charged antibody molecules. The values at high ionic strength become nearly constant with $B_2 \approx 2.4\times10^{-4}$ mL mol/g^2. Note that the calculated value of B_2 using the dead volume determined from the acetone peak in the "dead column" was slightly negative under these conditions, in contrast to the positive values reported in the literature [110].

The solid curve in the top panel of Figure 5.2 is a model calculation developed using the potential of mean force for charge–charge electrostatic interactions between hard spheres (Equation 4.6). The protein charge was evaluated as a function of solution ionic strength from the measured electrophoretic mobility determined from electrophoretic light scattering data obtained with a Malvern Zetasizer Nano (Worcestershire, UK) as described in Chapter 4. Values of Z at select conditions are summarized in Table 4.1. The model is in good qualitative agreement with the data, although it does tend to over-predict B_2 at very low ionic strength with the reverse behavior seen at high ionic strength.

The discrepancy at high ionic strength is likely due in part to errors in the evaluation of the excluded volume contribution to the virial coefficient. For example,

Vilker et al. [31] showed that the excluded volume term for a prolate ellipsoid with aspect ratio of 3.2 was 42% larger than that for a hard sphere with equivalent volume. The use of Equation (5.6) also ignores the possible contribution from a hydration layer around the protein [127] or to some type of weak intermolecular repulsive interaction. The discrepancies at low ionic strength could be due to the breakdown of the Debye–Huckel approximation (assumption of low surface potential in the development leading to Equation 5.8) in combination with errors associated with the complete exclusion of the antibody from the smaller pores of the SIC resin under these conditions. This is discussed in more detail below.

To further study the accuracy of this approach, the second virial coefficients evaluated from SIC were compared with results from membrane osmometry for the same monoclonal antibody at the same buffer conditions (from Chapter 4). The osmometry experiments required more than 1 g of protein at each solution condition, compared to the several mg needed for the SIC measurements. The results are summarized in Table 4.1 along with the model calculations given by Equations (5.6) to (5.8). The second column gives the ionic strength calculated based on the known amounts of acetate and NaCl. The B_2 values determined by SIC at pH 6 and 7, and at pH 5 and relatively high ionic strength, are in good agreement with results from membrane osmometry. However, the values at pH 5 and low ionic strength ($\leq$ 20 mM) show considerable discrepancies, with the values determined from SIC being considerably smaller than the values determined from the osmotic pressure measurements. One possible explanation for this discrepancy is the non-random immobilization of the antibody as discussed by Rakel et al. [125]. Alternatively, the antibody may be totally excluded from the smaller highly charged

pores in the protein-immobilized resin particles at low ionic strength, an effect that is likely to be more pronounced for the large antibody molecule examined in this work compared to previous SIC studies using small proteins like lysozyme and α-chymotrypsinogen. The data in Table 4.1 are also in good agreement with the value of B_2 = 1.7×10^{-4} mL mol/g^2 at pH 7 and 30 mM ionic strength reported by Le Brun et al. [110] for a different antibody.

5.4 Conclusion

Self-interaction chromatography is an attractive high throughput method for studying protein–protein interactions in different buffer conditions. The results presented in this chapter demonstrate that it is possible to use a dextran standard with equivalent hydrodynamic volume to evaluate the dead volume in the protein immobilized column to evaluate the second virial coefficient. This not only eliminates the need for a second (dead) column, reducing the time and increasing the throughput for the SIC measurements, the dextran also appears to provide a more accurate estimate of the dead volume since it eliminates errors associated with differences in column packing and the estimation of the immobilized protein volume. These effects are likely to be more important for larger proteins like the monoclonal antibody examined in this work.

The calculated values of the second virial coefficient were in good agreement with independent measurements of B_2 based on osmotic pressure data, providing additional validation of this approach. The greatest discrepancies are seen at low ionic strength and low pH, conditions where there are strong repulsive electrostatic interactions

that will likely cause the complete exclusion of the highly charged protein from the smaller pores within the protein-immobilized resin. This effect has not been discussed in most previous studies of SIC, many of which were targeted at identifying appropriate conditions for protein crystallization (i.e., conditions where B_2 is slightly negative). In contrast, most downstream processing and protein formulations employ buffer conditions where the overall intermolecular interaction is repulsive ($B_2 > 0$). The results obtained in this study clearly demonstrate the potential of using SIC to evaluate the magnitude of the intermolecular interactions under these conditions even for large proteins like monoclonal antibodies.

Chapter 6

Viscosity of Highly Concentrated Monoclonal Antibody Solutions

Note: Most of material presented in this chapter has been submitted for publication in: E. Binabaji, J. Ma, A.L. Zydney, Intermolecular Interactions and the Viscosity of Highly Concentrated Monoclonal Antibody Solutions, Pharmaceutical Research.

6.1 Introduction

Monoclonal antibodies are typically delivered in very highly concentrated solutions to achieve the desired dosage (mg antibody per kg patient body weight) in the limited volumes that can be delivered by subcutaneous injection [15]. The high viscosity of these solutions can have a significant impact on both the delivery and purification of the monoclonal antibody product [15]. There have thus been a number of prior studies focused on understanding the key factors controlling the viscosity of highly concentrated solutions of different monoclonal antibodies.

Liu et al. [128] investigated the effects of salt concentration and solution pH on the viscosity of a humanized IgG1 monoclonal antibody using both capillary and cone-and-plate rheometers. The viscosity of a dilute (10 g/L) solution behaved like a

Newtonian fluid over shear rates between 0.1 and 10,000 s^{-1}, but data with a 200 g/L solution in a 25 mM histidine buffer at pH 6 with 435 mM sucrose showed significant shear-thinning behavior over the entire range of shear rates. The viscosity of a 125 g/L solution in a 16 mM histidine buffer with 266 mM sucrose decreased by more than a factor of 8 as the NaCl concentration was increased from 0 to 200 mM due to the shielding of repulsive electrostatic intermolecular interactions. The viscosity in the absence of NaCl (in the presence of acetate or arginine) showed a sharp maximum around pH 5.8, which was well below the protein isoelectric point. The authors attributed this behavior to the presence of attractive electrostatic interactions leading to reversible self-association; this behavior was not seen with other monoclonal antibodies having very similar structure.

Chari et al. [129] examined the viscosity of an IgG_2 antibody using high frequency rheology. In contrast to the results obtained by Liu et al. [128], the viscosity reached its maximum value around the protein isoelectric point (pH 9). Model calculations indicated that the rheological behavior was dominated by long-range repulsive interactions at low protein concentrations but that short range attractive interactions (e.g., dipole–dipole attraction) became important at high protein concentrations.

Saito et al. [35] obtained data for the viscosity of three humanized IgG_1 monoclonal antibodies over a range of pH using a microfluidic Rheosense viscometer. The viscosity of two antibodies increased monotonically with increasing solution pH (from pH 5 to 8 in a 10 mM acetate or phosphate buffer with 140 mM NaCl), while the viscosity for the third antibody showed a significant decrease with increasing pH. The

viscosity data for all three antibodies were well correlated with independent measurements of the second virial coefficient (B_2). However, the reduction in viscosity with increasing values of B_2 is exactly opposite of that predicted using available theories for the viscosity of concentrated colloidal dispersions [130], all of which predict that an increase in repulsive interactions (as described by the second virial coefficient) should lead to an increase in the effective size of the colloidal particles and thus an increase in viscosity. Sarangapani et al. [131] discussed the limitations of colloidal descriptions of the viscosity of concentrated protein solutions in the context of the behavior of bovine serum albumin, specifically highlighting the effects of surface hydration, surface charge distribution, and conformational changes.

Yadav et al. [132] examined the effects of charge distribution on the viscosity of a series of monoclonal antibody variants with different surface charge in a histidine buffer at pH 6.0. Antibodies with more non-uniform surface charge had higher viscosity, which the authors attributed to the increased intermolecular attraction between oppositely charged "patches" on different antibodies. The results were analyzed in terms of the second virial coefficient (determined from light scattering measurements), although there was no direct correlation between these parameters. The authors explained the behavior qualitatively in terms of the different effects of intermolecular interactions on self-association and irreversible aggregation, both of which affect the solution viscosity.

Despite the previous work in this area, there are still considerable uncertainties over the key factors controlling the viscosity of highly concentration solutions of monoclonal antibodies. The objective of the work presented in this chapter was to examine the viscosity of highly concentrated solutions of an IgG1 antibody over a wide

range of protein concentrations, solution pH, salt concentrations, and the presence / absence of different excipients. The viscosity results were analyzed in terms of the antibody virial coefficients (both B_2 and B_3 as evaluated from osmotic pressure data) to obtain additional insights into the effects of intermolecular protein-protein interactions on the behavior of these highly concentrated antibody solutions.

6.2 Materials and Methods

All experiments were performed using a highly purified IgG_1 monoclonal antibody provided by Amgen with molecular weight of 142 kDa and isoelectric point of 8.16. Data were obtained in acetate and phosphate buffers, both with and without added sucrose (Sigma, S-2395), L-proline (SPECTRUM, P1434), or arginine-HCl (JT Baker, 2067-06) as excipients. Protein solutions were kept at 4°C for up to a week; solutions used for longer periods of time were kept at -30°C. More details on sample preparation were presented in Chapter 3.

The steady-state viscosity (ratio of shear stress to shear rate) was evaluated using a Rheometrics Fluids Spectrometer (RFS II, strain-controlled rotational rheometer) with a concentric cylinder geometry having an inner diameter of 1.65 cm, an outer diameter of 1.71 cm, and height of 1.37 cm. The RFSII has two transducers with different torque sensitivity that provide reliable viscosity measurements from about 1 mPa.s to more than 100 mPa.s.

The rheometer was initially calibrated using a series of Newtonian standards (oils and water) of known viscosity. The sample temperature was maintained at 25 ± 1 °C

using a circulating water bath surrounding the outer cylinder; the temperature was monitored using a thermocouple connected to the inner cylinder. The sample holder and inner cylinder were thoroughly washed with deionized water and completely dried prior to each experiment. 1 mL of the antibody solution was carefully loaded into the sample holder, taking extra care to avoid any bubble formation. The shear stress was then measured over a range of shear rates from 10–1000 s^{-1} with two data points typically taken per decade. Most experiments were performed with continually increasing shear rate; limited data were obtained with decreasing shear rate to verify that there was no hysteresis or shear-induced changes to the protein.

The antibody concentration for each sample was measured using the UV absorbance at 280 nm determined using a NanoDrop spectrophotometer both before and after each experiment. Measurements were typically within 1 percent, with the largest absolute deviation being 4–5 g/L at the highest protein concentrations (>200 g/L). In addition, size exclusion chromatography with a Superdex 200 column was performed on select samples to evaluate the fraction of antibody dimers and higher order oligomers. In most cases, the dimer peak was undetectable, and there was no evidence of any higher order oligomers in any of the samples.

6.3 Results and Analysis

6.3.1 Monoclonal Antibody Viscosity

Typical data for the viscosity (η) of the monoclonal antibody solution in a pH 5 acetate buffer with 20 mM NaCl at different antibody concentrations are shown in Figure

6.1. In each case, the viscosity was essentially independent of the shear rate over the range from 10 to 1000 s^{-1}, indicating that the antibody solution was Newtonian over this range of conditions. This behavior is consistent with recent data by Castellanos et al. [133], who attributed the non-Newtonian behavior seen in other studies using rotational rheometers to the effects of the air-liquid interface at the top of the cylinder. There was a small decrease in viscosity with increasing shear rate for the 219 g/L solution, which may reflect some shear-thinning behavior for this sample. The viscosity increases significantly with increasing antibody concentration, going from around 6 mPa.s at an antibody concentration of 140 g/L to 80 mPa.s at 270 g/L.

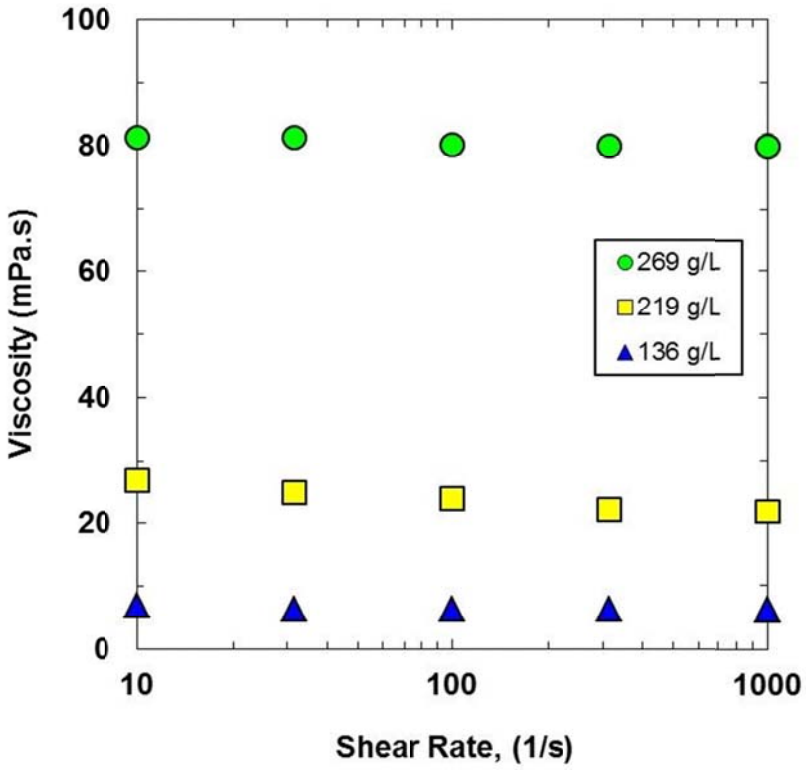

Figure 6.1. Viscosity (η) as a function of shear rate for the IgG_1 monoclonal antibody in a 5 mM acetate buffer at pH 5 with 20 mM NaCl.

The RFS II rheometer used in this work has a cylinder length of 1 cm; thus, the air-liquid interface would not be expected to cause a significant perturbation in the measured (average) shear stress at the relatively high shear rates examined in this work. In addition, limited experiments were performed in the presence of 10% Triton X-100, a non-ionic surfactant that has been used previously to minimize interfacial viscosity. The measured viscosity in the presence of the Triton X-100 was within 10% of that for the pure antibody solution under otherwise identical conditions, indicating that the results obtained with the RFS II rheometer reflect the true bulk viscosity of the antibody solution. There was also no evidence of any hysteresis; data obtained with increasing and decreasing shear rate (as shown in Figure 6.2) were indistinguishable. The data in Figure 6.2 do show a small but statistically significant reduction in viscosity with increasing shear rate, consistent with the presence of some shear-thinning in the antibody solution possibly due to the break-up of solute aggregates with increasing shear rate.

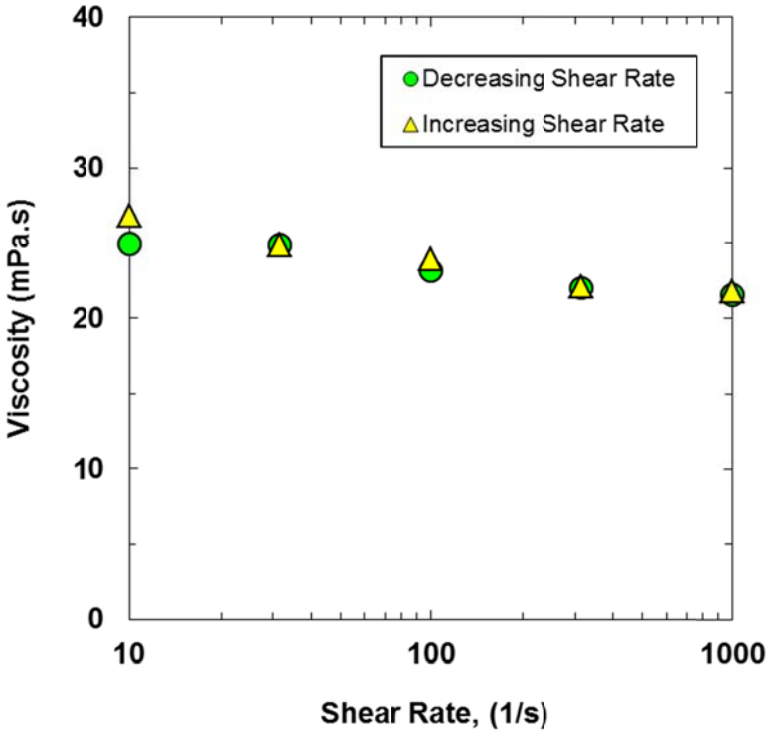

Figure 6.2. Viscosity (η) as a function of shear rate for the IgG_1 monoclonal antibody in a 5 mM acetate buffer at pH 5 with 20 mM NaCl at 219 g/L. Measurements obtained with decreasing shear rate is compared with the viscosity measurements obtained with increasing shear rate.

The effect of the antibody concentration on the relative viscosity, η/η_0 where η_0 is the viscosity of the protein-free buffer, is examined in Figure 6.3. The data at pH 5 were obtained in a 5 mM acetate buffer while a 5 mM phosphate buffer was used for the results at pH 6 and 7, both with 20 mM NaCl. The solid and dashed curves are model fits as described in Section 6.3.2. The viscosity at any given antibody concentration increases with increasing pH, particularly at high protein concentrations. This effect was quite significant, with the viscosity at pH 7 being nearly double that at pH 5.

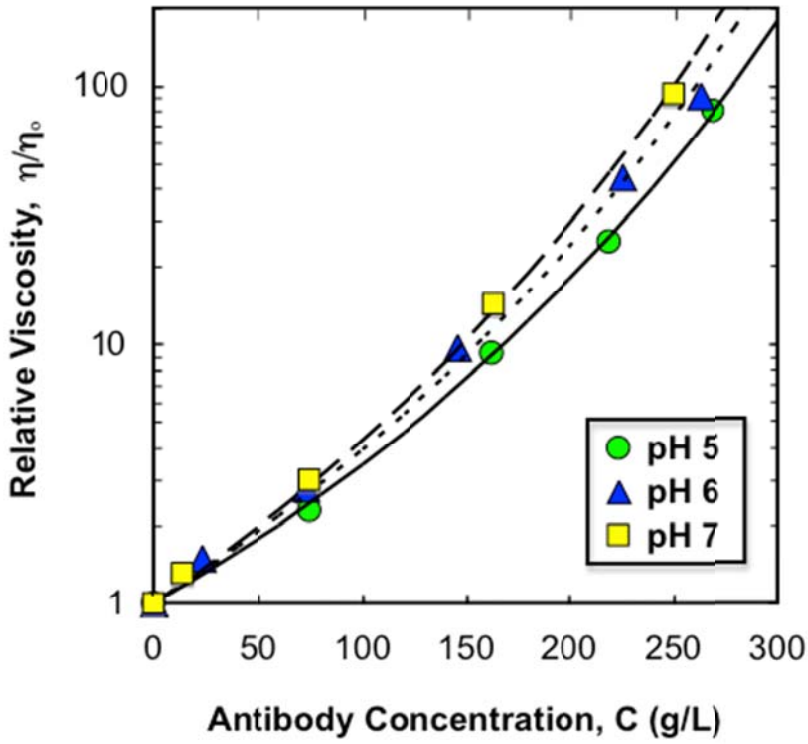

Figure 6.3. Relative viscosity at high shear rate as a function of the antibody concentration at several pH values. Data at pH 5 were in an acetate buffer while for pH 6 and 7 a phosphate buffer was used, all with 20 mM NaCl. Solid and dashed curves are model calculations using Equation (6.3) with the best fit values of b and C_{max} = 800 g/L.

Figure 6.4 shows the effect of solution ionic strength, adjusted by the addition of NaCl, on the antibody viscosity in a 5 mM acetate buffer at pH 5. The relative viscosity increases with increasing NaCl concentration at all three concentrations, suggesting that the shielding of the electrostatic interactions causes the observed increase in viscosity.

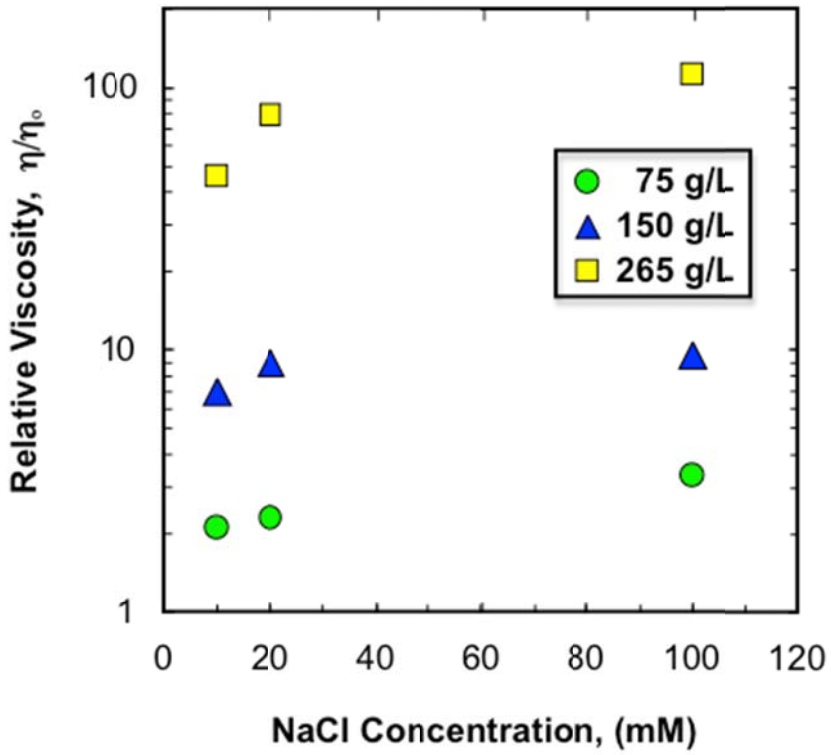

Figure 6.4. Relative viscosity of the antibody solution at high shear rate as a function of added NaCl concentration for experiments performed using a 5 mM acetate buffer at pH 5.

The behavior seen in Figures 6.3 and 6.4 is exactly opposite to that predicted by classical models for the rheology of colloidal dispersions [130]:

$$\frac{\eta}{\eta_0} = 1 + 2.5\varphi + \left[2.5 + \frac{3}{40}\left(\frac{d_{eff}}{2r_s} \right)^5 \right] \varphi^2 + O\left(\varphi^3\right) \tag{6.1}$$

where φ is the protein volume fraction (proportional to the protein concentration), r_s is the protein radius (treated as a sphere), and d_{eff} is the effective diameter of the protein accounting for a square well repulsive potential. Detailed expressions for the highest order term (e.g., of order φ^3) for charged spheres are not currently available. d_{eff} is

expected to decrease with increasing pH due to the reduction in net charge of the monoclonal antibody, which varies from $Z = 14$ at pH 5 to $Z = 6$ at pH 6 and $Z = 3$ at pH 7 (as determined from the measured values of the electrophoretic mobility as discussed in Chapter 4). d_{eff} is also expected to decrease with increasing ionic strength due to the reduction in the thickness of the electrical double layer. These phenomena are discussed in more detail in Section 6.3.3.

6.3.2 Model Correlations

A number of different theoretical models and empirical correlations have been used in the literature to describe the behavior of concentrated protein solutions. Connolly et al. [134] used a simple exponential model to describe the viscosity for a range of monoclonal antibodies:

$$\frac{\eta}{\eta_0} = \exp(mC) \tag{6.2}$$

where m is an empirical coefficient. Although Equation (6.2) is qualitatively consistent with the data in Figure 6.3, the results at high protein concentrations show significant upward curvature on the semi-log plot. More accurate fits to the data were developed using the semi-empirical model originally presented by Ross and Minton [135] for the viscosity of concentrated hemoglobin solutions:

$$\frac{\eta}{\eta_0} = \exp\left[\frac{bC}{1-\left(\frac{C}{C_{\max}}\right)}\right] \tag{6.3}$$

where b is related to the intrinsic viscosity and C_{max} provides a measure of crowding and steric constraints in the highly concentrated protein solutions. In order to verify the appropriateness of Equation (6.3) for describing the viscosity results obtained with the monoclonal antibody solutions, the data in Figure 6.3 were re-plotted in Figure 6.5 in a linearized form as:

$$\frac{1}{\ln\left(\frac{\eta}{\eta_0}\right)} = \left(\frac{1}{b}\right)\frac{1}{C} - \frac{1}{bC_{\max}} \tag{6.4}$$

The data at pH 5 are highly linear when plotted in this fashion, with $r^2 > 0.99$, with the best fit values of the slope and intercept giving $b = 0.0108 \pm 0.001$ L/g and $C_{max} = 640 \pm 90$ g/L.

The viscosity data were all analyzed using Equation (6.3) with the best fit values of the model parameters determined by non-linear regression using Mathematica Version 9.0. The high degree of coupling between b and C_{max} made it difficult to accurately determine both of these parameters from the available data, leading to very high error bars (95% confidence intervals). However, all of the fitted values of C_{max} were similar, with no clear dependence on solution pH or ionic strength. Thus, the data were re-fit using the average value of $C_{max} = 800$ g/L as determined from multiple data sets, with the best fit values of the parameter b then determined for each set of experimental conditions by non-linear regression. The solid and dashed curves in Figure 6.3 are the resulting model calculations with $b = 0.0108$, 0.0119, and 0.0126 L/g for pH 5, 6, and 7, respectively. The model fits are in very good agreement with the experimental data over the full range of antibody concentrations, providing further support for the use of

Equation 6.3 to analyze the viscosity of these highly concentrated monoclonal antibody solutions.

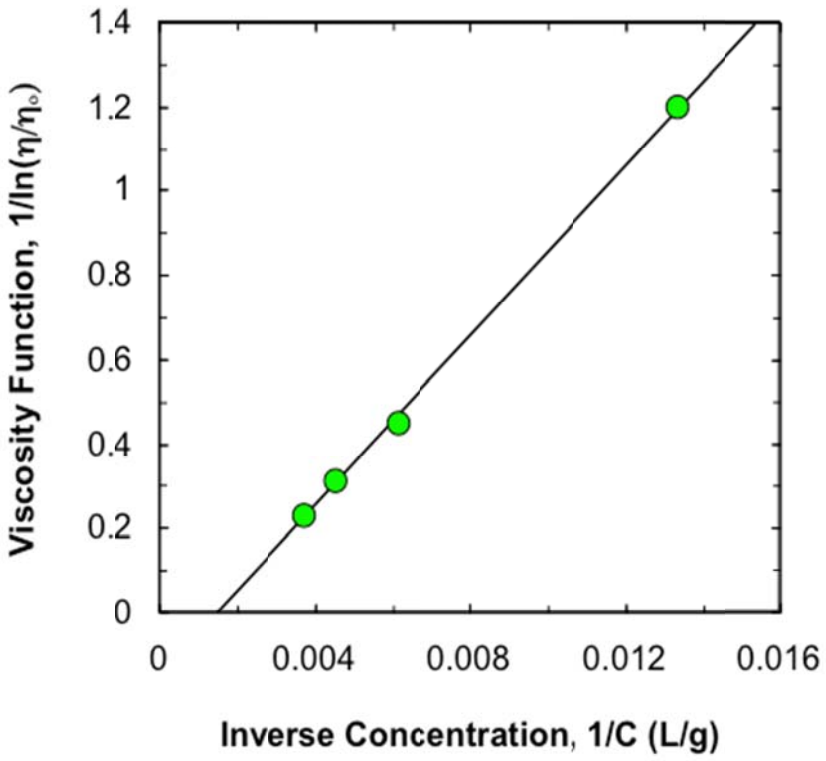

Figure 6.5. Linearized plot of the viscosity data in a 5 mM acetate buffer with 20 mM added NaCl at pH 5. Solid line is linear regression fit using Equation (6.4).

6.3.3 Virial Coefficients

The best fit values of the viscosity parameter *b* for the different buffer conditions are summarized in Table 6.1 along with results for the second and third virial coefficients determined for the same monoclonal antibody in the same buffers from the osmotic pressure data in Chapter 4. The viscosity parameter b increases with increasing pH and

salt concentration, while the second virial coefficient decreases over the same range of parameters. This relationship between the viscosity and the second virial coefficient for monoclonal antibody solutions has been reported previously by Saito et al. [35] and Connolly et al. [134]. However, the inverse correlation seen in Table 6.1, and in the studies by Saito et al. and Connolly et al., is inconsistent with theoretical descriptions of colloidal systems which show that a repulsive inter-particle potential produces a stress that causes a corresponding increase in the solution viscosity and the second virial coefficient through its effect on the potential of mean force.

The importance of reversible self-association on the behavior of highly concentrated solutions of monoclonal antibodies has been reported in a number of previous studies [35, 128, 129]. These associations are due to local (short-range) attractive interactions that appear to dominate in very highly concentrated solutions despite the presence of long-range electrostatic repulsion caused by overall net positive charge of the antibody. The importance of these local attractive interactions on the osmotic pressure was discussed in Chapter 4; this results in significant negative values of the third virial coefficients (B_3) as seen in Table 6.1. These local interactions are likely electrostatic in origin, e.g., those associated with dipole–dipole attraction, as indicated by the significant decrease in the absolute value of B_3 with increasing ionic strength.

The results in Table 6.1 show a direct correlation between b and B_3, with both parameters increasing with increasing pH and salt concentration. In addition, the b value in the pH 5, 100 mM NaCl solution lies between the values in the pH 6 and pH 7 solutions (both with 20 mM NaCl), which is consistent with the very similar values of the third virial coefficient in these buffers.

Table 6.1 Effect of buffer conditions on the viscosity coefficient (b), the second and third osmotic virial coefficients (B_2 and B_3), and the antibody charge (Z).

Buffer Condition	b $\left(\frac{\mathbf{m^3}}{\mathbf{kg}}\right) \times \mathbf{10^2}$	B_2 $\left(\frac{\mathbf{mL.mol}}{\mathbf{g^2}}\right) \times \mathbf{10^4}$	B_3 $\left(\frac{\mathbf{mL^2.mol}}{\mathbf{g^3}}\right) \times \mathbf{10^7}$	Z
pH 5				
10 mM	0.962	7.1 ± 1.3	-19 ± 7	12 ± 1
20 mM	1.08	4.4 ± 0.4	-11 ± 2	14 ± 1
100 mM	1.23	2.5 ± 0.4	-4 ± 2	24 ± 1
20 mM NaCl				
pH 5	1.08	4.4 ± 0.4	-11 ± 2	14 ± 1
pH 6	1.19	2.6 ± 0.3	-4 ± 2	6 ± 1
pH 7	1.26	1.7 ± 0.1	-3 ± 1	3 ± 1

* Error limits on B_2 and B_3 were determined using Mathematica (for the osmotic pressure data) or by propagation of error analysis (for Z values).

The relationship between b and B_3 is examined more explicitly in Figure 6.6 for experiments performed over a range of solution pH and NaCl concentration. The results are highly linear with $r^2 = 0.97$, suggesting that an increase in attractive intermolecular electrostatic interactions (more negative values of the third virial coefficient) leads to a reduction in the viscosity of the antibody solution (smaller value of the viscosity parameter). The local attractive interactions can be thought of as reducing the effective diameter of an individual antibody (d_{eff} in Equation 6.1) or as reducing the effective volume fraction of the suspension (by creating small "compact" aggregates of several antibodies), in either case leading to a reduction in the solution viscosity.

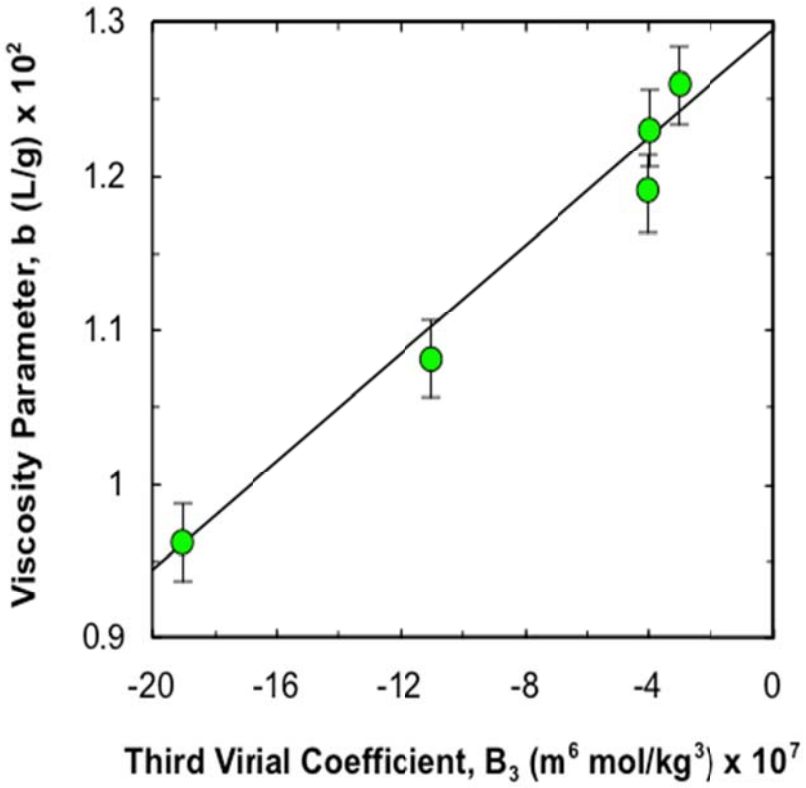

Figure 6.6. Relationship between the viscosity coefficient (*b*) and the third virial coefficient (B_3) for monoclonal antibody solutions over a range of pH and salt concentration (data in Table 6.1). Error bars were calculated from the 95% confidence interval on *b* determined using Mathematica.

6.3.4 Effect of Excipients

A number of different excipients are used to stabilize highly concentrated formulations of monoclonal antibodies and to help prevent protein aggregation. Viscosity data were obtained in the presence of three commonly used excipients: sucrose, L-proline, and arginine-HCl. The effects of arginine-HCl on the viscosity of the antibody solution in a pH 5, 5 mM acetate buffer with 20 mM NaCl are shown in Figure 6.7. At low protein concentrations, the viscosity increases slightly with increasing arginine

concentration due to the known effect of arginine on the viscosity of water (in the absence of protein). In contrast, arginine caused a reduction in viscosity at high antibody concentrations (above about 150 g/L). This effect is quite pronounced at the highest protein concentration (≈ 270 g/L), with the viscosity decreasing from 80 mPa.s in the absence of arginine to 40 mPa.s in the presence of 300 mM arginine.

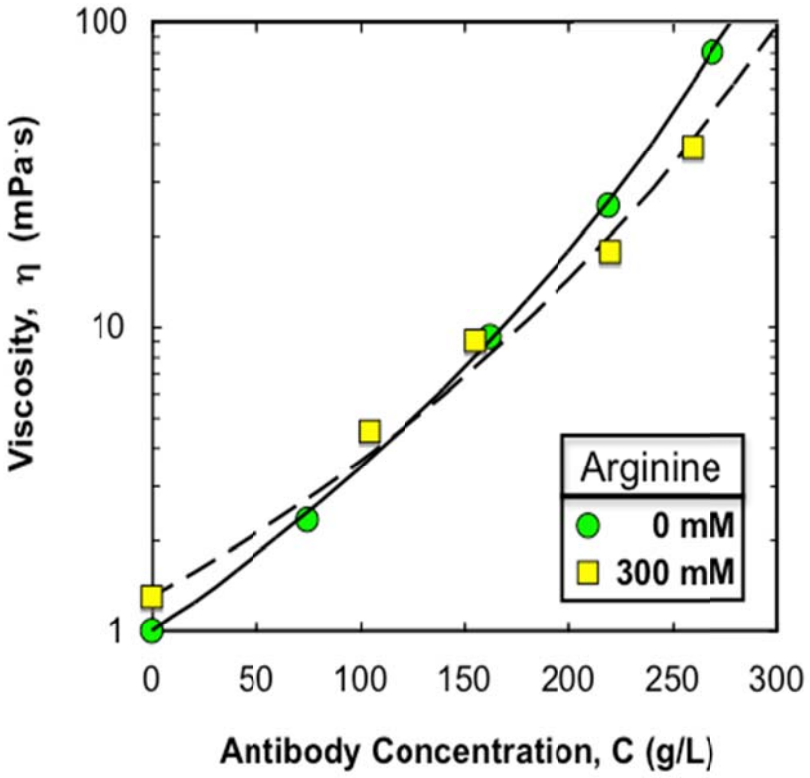

Figure 6.7. Viscosity as a function of antibody concentration in a 5 mM acetate buffer at pH 5 with 20 mM NaCl both with and without added arginine. Solid and dashed curves are model calculations based on Equation (6.3) with C_{max} = 800 g/L with b = 0.0108 L/g in the absence of arginine and b = 0.0090 L/g in the presence of 300 mM arginine.

The solid and dashed curves in Figure 6.7 are the model fits using Equation (6.3). The model is in very good agreement with the experimental results using b = 0.0108 L/g in the absence of arginine and b = 0.0090 L/g in the presence of 300 mM arginine. The addition of arginine also caused a small decrease in the value of the second virial coefficient from $B_2 = 4.4\times10^{-4}$ $m^3.mol/kg^2$ in the absence of arginine to $B_2 = 3.5\times10^{-4}$ $m^3.mol/kg^2$ in the 300 mM arginine solution (see Chapter 4). Arginine had a larger effect on the third virial coefficient, with B_3 going from -11×10^{-7} $m^6.mol/kg^3$ in the absence of arginine to -9×10^{-7} $m^6.mol/kg^3$ in the 300 mM arginine solution, corresponding to a reduction in the magnitude of the attractive multi-body interactions. This behavior is consistent with previous work by Arakawa et al. [136] who concluded that arginine reduces the extent of protein aggregation by suppressing short range protein–protein interactions through its association with the amino acid side chains and peptide bonds. Arginine also alters the structure of water, as seen in changes in the surface tension [136] as well as the solution viscosity [137].

The origin of the reduction in the viscosity coefficient b with added arginine is unclear; the data in Figure 6.5 indicate that increasing the value of B_3 (i.e., reducing the magnitude of the negative value) would cause an increase in the value of b. Additional experiments were thus performed using the same buffer (5 mM acetate with 20 mM NaCl at pH 5) with 300 mM concentrations of the excipients L-proline and sucrose. In each case, the addition of the excipient caused an increase in the viscosity of water, which led to a small increase in the viscosity of the antibody solution at low protein concentrations. However, the excipients significantly reduced the increase in viscosity with increasing protein concentration, with the net result that the viscosity at high protein concentrations

was lower than that for the solution without any excipient (similar to the results for arginine in Figure 6.7).

The best fit values of the viscosity coefficient and the osmotic virial coefficients for the 300 mM solutions of the different excipients are summarized in Table 6.2. All three excipients caused a reduction in the viscosity coefficient as well as a corresponding increase in the third virial coefficient; the effect of the excipient on the second virial coefficient was small.

Table 6.2 Effect of excipients (300 mM concentration) on the viscosity coefficient (b), viscosity at infinite dilution (η_0), and the second and third osmotic virial coefficients (B_2 and B_3) in a 5 mM acetate buffer at pH 5 with 20 mM added NaCl

Excipient Condition	b $\left(\frac{\mathbf{m^3}}{\mathbf{kg}}\right) \times \mathbf{10^2}$	η_0 $(\mathbf{Pa.s}) \times \mathbf{10^3}$	B_2 $\left(\frac{\mathbf{mL.mol}}{\mathbf{g^2}}\right) \times \mathbf{10^4}$	B_3 $\left(\frac{\mathbf{mL^2.mol}}{\mathbf{g^3}}\right) \times \mathbf{10^7}$
None	1.08	1.00	4.4 ± 0.4	-11 ± 2
Arginine-HCl	0.90	1.30	3.5 ± 0.1	- 9 ± 2
L-Proline	0.84	1.39	4.1 ± 0.1	- 10 ± 2
Sucrose	0.89	1.41	4.0 ± 0.4	- 9 ± 2

* Error limits on B_2 and B_3 were determined using Mathematica based on the osmotic pressure data.

6.4 Discussion

The data obtained in this chapter provide an extensive study of the viscosity of a highly purified monoclonal antibody, focusing on the behavior at very high protein

concentrations and including a range of solution pH, salt concentration, and the presence of several commonly used excipients. The viscosity of the antibody solution was essentially independent of the shear rate over the range from 10–1000 s^{-1} even in highly concentrated solutions (up to 260 g/L), although there was some evidence of weak shear-thinning behavior in some of the protein solutions. The viscosity at very high antibody concentrations (>250 g/L) was greater than 100 mPa.s at some buffer conditions. The viscosity increased with increasing pH (over the range from pH 5 to 7) and it also increased with increasing salt concentration (at pH 5).

The viscosity data were analyzed using the semi-empirical model developed by Ross and Minton [135], providing a simple correlation for the concentration-dependence of the viscosity. The viscosity coefficient *b* was well-correlated with data for the third virial coefficient for the same antibody determined under identical buffer conditions. Note that Saito et al. [35] and Connolly et al. [134] both suggested a correlation between the viscosity and second osmotic virial coefficient based on data for a series of monoclonal antibodies (with the virial coefficients evaluated indirectly from sedimentation data). However, the inverse correlation seen in both of those studies is inconsistent with available models for the viscosity of colloidal dispersions. In addition, there is extensive previous work indicating that the viscosity of highly concentrated antibody solutions is governed primarily by short-range attractive interactions, which cannot be described by the positive values of the second virial coefficient. In contrast, the values for the third virial coefficient were negative over all experimental conditions, corresponding to short-range multi-body attractive interactions. The relationship between

the viscosity behavior and the third virial coefficient has not been recognized previously, in large part due to the nearly complete absence of data for the third virial coefficient.

The results reported in this chapter may also help explain the very different behavior observed for monoclonal antibodies and other model proteins like bovine serum albumin (BSA). For example, Heinen et al. [138] found a reduction in the viscosity of concentrated BSA solutions with increasing salt concentration, exactly the opposite of the behavior seen in this chapter and elsewhere for monoclonal antibodies, even though the second osmotic virial coefficients are similar in magnitude for both proteins. However, the third virial coefficients for BSA are positive [31], in contrast to the negative values of the third virial coefficient for the monoclonal antibody examined in this thesis. It is not possible to extend this analysis to other proteins due to the lack of available data on the viscosity and third virial coefficients under comparable buffer conditions.

The addition of the excipients, such as proline, arginine, and sucrose, caused an increase in the viscosity at low antibody concentrations where the viscosity is dominated by that of the solvent. The behavior is very different at high antibody concentrations where the excipients caused a significant reduction in the viscosity. For example, the addition of 300 mM arginine caused a two-fold reduction in the viscosity. This effect could not be explained by the change in the osmotic virial coefficients since the observed increase in B_3 was expected to cause an increase in viscosity due to the reduction in the magnitude of the short range attractive multi-body interactions. Additional experimental studies will be needed to clarify the origin of the complex behavior associated with these excipients.

Chapter 7

Theoretical Analysis of the Ultrafiltration Behavior of Highly Concentrated Protein Solutions

Note: Most of material presented in this chapter has been submitted for publication in: E. Binabaji, J. Ma, S. Rao, A.L. Zydney, Theoretical analysis of the ultrafiltration behavior of highly concentrated protein solutions, Journal of Membrane Science.

7.1 Introduction

Ultrafiltration is the most commonly used method for concentration and final formulation of recombinant therapeutic proteins, most of which are delivered by injection [15, 18, 19]. Ultrafiltration of highly active hormones (e.g., insulin), cytokines (e.g., interferon), and clotting factors (e.g., Factor VIII) is relatively straightforward since these proteins are delivered at low to moderate concentrations. In contrast, monoclonal antibodies need to be formulated in highly concentrated solutions (up to and exceeding 200 g/L) to achieve the desired dosage in the limited volumes that can be delivered by subcutaneous injection, creating significant challenges for ultrafiltration [15, 18, 19].

As mentioned in Chapter 2 most theoretical descriptions of the filtrate flux in ultrafiltration systems are developed using a “stagnant film” model based on solution of the

steady-state one-dimensional convection-diffusion equation (Equation 2.10) which can be integrated across the concentration boundary layer (with thickness δ) assuming that the protein diffusion coefficient (*D*) is constant to give the classical concentration polarization model for a fully retentive membrane [139]:

$$J_v = k \ln\left[\frac{C_w}{C_b}\right] \tag{7.1}$$

A variety of expressions are available for the mass transfer coefficient in different modules [33], with these correlations developed from experimental data (obtained from both mass and heat transfer experiments) and from solution of the appropriate convection-diffusion equation in a particular flow system (e.g., laminar flow over a flat plate).

Although, Equation (7.1) provides an accurate description of the filtrate flux for low to moderate protein concentrations, this simple polarization model cannot be used with highly concentrated solutions due to the assumptions of a constant diffusion coefficient / viscosity and the neglect of protein-protein interactions within the concentration polarization boundary layer. A number of different approaches have been proposed to address the limitations of the classical stagnant film model. For example, Aimar and Field [61] accounted for the effects of the high viscosity of the concentrated solution near the membrane surface by multiplying the mass transfer coefficient in Equation (7.1) by the empirical correction factor $(\eta_b / \eta_w)^{0.27}$ where η_b and η_w are the viscosities evaluated using the bulk and wall concentrations, respectively. Gekas and Hallstrom [62] used a similar approach but with a correction factor based on the Schmidt number, $(Sc_b / Sc_w)^{0.11}$ where $Sc_w = \frac{\eta_w}{\rho D_w}$ to account for the dependence of both the solution viscosity and diffusion

coefficient on the protein concentration. Kozinski and Lightfoot [50] argued that the product of the diffusion coefficient and viscosity was constant based on the Stokes-Einstein equation, and that this was the key parameter governing mass transfer in a rotating disk ultrafiltration module. Zydney [63] took a very different approach by incorporating the concentration dependence of the diffusion coefficient directly in Equation (2.10), both through the protein mobility and the use of the gradient in the chemical potential (instead of the gradient in the protein concentration) for the driving force for diffusion. No attempt was made to account for the concentration dependence of the viscosity. Model calculations were in good agreement with experimental data obtained in a stirred ultrafiltration device. This approach is discussed in more detail in the next section.

The objective of this work was to develop a more accurate model for the filtrate flux in the ultrafiltration of highly concentrated protein solutions that properly accounts for: (1) the effects of intermolecular interactions on the thermodynamic driving force for diffusion, (2) the concentration dependence of the solution viscosity, and (3) the large parasitic pressure losses due to flow through the tangential flow filtration (TFF) module which can, under some circumstances, lead to back-filtration near the device exit. The key thermodynamic (virial coefficients) and hydrodynamic (viscosity) properties were evaluated from independent experimental measurements as discussed in Chapters 4 and 6. The model predictions are compared with experimental data for the ultrafiltration of the same antibody in a linearly scalable screened TFF cassette used extensively in bioprocessing applications for final product formulation. The model is in good agreement with the experimental results, providing important additional insights into the key factors controlling the filtrate flux during ultrafiltration of highly concentrated protein solutions.

7.2 Theoretical development

7.2.1 Modified Polarization Model

As discussed by Zydney [63], the diffusive solute flux in highly concentrated solutions is proportional to the gradient in the chemical potential (μ) instead of the gradient in the solute concentration, so that Equation (2.10) becomes:

$$N_s = -J_v C - \frac{DC}{RT}\left(\frac{d\mu}{dy}\right) \tag{7.2}$$

The gradient in the chepmical potential can be rewritten in terms of the protein osmotic pressure (Π) as:

$$\left(\frac{d\mu}{dy}\right) = \left(\frac{MW}{C}\right)\left(\frac{d\Pi}{dC}\right)\left(\frac{dC}{dy}\right) \tag{7.3}$$

where the osmotic pressure is conveniently expressed using a virial expansion as discussed in Chapter 4:

$$\Pi = RT\left\{2\left[\left(\frac{ZC_p}{2M_p}\right)^2 + {m_s}^2\right]^{\frac{1}{2}} - 2m_s\right\} + RT\left(B_1 C + B_2 C^2 + B_3 C^3\right) \tag{7.4}$$

where the first term is the Donnan contribution. Equation (7.4) has been truncated after the third osmotic virial coefficient (B_3), which is sufficient to describe the behavior of concentrated monoclonal antibody solutions up to concentrations of at least 250 g/L. Note that the analysis presented by Zydney [63] only considered the term involving the second virial coefficient and did not account for the Donnan contribution. The diffusion

coefficient in Equation (7.2) is also a function of the protein concentration due to the dependence of the protein mobility on the local solution viscosity:

$$D = D_0\left(\frac{\eta_0}{\eta}\right) \tag{7.5}$$

where D_o and η_o are the diffusivity and viscosity in the limit of an infinitely dilute solution. Note that Equation (7.5) is consistent with the Stokes-Einstein equation as discussed by Kozinski and Lightfoot [50]. Equations (7.3) to (7.5) can be substituted into Equation (7.2), with the resulting equation integrated over the concentration boundary layer thickness (δ) to give the following expression for the filtrate flux:

$$J_v = \frac{D_0}{\delta}\int_{C_b}^{C_w}\left(\frac{\eta_0}{\eta}\right)\left(\frac{d\Pi}{dC}\right)\frac{dC}{C} \tag{7.6}$$

where D_0/δ is related to the mass transfer coefficient and the derivative of the osmotic pressure with respect to the protein concentration can be evaluated from Equation (7.4). Equation (7.6) reduces to the classical stagnant film model (Equation 7.1) when the solution viscosity is constant ($\eta = \eta_o$) and $Z = B_2 = B_3 = 0$, i.e., for an uncharged protein under conditions where there are no intermolecular interactions. Equation (7.6) can be integrated using an appropriate relationship for the viscosity as a function of the protein concentration; this is discussed in more detail in Section 7.4.

The boundary layer thickness in Equation (7.6) is determined by the module geometry (e.g., channel height, spacer, module length, etc.) as well as the device hydrodynamics (e.g., feed flow rate). In addition, the boundary layer thickness depends on $Sc^{1/3}$ where Sc is the Schmidt number [139]. Therefore to take into account the effect

of changes in the boundary layer thickness on the mass transfer coefficient, Equation (7.6) was rewritten as:

$$J_v = k_0 \left(\frac{\eta_b}{\eta_0} \right)^{1/3} \int_{C_b}^{C} \left(\frac{\eta_0}{\eta} \right) \left(\frac{d\Pi}{dC} \right) \frac{dC}{C} \tag{7.7}$$

where k_o is the mass transfer coefficient that would exist in the absence of any non-idealities.

As discussed in Chapter 2, there is considerable debate in the literature over the factors that determine the wall concentration in the stagnant film model. Some investigators have evaluated the wall concentration based on the solubility (or "gel") concentration for the particular protein, while others have assumed that the wall concentration is determined by the osmotic pressure, in which case C_w can be evaluated by simultaneous solution of the concentration polarization model (Equation 7.1 or 7.7) and the equation describing the volumetric flux across the membrane (Equation 2.2). Since the membrane used in this work is fully retentive to the model antibody, the protein concentration in the filtrate is zero and the osmotic pressure difference is simply equal to the osmotic pressure evaluated at the protein concentration at the membrane surface, C_w. The evaluation of the wall concentration is discussed in more detail subsequently.

7.2.2 Pressure Effects

Equation (7.7) describes the local filtrate flux in a tangential flow filtration (TFF) device. The length-average filtrate flux (or the volumetric filtrate flow rate) would then be evaluated by integrating Equation (7.7) along the length of the module. In dilute

solutions, the pressure drop due to flow through the channel is relatively small, in which case the transmembrane pressure drop is often taken as a constant at its mean value. At higher feed concentrations, the solution viscosity becomes quite high, in which case the transmembrane pressure will vary with position:

$$\frac{d}{dz}\left(\Delta P_{TM}\right) = a\frac{12\eta Q}{wh^3} \tag{7.8}$$

where Q is the local volumetric flow rate, z is the position along the length of membrane, w is the channel width, and h is the channel height. The viscosity in Equation (7.8) should be evaluated at an appropriate mean value to account for the variation in protein concentration (and thus viscosity) across the concentration polarization boundary layer. If the boundary layer is sufficiently thin, η can simply be evaluated at the bulk protein concentration. The coefficient a is a correction factor that accounts for the additional parasitic pressure losses associated with the screen in the TFF cassette; $a = 1$ in an open channel. Equation (7.8) was used by Subramani et al. [140] to evaluate the pressure drop in a spacer filled channel with a =1.5 – 5 depending upon the channel geometry and flow rate.

The effect of the pressure gradient on the ultrafiltration is shown schematically in Figure 7.1. The y-axis shows the dimensionless transmembrane pressure and the bulk osmotic pressure, both scaled by the average transmembrane pressure difference in the module. The osmotic pressure is evaluated at the inlet concentration, which neglects the small variation in bulk protein concentration as one moves through module. This effect is relatively small since typical TFF modules in bioprocessing operate at low conversion

(ratio of permeate to feed flow rates of less than 0.1). At low feed concentrations (left panel), the transmembrane pressure will be relatively uniform throughout the module with a value that is significantly greater than the osmotic pressure evaluated at the bulk protein concentration. There is thus a net positive driving force for filtration (as given by Equation 2.2) along the entire length of the module. The situation is very different at high feed concentrations due to the large increase in both the osmotic pressure and the solution viscosity under these conditions. The large parasitic pressure loss due to flow through the module causes a large variation in the transmembrane pressure over the length of the channel, with ΔP_{TM} dropping below the bulk osmotic pressure over the final portion of the module (right panel). This leads to a reverse or back-filtration near the module exit (Equation 2.2). The implications of this back-filtration on the overall ultrafiltration behavior are discussed subsequently.

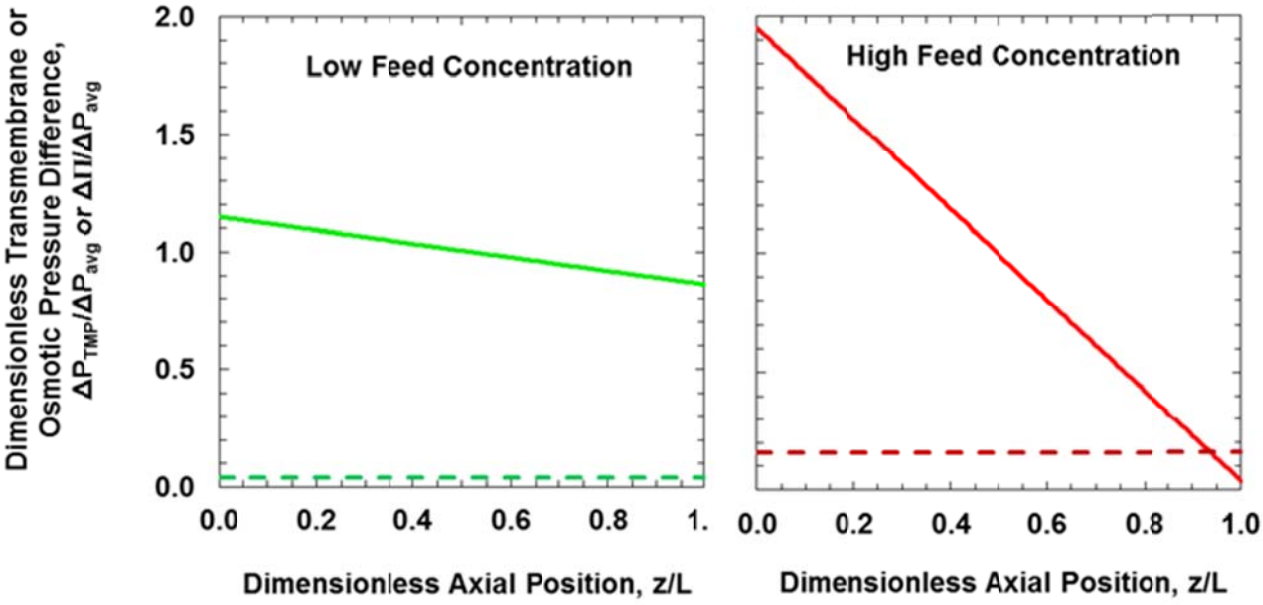

Figure 7.1. Schematic diagram showing the variation in the transmembrane pressure and the osmotic pressure at both low (left panel) and high (right panel) feed concentrations.

7.3 Materials and Methods

7.3.1 Protein Solution

A highly purified humanized monoclonal antibody was provided by Amgen with a molecular weight of 142 kDa and isoelectric point of 8.16. The antibody was stored at -80°C and slowly thawed prior to use. The antibody was placed in the desired buffer by diafiltration at low filtrate flux through a fully retentive Ultracel^{TM} composite regenerated cellulose membrane with 30 kDa nominal molecular weight cut-off (Millipore Corp., Bedford, MA). The resulting protein solution was kept at 4°C for up to a week; solutions used for longer periods of time were kept at -30°C. More details regarding preparation of the protein solutions are provided in Chapter 3.

7.3.2 Ultrafiltration

Ultrafiltration experiments were performed using Pellicon 3 tangential flow filtration (TFF) cassettes with C screen channel provided by EMD Millipore (Bedford, MA). The cassettes housed 30 kDa Ultracel composite regenerated cellulose membranes with a total filtration area of 88 cm^2 membrane. The channel dimensions were measured to be approximately L = 20 cm and w = 2.2 cm, yielding a membrane area of 88 cm^2 since the module has two flat sheet membranes (one on each side). The channel height

was estimated as h = 0.024 cm based on manufacturer's data for the feed channel hold-up volume (1.5 mL) assuming that the spacer occupies 30% of the channel. Cassettes were installed in the cassette holder using the procedures provided by the manufacturer. The modules were then flushed with at least 30 L/m^2 of the specific buffer to be used in the ultrafiltration experiment. Modules were cleaned by recirculating a 0.3 N NaOH solution for 30-60 min and stored in 0.1 N NaOH between experiments.

The feed was driven through the module using a positive displacement pump (Masterflex, Gelsenkirchen, Germany), with the inlet (feed) and exit (retentate) pressures evaluated using analog pressure gauges (Ashcroft, Stratford, CT). The permeate line was simply kept at atmospheric pressure. The membrane hydraulic permeability was evaluated from data for the filtrate flux (using DI water) as a function of the transmembrane pressure using Equation (3.4). The feed reservoir was then filled with the antibody solution. The transmembrane pressure was set by adjusting a pinch valve on the retentate exit line, with the permeate flow rate evaluated by timed collection of permeate samples. Experiments were performed in a batch concentration mode, with the retentate recycled back to the feed reservoir while the permeate was removed. The filtrate flux was measured as a function of time, corresponding to different bulk protein concentrations, as the feed volume was reduced. Permeate and feed samples were taken periodically to evaluate the bulk protein concentration and sieving coefficient using a NanoDrop 2000c spectrophotometer (Thermo Scientific, Waltham, MA) with the absorbance measured at 280 nm. Additional details on the ultrafiltration experiments are provided in Chapter 3.

7.4 Results and Discussion

7.4.1 Filtrate Flux

Figure 7.2 shows experimental data for the filtrate flux as a function of the bulk protein concentration during ultrafiltration of the monoclonal antibody in a 5 mM acetate buffer with 20 mM NaCl at pH 5. The data were obtained as part of a single experimental run using a feed flow rate of Q = 45 mL/min (corresponding to a feed flux of Q/A = 85 μm/s = 310 L/m^2/h), with the protein concentration increasing as a function of time as permeate was removed. The average transmembrane pressure $(\frac{P_{feed} + P_{retentate}}{2} - P_{filtrate})$ was kept constant at 15 psi (105 kPa) by continually adjusting the clamp on the retentate exit. However, when the bulk protein concentration was approximately 170 g/L, it was necessary to fully open the retentate clamp so that $P_{retentate} \approx P_{filtrate}$. Further increases in the bulk protein concentration caused additional increases in the feed pressure (due to the increase in solution viscosity), leading to a corresponding rise in the average transmembrane pressure.

Antibody concentrations in the initial filtrate samples were undetectable (corresponding to concentrations less than 0.01 g/L). Low levels of antibody were detected at the highest feed concentrations, corresponding to a sieving coefficient of around 0.006 (99.4% retention). Overall mass balance closure was good, with the final mass of antibody (accounting for the volume in the feed reservoir, tubing, and module) being more than 90% of the initial mass – most of the "loss" was in the feed samples taken during the course of the experiment. The membrane permeability evaluated at the

end of the experiment (after gently rinsing the module with buffer) was 13% smaller than the initial permeability, suggesting a small amount of irreversible fouling. The permeability could be restored to within a few percent of the initial value after cleaning with 0.3 N NaOH.

The filtrate flux during the ultrafiltration decreased with increasing bulk protein concentration as expected, with the data looking nearly linear when plotted as a function of the logarithm of the bulk protein concentration as suggested by Equation (7.1) (results in Figure 7.2). The maximum achievable protein concentration for this experiment was approximately 225 g/L, which was attained after 1 hr of ultrafiltration; continued circulation of the feed through the module for an additional 3 hr gave no measurable filtrate flux and thus no change in the feed concentration. The dashed line in Figure 7.2 is the filtrate flux given by the simple stagnant film model (Equation 7.2) using C_w = 225 g/L and k_m = 5.8 μm/s (21 L/m^2/h).

Although the simple stagnant film model appears to be in good agreement with the data, there are two major problems with this analysis. First, the calculated value of the wall concentration (C_w = 225 g/L) is well below the gel concentration for this monoclonal antibody, and it is also well below the value needed to provide the necessary osmotic pressure to limit the filtrate flux. Data for the osmotic pressure for this antibody in identical buffer conditions from Chapter 4 give $\Delta\Pi$ = 44 kPa at a protein concentration of 225 g/L. The filtrate flux evaluated from Equation (2.2) using this value of $\Delta\Pi$ and a transmembrane pressure of 105 kPa is J_v = 42 μm/s (based on the "fouled" membrane permeability), which is several times larger than the measured filtrate flux at the very start of the experiment (i.e., at a bulk protein concentration of <30 g/L). A much higher

wall concentration would be needed to give the measured values of the filtrate flux seen in Figure 7.2.

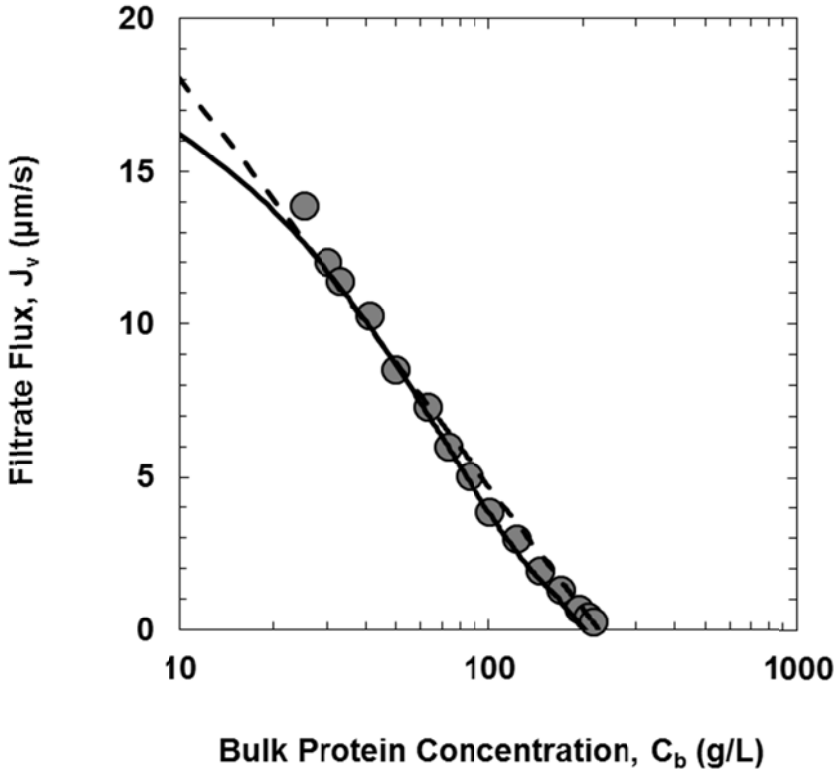

Figure 7.2. Experimental data for the filtrate flux as a function of the bulk monoclonal antibody concentration during ultrafiltration through the Pellicon 3 module. Data were obtained using a 5 mM acetate buffer with 20 mM added NaCl at pH 5 with a feed flow rate of 45 mL/min. Dashed line is the simple stagnant film model (Equation 7.1) with k_m = 5.8 µm/s and C_w = 225 g/L and solid curve is the modified polarization model developed in this work.

In addition to the problem with C_w, the filtrate flux data in Figure 7.2 show a small but significant curvature on the semi-log plot. This can be seen much more easily by evaluating the slope:

$$\frac{dJ_v}{d(\ln C_b)} = C_b \frac{dJ_v}{dC_b} \tag{7.9}$$

using finite difference representations for the derivative accounting for the non-uniform spacing of the bulk concentration data. Figure 7.3 shows the variation in the slope as a function of bulk protein concentration. The calculated values of the slope initially decrease with increasing bulk protein concentration but then appear to go through a weak minimum around C_b = 170 g/L. This is in sharp contrast to the constant value of the slope (equal to the mass transfer coefficient) given by Equation (7.1). This will be discussed in more details in section 7.4.

The solid curve in Figure 7.3 is developed from the modified polarization model (Equation 7.7), with the viscosity of the antibody solution given as:

$$\frac{\eta}{\eta_0} = \exp\left(\frac{bC}{1 - C/C_{\max}}\right) \tag{7.10}$$

with b = 0.0108 L/g and C_{max} = 800 g/L based on the experimental correlation developed in Chapter 6. Equation (7.7) is integrated numerically in Mathematica with $B_2 = 4.4\times10^{-4}$ $m^3.mol/kg^2$ and $B_3 = -11\times10^{-7}$ $m^6.mol/kg^3$ as determined from osmotic pressure measurements and Z = 14 (from electrophoretic light scattering) using k_o = 1.6 μm/s and C_w = 330 g/L (the evaluation of k_o and C_w is discussed in more detail subsequently). The slope is then evaluated by numerical differentiation of an interpolation function that is fit to the integral using Mathematica. The slope given by this modified polarization model is in very good agreement with the experimental data for C_b < 170 g/L, properly capturing the changes in slope with increasing bulk protein concentration. However, the

model is unable to explain the increase in the slope at very high protein concentrations – the predicted slope given by Equation (7.7) decays to zero as C_b approaches C_w.

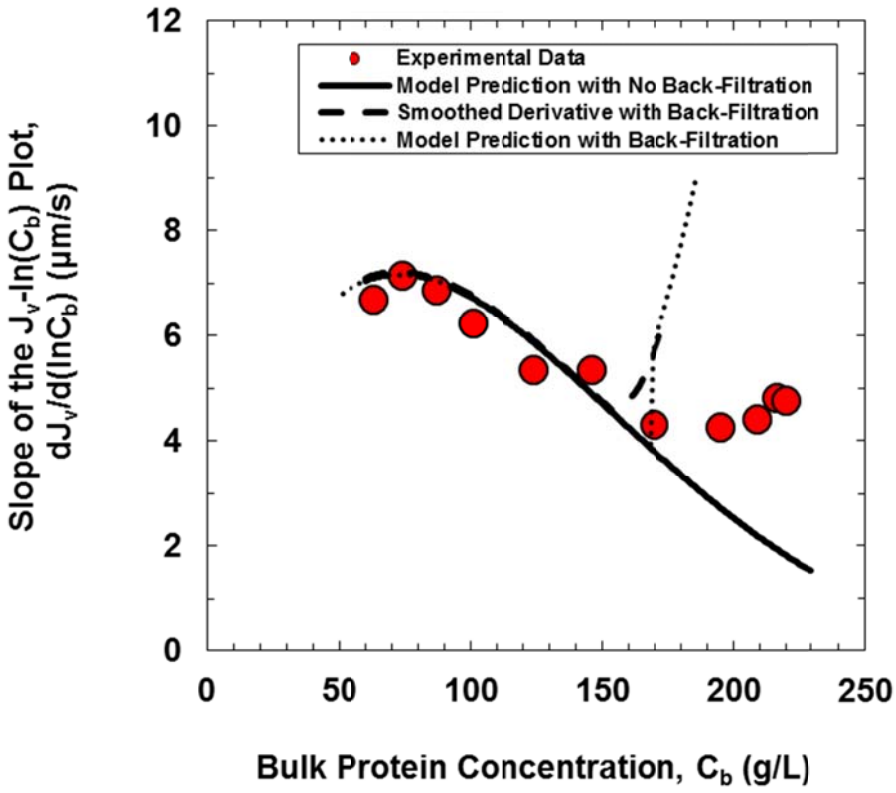

Figure 7.3. Calculated values of the slope, $dJ_v/d(\ln C_b)$ as a function of the bulk protein concentration from the data in Figure 7.2. Solid, dashed and dotted curves are model calculations as described in the text.

7.4.2 Back-Filtration

As discussed previously, the ultrafiltration behavior at high protein concentrations is complicated by the large pressure drop due to flow of the highly viscous protein

solution through the TFF module. Figure 7.4 shows experimental data for the module pressure drop, $\Delta P_{module} = P_{feed} - P_{retentate}$, as a function of the bulk protein concentration (top panel). The pressure drop is less than 50 kPa for the dilute solutions but increases to more than 400 kPa (58 psi) at a bulk protein concentration of 217 g/L. The solid curve shows the calculated values of the pressure drop given by integration of Equation (7.8) assuming that the volumetric flow rate (Q) and the solution viscosity (η) are both constant at their inlet (bulk) values. The integration was performed over a length $L + 2L_o$ to account for the pressure drop across the inlet and outlet headers of the module (each modeled as having an effective length $L_o = 0.01$ m using the same channel height as in the rest of the module). Note that a filtrate flux of 10 μm/s (corresponding to a bulk protein concentration of 40 g/L) gives a volumetric filtrate flow rate of 5.3 mL/min, which is less 12% of the feed flow rate; the variation in Q is significantly smaller at high C_b due to the reduction in filtrate flux. The model calculations, using the best fit value of the channel correction factor ($a = 2.5$), are in very good agreement with the data over the entire range of bulk protein concentrations.

The lower panel in Figure 7.4 shows the corresponding values of the exit transmembrane pressure. At low bulk protein concentrations, the exit transmembrane pressure is nearly constant at a value of 90 kPa, consistent with the 35 kPa pressure drop through the module (with the mean $\Delta P_{TM} = 105$ kPa). The exit transmembrane pressure decreased as the bulk protein concentration increased so that the average transmembrane pressure remained constant. The pinch clamp was fully opened at a bulk protein concentration of 170 g/L, with the exit transmembrane pressure becoming approximately equal to the filtrate pressure at bulk concentrations above this value. Also shown for

comparison are the calculated values of the bulk osmotic pressure, i.e., the osmotic pressure evaluated at $C = C_b$. The bulk osmotic pressure is much less than the exit transmembrane pressure at low protein concentrations, but the situation is reversed at high C_b, giving rise to a reverse filtration in the latter portion of the module (as given by Equation 2.2). The value of the bulk protein concentration at the onset of reverse filtration, i.e., when ΔP_{TM} first drops below $\Delta\Pi$, can be evaluated as:

$$\overline{\Delta P}_{TM} - \frac{6aQ\eta_b L}{wh^3} = \Pi_b \tag{7.11}$$

where η_b and Π_b are the viscosity and osmotic pressure evaluated at $C = C_b$ using Equations (7.10) and (7.4), respectively. Equation (7.11) can be solved iteratively using a mean transmembrane pressure of $\overline{\Delta P}_{TM}$ = 105 kPa giving C_b = 165 g/L, in excellent agreement with the results in Figure 7.4. Note that this is also close to where the model and data begin to diverge in Figure 7.3, i.e., the inability of Equation (7.7) to accurately predict the slope at high bulk protein concentrations is directly due to the onset of back-filtration in the TFF cassette.

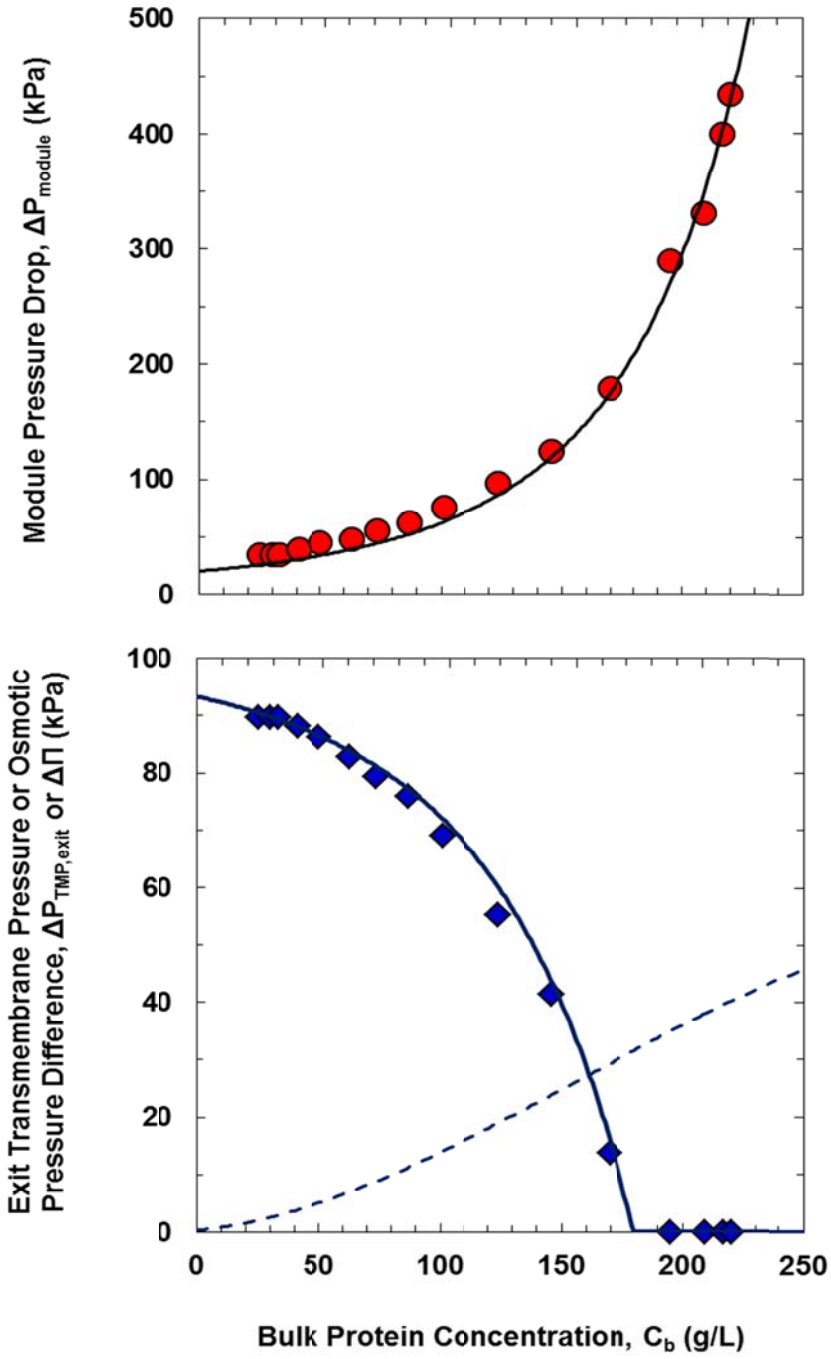

Figure 7.4. Experimental data for the module pressure drop (top panel) and the exit transmembrane pressure (bottom panel) as a function of the bulk protein concentration. Solid curve in top panel is the model calculation obtained by integration of Equation (7.8) as described in the text. Dashed curve in bottom panel is the bulk osmotic pressure calculated using Equation (7.4).

In order to properly evaluate the filtrate flux at high bulk protein concentrations, it is necessary to account for the effect of back-filtration on the total volumetric filtrate flow rate through the membrane. Equation (7.7) was used to evaluate the positive flux in the first portion of the module, where $\Delta P_{TM} > \Pi_b$, while Equation (2.2) was used to evaluate the reverse flux in the latter portion of the module assuming that $\Delta\Pi = \Pi_b$. The protein concentration at the membrane surface in the region of reverse filtration is likely to be a complex function of the module and fluid flow due to the "reverse concentration polarization" in combination with the convective transport of the protein within the highly concentrated boundary layer further down the module. The use of the bulk protein concentration to evaluate $\Delta\Pi$ should provide a reasonable approximation to this more complex situation. In addition, the effective membrane permeability ($L_{p.eff}$) for flow in the reverse direction will be less than the true membrane permeability due to concentration polarization effects as discussed in Chapter 4:

$$J_{back} = \left[\frac{L_P}{1 + \frac{L_p C_b}{k_{back}} \left(\frac{d\Pi}{dC} \right)_{C_b}} \right] \left[\Delta P_{TM} - \Delta \Pi_b \right] \tag{7.12}$$

where ΔP_{TM} is the local transmembrane pressure, which decreases with increasing position (z) in the module, and k_{back} is the mass transfer coefficient in the region of back-filtration.

The location at which back-filtration first occurs, denoted as the cross-over point z^*, can be determined by solving for z corresponding to $\Delta P_{TM} = \Pi_b$ (with z = 0 corresponding to the entrance to the membrane, i.e., after the inlet header) giving:

$$z^* = \frac{wh^3}{12aQ\eta_b}\left[\Pi_b - \bar{\Delta}\bar{P}_{TM}\right] + \frac{L}{2} \tag{7.13}$$

for $\Delta P_{TM,exit} > 0$ and

$$z^* = L + L_o - \frac{wh^3}{12aQ\eta_b}\Pi_b \tag{7.14}$$

for $\Delta P_{TM,exit} = 0$ (i.e., at high feed concentrations where the exit retentate clamp is fully open). z^* moves inward as C_b increases, going from $z^* = L$ at C_b = 165 g/L to z^*/L = 0.87 at C_b = 183 g/L for an inlet feed flow rate of 45 mL/min.

The solid curve in Figure 7.2 represents the calculated values of the filtrate flux given by the polarization model accounting for back-filtration, while the dashed curve in Figure 7.3 represents the calculated values of the slope. The model calculations for the flux are in excellent agreement with the experimental data over the full range of antibody concentrations. The dashed and dotted curves in Figure 7.3 are identical to the solid curve for C_b < 170 g/L, i.e. under conditions where there is no back-filtration. However, the complete model, which accounts for the effects of back-filtration, is able to capture the observed increase in slope at the highest bulk concentrations. The dotted curve in Figure 7.3 is the detailed model calculation using Mathematica – the model predicts a sharp jump in slope at the onset of back-filtration (leading to a rapid decrease in the flux). The dashed curve in Figure 7.3 is the "smoothed" derivative, calculated by numerical differentiation of the model using a centered difference representation with ΔC = 15 g/L. This smoothed derivative provides a better representation of the experimental results, which were determined by numerical differentiation of the discrete flux values – this type

of numerical differentiation is unable to capture the type of discontinuous change in the derivative seen in the full model. The discrepancies between the model and experimental results for slope at the high protein concentrations is likely due to a combination of the numerical differentiation along with difficulties in evaluating the back-filtration flux in the region where the local transmembrane pressure is less than the local bulk osmotic pressure difference across the membrane.

7.4.3 Modified Polarization Model

The effects of intermolecular interactions on bulk mass transfer can be described by the function that multiplies the term *dC/C* in Equation (7.7). The calculated values of the intermolecular interaction function, *f*,

$$f = \left(\frac{MW}{RT}\right)\left(\frac{\eta_0}{\eta}\right)\left(\frac{d\Pi}{dC}\right) \tag{7.15}$$

were evaluated using the previously determined values of the virial coefficients and viscosity for the monoclonal antibody solution with the results for the pH 5 acetate buffer with 20 mM NaCl shown in Figure 7.5. The horizontal dashed line shows $f = 1$ as would be the case in the absence of any intermolecular interactions (i.e., as assumed in the classical stagnant film model). The intermolecular interaction function for the monoclonal antibody is equal to one at $C = 0$ but initially increases with increasing bulk protein concentration due to the higher order terms in the expression for the protein osmotic pressure (Chapter 4). The function *f* attains its maximum value of $f \approx 4.4$ at $C_b \approx$ 55 g/L and then decreases sharply at higher protein concentrations due to the rapid

increase in the solution viscosity (Chapter 6). Interestingly, the average value of f determined by integration over the intermolecular interaction function from C = 100 to 330 g/L is approximately equal to one. Under these conditions, the increase in back transport associated with the increase in the chemical potential gradient is almost exactly balanced by the reduction in the protein mobility due to the increased viscosity.

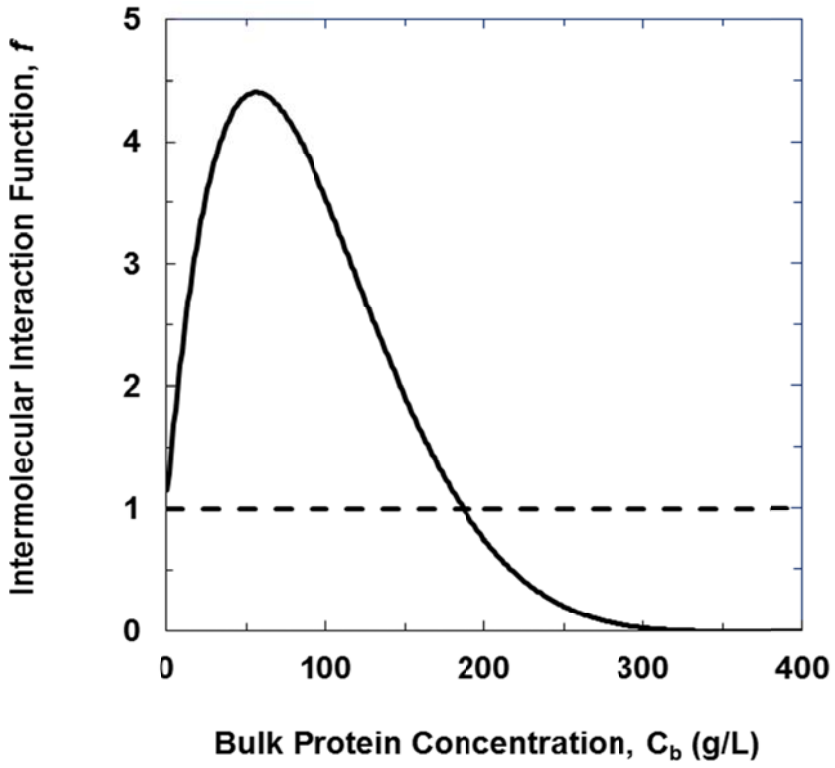

Figure 7.5. Intermolecular interaction function in Equation (7.7) as a function of the protein concentration. Dashed line is f = 1 as in the classical stagnant film model.

In order to evaluate the filtrate flux by integration of Equation (7.7), it is first necessary to determine the protein concentration at the membrane surface, C_w. Although the wall concentration likely varies with transverse position in the module due to the

change in the local transmembrane pressure, an average value for the wall concentration was determined based on the assumption that the filtrate flux is limited by the osmotic pressure of the highly concentrated protein solution in the immediate vicinity of the membrane surface (i.e., at $C = C_w$). The extrapolated values of the osmotic pressure given by the virial expansion developed in Chapter 4 (Equation 4.5) goes through a maximum at C_w = 330 g/L due to the negative value of the third virial coefficient; extrapolation to higher concentrations would require values of the higher order virial coefficients. Model calculations were thus performed using C_w = 330 g/L, which eliminated any artifacts associated with the negative values of f at protein concentrations above this value. Model calculations performed over a range of C_w values (from 300 to 500 g/L) gave essentially identical values of the filtrate flux. The best fit value of k_o was then determined by minimizing the sum of the squared residuals between the model (numerical integration of Equation 7.7) and the experimental data under conditions where there was no back-filtration, i.e., for filtrate flux values at C_b < 170 g/L. This gave k_o = 1.6 μm/s based on the experimental data in Figure 7.2. The mass transfer coefficient for back-filtration was estimated as $k_{back} = 5.5\ k_o$ which accounts (at least approximately) for the enhancement in mass transfer arising from the chemical potential driving force in Equation (7.2).

The model calculations at the highest bulk protein concentrations were performed by accounting for the effects of back-filtration. In this case, numerical integration of Equation (7.7) was only used in the region where $\Delta P_{TM} > \Pi_b$, with Equation (7.12) used

to evaluate the reverse flux where $\Delta P_{TM} < \Pi_b$. Since the transmembrane pressure varies linearly with position, the net flux under these conditions is given as:

$$J_v = k_0 \left[\frac{\eta_b}{\eta_0}\right]^{1/3} \left[\int_{C_b}^{C_w} \left(\frac{MW}{RT}\right)\left(\frac{\eta_0}{\eta}\right)\left(\frac{d\Pi}{dC}\right)\frac{dC}{C}\right]\left(z^*/L\right) - \left(\frac{L_{P,eff}}{\eta_0}\right)\left[\frac{6Q\eta_b aL}{wh^3}\right]\left[\left(1 - z^*/L\right)^2 + 2\,L_0/L\left(1 - z^*/L\right)\right] \tag{7.16}$$

where C_w has been taken as a constant in the entire region with positive filtration and z^* is the position at which $\Delta P_{TM} = \Pi_b$ as given by Equation (7.12) or (7.13). The presence of this back-filtration leads to a maximum achievable antibody concentration that is much smaller than the wall concentration (C_w = 330 g/L). Under these conditions, the positive filtrate flux over the first part of the channel exactly balances the reverse (back-filtration) flux near the channel inlet, leading to a net flux of zero (as given by Equation 7.15).

Figures 7.6 and 7.7 show a comparison between the model calculations and the experimental results during ultrafiltration of the monoclonal antibody at feed flow rates of 25, 45, and 65 mL/min through the Pellicon 3 module. The solid curves are the model calculations given by Equation (7.16), with the k_o values at 25 and 65 ml/min determined by scaling as $Q^{1/2}$ based on the correlation for mass transfer in a screened module [141]. The wall concentration was fixed at 330 g/L for all three feed flow rates since the data were all obtained at the same mean transmembrane pressure. The model calculations are in very good agreement with the experimental results for both the filtrate flux (Figure 7.6) and the smoothed slope (Figure 7.7) at all 3 flow rates, with the smoothed sloped determined by numerical differentiation of the model calculations as described

previously. The minimum in the slope shifts to lower bulk protein concentrations as the feed flow rate increases due to the increase in the pressure drop associated with the flow through the module. In addition, the model accurately predicts the values of the maximum achievable protein concentration, i.e., the concentration at which the filtrate flux equals zero. The model is unable to quantitatively describe the increase in the slope after the onset of back-filtration, which is likely due to the approximations involved in using Equation (7.12) to evaluate the back-filtration flux.

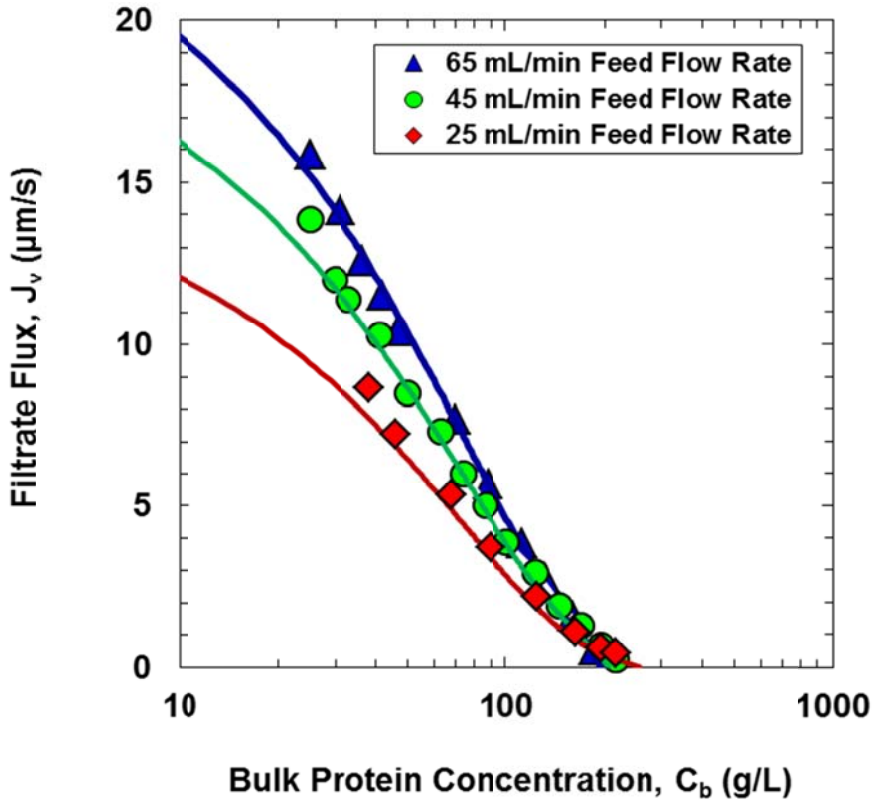

Figure 7.6. Experimental data for the filtrate flux as a function of the bulk protein concentration during ultrafiltration of the monoclonal antibody in the Pellicon 3 module at different feed flow rates. Data were obtained using a 5 mM acetate buffer with 20 mM added NaCl at pH 5. Solid curves are model calculations developed using the modified polarization model accounting for back-filtration.

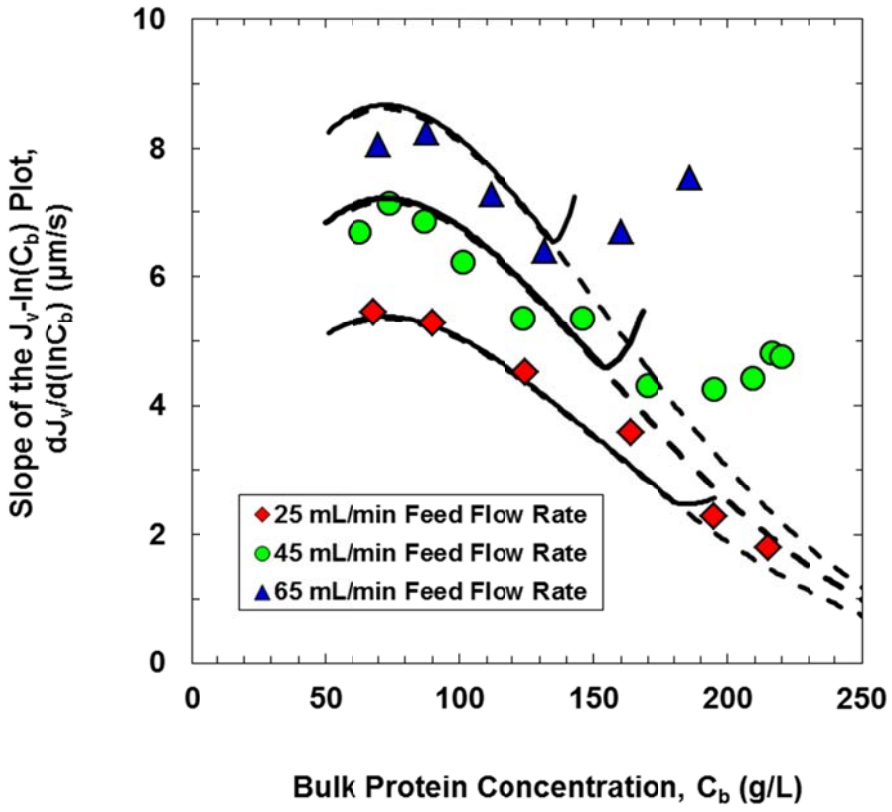

Figure 7.7. Experimental data for the calculated values of the slope, $dJ_v/d(\ln C_b)$ during ultrafiltration of the monoclonal antibody in the Pellicon 3 module at different feed flow rates. Data were obtained using a 5 mM acetate buffer with 20 mM added NaCl at pH 5. Solid curves are model calculations developed using the modified polarization model accounting for back-filtration.

The effect of the feed flow rate on the maximum achievable antibody concentration is examined more explicitly in Figure 7.8. The results are plotted as the normalized maximum achievable concentration, C_{max}/C_w, as a function of the feed flow rate, with the filled symbols representing the extrapolated values of C_{max} from the filtrate flux data in Figure 7.6. The maximum achievable protein concentration decreases with increasing feed flow rate due to the increase in the pressure drop through the module and

the corresponding increase in the extent of back-filtration. The maximum achievable antibody concentration could only be increased to 255 g/L by decreasing the feed flow rate to 25 mL/min.

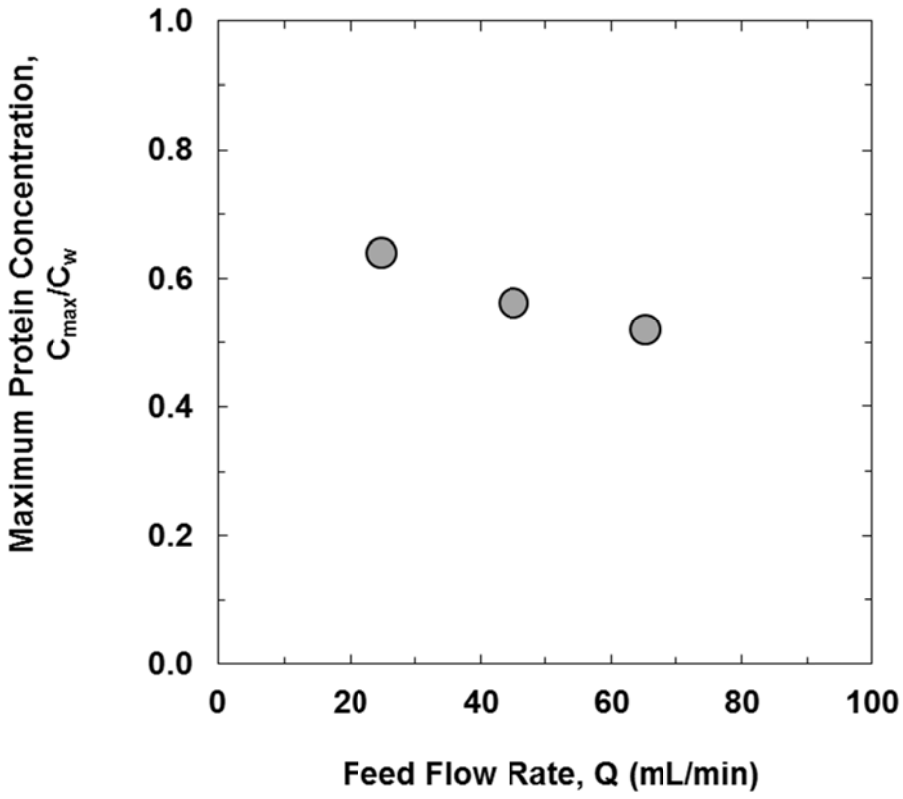

Figure 7.8. Maximum achievable antibody concentration as a function of feed flow rate. Data were obtained using a 5 mM acetate buffer with 20 mM added NaCl at pH 5.

7.5 Conclusions

The need to formulate monoclonal antibody products at very high protein concentrations (above 200 g/L) has created major challenges for the design and application of ultrafiltration processes for final formulation of monoclonal antibodies. A new mathematical model was developed specifically to describe the filtrate flux behavior during ultrafiltration of these highly concentrated monoclonal antibody solutions. The model includes two basic phenomena: (1) the filtrate flux over most of the channel is evaluated using a modified form of the stagnant film model in which the driving force is expressed in terms of the gradient in the chemical potential (evaluated using data for the osmotic virial coefficients) with the protein mobility accounting for the concentration dependence of the solution viscosity, and (2) the large parasitic pressure losses due to flow through the screened channel (particularly at high bulk protein concentrations) causes a negative filtrate flux, or back-filtration, near the exit of the module where the transmembrane pressure becomes less than the osmotic pressure. This back-filtration reduces the value of the length-average filtrate flux, and it causes the maximum or limiting value of the antibody concentration, i.e., the antibody concentration at which the filtrate flux equals zero, to drop well below the wall concentration.

Model calculations were performed for a highly purified monoclonal antibody (provided by Amgen) based on independent measurements for the osmotic pressure and virial coefficients (Chapter 4) and the solution viscosity (Chapter 6) up to protein concentrations of at least 250 g/L. The model was in good agreement with experimental data obtained in a linearly-scalable Pellicon 3 tangential flow filtration module

commonly used in downstream processing of monoclonal antibodies. The model properly captures the observed variation of the filtrate flux with bulk protein concentration, including the complex dependence of the slope in the plot of flux versus the logarithm of C_b. In addition, the model is able to accurately predict the maximum achievable protein concentration and its dependence on the feed flow rate; increasing the feed flow rate leads to a reduction in the maximum achievable protein concentration due to the increase in back-filtration arising from the larger pressure loss associated with flow through the channel. Thus, it should be possible to obtain antibody formulations with higher protein concentration by decreasing the feed flow rate towards the end of the ultrafiltration process; high feed flow rates can be used over most of the ultrafiltration to provide high filtrate flux while the low feed flow rate in the final stage of the ultrafiltration reduces the extent of back-filtration by reducing the parasitic pressure losses. This model provides new insights into the ultrafiltration behavior of highly concentrated protein solutions as well as an appropriate framework for the design and analysis of ultrafiltration processes / systems for the formulation important recombinant protein products.

Chapter 8

Ultrafiltration Behavior of Highly Concentrated Monoclonal Antibody Solutions: Effect of Physicochemical and Operating Conditions

8.1 Introduction

The growing interest in developing high concentration formulations for monoclonal antibody products [15, 17] requires a fundamental understanding of the key factors controlling the ultrafiltration behavior of highly concentrated monoclonal antibody solutions, including the dramatic decrease in filtrate flux at high bulk protein concentrations which limits the maximum achievable concentration [15, 18]. The modified concentration polarization model developed in Chapter 7 provides an appropriate theoretical framework for the analysis of these ultrafiltration phenomena. The objective of the studies described in this chapter are to use that model framework to examine the effects of module geometry (e.g., spacer design and TFF cassette versus hollow fiber) and solution conditions (e.g., pH, ionic strength, and presence of excipients) on antibody ultrafiltration.

8.2 Materials and Methods

8.2.1 Protein Solutions

A highly purified humanized monoclonal antibody was provided by Amgen with a molecular weight of 142 kDa and isoelectric point of 8.16. The antibody was stored at -80°C and slowly thawed prior to use. The antibody was placed in the desired buffer by diafiltration at low filtrate flux through a fully retentive Ultracel™ composite regenerated cellulose membrane with 30 kDa nominal molecular weight cut-off (Millipore Corp., Bedford, MA). Protein solutions with different pH (5, 6, and 7), different ionic strength (10, 20, and 100 mM NaCl), and different excipients (arginine, L-proline, or sucrose) were prepared as described in Chapter 3. The resulting protein solutions were kept at 4°C for up to a week; solutions used for longer periods of time were kept at -30°C.

8.2.2 Ultrafiltration

Ultrafiltration experiments were performed using Pellicon 3 tangential flow filtration (TFF) ultrafiltration cassettes (Millipore Corp., Bedford, MA) and MicroKros® hollow fiber modules (Spectrum Labs, Rancho Dominguez, CA). The Pellicon 3 cassettes have screened channels and house two flat sheet 30 kDa Ultracel composite regenerated cellulose membranes with channel length of 20 cm and width of 2.2 cm, providing a total membrane area of 88 cm^2. Modules were examined with both C (Millipore, P3C030C00) and D (Millipore, P3C030D00) screens; the D screen cassettes are specifically designed to accommodate highly viscous solutions. The channel heights for the Pellicon 3 cassettes

were estimated as follows. The hold-up volume for the feed channel in the C screen cassette is given by the manufacturer as 1.5 mL – this gives a channel height of h = 240 μm assuming that the screen occupies 30% of the channel volume. The manufacturer's value for the hold-up volume for the D screen cassette is given as 4 mL (more than 2.5 times the hold-up volume for the C screen cassette), but this provides an unrealistic estimate for the channel height. The ratio of the hold-up volumes for the D-screen and C-screen cassettes for Pellicon 3 modules with 0.11, 0.57, and 1.14 m^2 membrane area was around 1.3. This ratio was used to calculate the channel height assuming that the D screen occupies 10% of the channel volume giving a channel height of h = 240 μm. This value was used in all subsequent calculations for the D screen cassette.

Cassettes were installed in the cassette holder and prepared for use in the ultrafiltration experiments using the procedures provided by Millipore. All modules were initially flushed with at least 500 mL of DI water to remove the shipping / storage solution and thoroughly wet the membrane pore structure. The modules were then flushed with 300 mL of the specific buffer to be used in the protein ultrafiltration. After each experiment, the module was cleaned by recirculating a solution of 0.3 N NaOH at pH 10.5 for 30 min and then was stored in 0.1 N NaOH.

Ultrafiltration experiments were also performed using MicroKros® hollow fiber modules with 30 kDa modified polyethersulfone (mPES) membranes. The hollow fibers have an inner diameter of 500 μm and are available with fiber lengths of 20, 40, and 65 cm, corresponding to membrane areas of 20, 40, and 60 cm^2, respectively, for the modules with 6 fibers (Spectrum Labs, C02-E030-05-N). Hollow fiber modules were mounted vertically and prepared following the procedures provided by Spectrum Labs.

This involved initially flushing with 200 mL of DI water at 5 psi, rinsing with a solution of 50% isopropanol at 3-4 psi for an hour, and flushing with an additional 500 mL of DI water at 5 psi. The membrane hydraulic permeability was then measured using DI water; modules were only used if the permeability was at least 20 $L/m^2/hr/psi$). The module was then flushed with 100 mL of the specific buffer to be used in the protein ultrafiltration. Modules were cleaned by recirculating a solution of 0.5 N NaOH for 1 hour and then stored in DI water at 4°C between experiments.

The same experimental set up was used for the Pellicon 3 and hollow fiber modules as shown schematically in Figure 3.7. The feed was driven through the module using a positive displacement pump (Masterflex, Gelsenkirchen, Germany). The membrane hydraulic permeability was evaluated from data obtained for the filtrate flux over a range of transmembrane pressure using DI water. The feed reservoir was then filled with the antibody solution. The transmembrane pressure was set by adjusting a valve on the retentate exit line, with the permeate flow rate evaluated via timed collection of permeate samples obtained throughout the ultrafiltration. Experiments were performed in a batch concentration mode at constant transmembrane pressure (by adjusting the pinch valve on the retentate exit line), with the retentate recycled back to the feed reservoir while permeate was removed. This allowed data to be obtained over a range of antibody concentrations in a single experimental run. Permeate and feed samples were taken periodically for off-line analysis of the antibody concentration.

8.3 Results and Analysis

8.3.1 Batch Ultrafiltration

In order to effectively evaluate the effects of the bulk protein concentration on the filtrate flux, while also providing an accurate small-scale model of commercial ultrafiltration processes, all experiments were performed in batch ultrafiltration mode with the filtrate flux and antibody concentration evaluated as a function of time as the filtrate was removed and the feed was concentrated. Typical experimental data are shown in Figure 8.1 for ultrafiltration of the monoclonal antibody solution in a 5 mM acetate buffer at pH 5 with 20 mM NaCl in a Pellicon 3 module with C screen. The initial feed had an antibody concentration of 25 g/L. The average transmembrane pressure was kept constant during the ultrafiltration at a value of approximately 105 kPa = 15 psi by adjusting the retentate valve (partially opening). This was not possible at very high bulk protein concentrations (> 170 g/L for this run) since it would have required a negative exit transmembrane pressure. Instead, data at the highest protein concentrations were obtained with the retentate valve fully open (i.e., with the exit retentate pressure approximately equal to the filtrate pressure), with the mean transmembrane pressure increasing with increasing feed concentration under these conditions.

The filtrate flux decreased with time during the ultrafiltration process due to the corresponding increase in the bulk protein concentration. For example, within the first 20 min of the batch ultrafiltration process the filtrate flux decreased from 13.9 to 8.5 μm/s (around 40%) while the feed concentration increased from 20 to 50 g/L. This was not due to any time-dependent fouling. Limited experiments performed using total recycle, i.e.,

with constant bulk protein concentration, gave filtrate flux values that were essentially independent of time (variations of less than 5%) over 10 min of ultrafiltration.

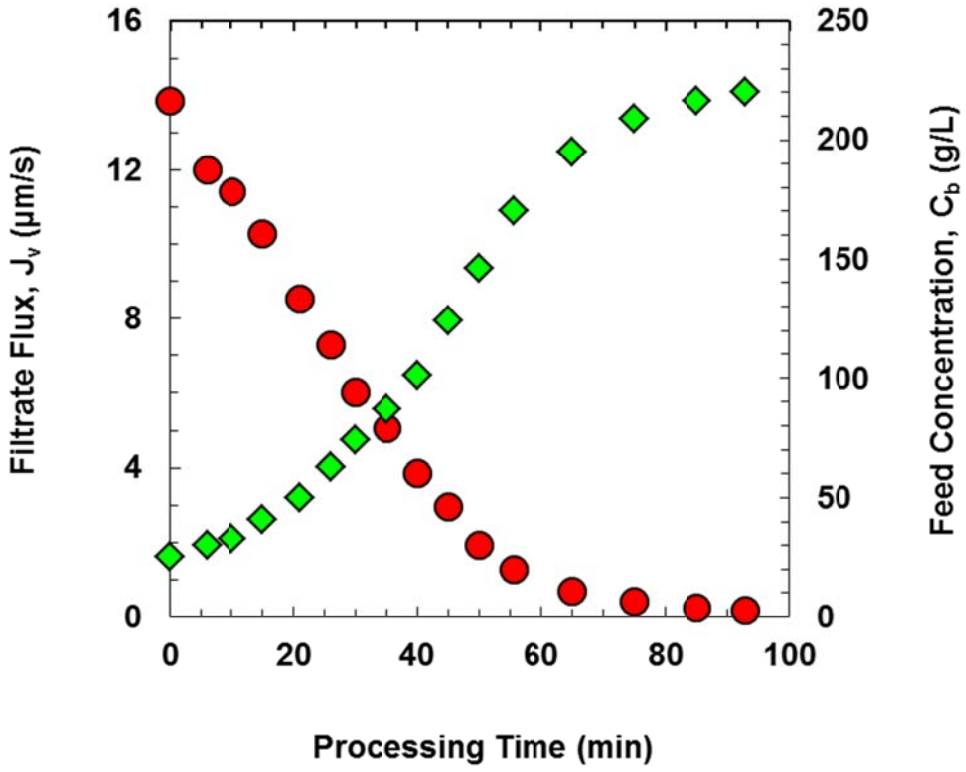

Figure 8.1. Filtrate flux and bulk protein concentration as a function of time during batch ultrafiltration of the monoclonal antibody solution in a 5 mM acetate buffer at pH 5 with 20 mM NaCl using the Pellicon 3 TFF module with C screen.

8.3.2 Screen Effects in Pellicon 3 Cassettes

The experimental data in Figure 8.1 have been re-plotted in Figure 8.2 as an explicit function of the bulk antibody concentration. The flux decreases with increasing antibody concentration, with the data being nearly linear on the semi-log plot (consistent

with the form of the simple concentration polarization model). The solid curve represents the model calculations as discussed in Chapter 7.

Also shown for comparison are results obtained in a Pellicon 3 module with a different internal screen. As mentioned earlier, tangential flow filtration cassettes have internal screens to provide mixing and increased mass transport [141, 142]. However, the screen also increases the parasitic pressure losses within the module, which can be critically important for highly viscous solutions. Two versions of the Pellicon 3 module are available commercially: the D screen module is specifically marketed "to be optimized for applications that require higher viscosity and concentration" [143]. The data in Figure 8.2 were obtained using the same monoclonal antibody solution (pH 5 acetate buffer with 20 mM NaCl) at the same feed flow rate of 45 mL/min; the only difference in the experiments is the internal screen within the Pellicon 3 modules.

Somewhat surprisingly, the filtrate flux is slightly higher in the D screen module, even though the spacer in this module should provide less internal mixing (due to more open structure). The solid curves in Figure 8.2 are model calculations using the modified polarization model with k_o = 1.9 μm/s for the D screen and 1.6 μm/s for the C screen; all other model parameters (e.g., b, B_2, B_3, and C_w) are the same for the two modules and are the same as what discussed in Chapter 7. The model calculations are in good agreement with the experimental data, although the origin of the greater value of k_o in the D screen module is unclear.

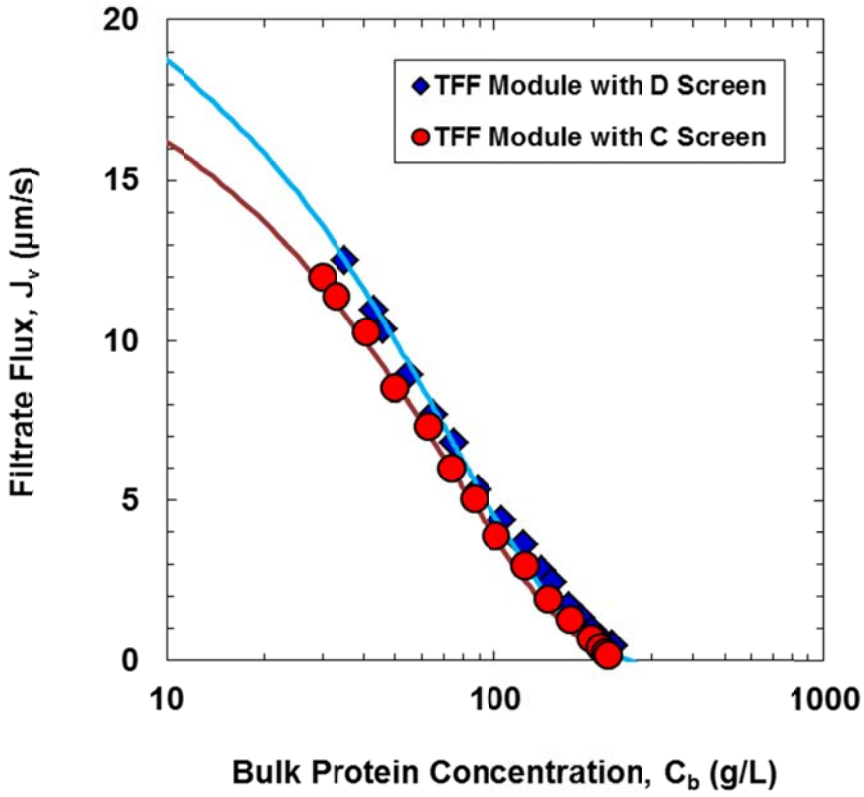

Figure 8.2. Filtrate flux as a function of the bulk protein concentration during batch ultrafiltration in the C and D screen modules. Data obtained with a 5 mM acetate buffer with 20 mM NaCl at a feed flow rate of 45 mL/min. Solid curves are model calculations using modified polarization model.

The D screen module also has a higher value for the maximum achievable protein concentration (255 g/L versus 225 g/L in the C screen module), consistent with the reduction in the pressure drop. The effect of the screen on the module pressure drop is shown in Figure 8.3. The pressure drop in the D screen module is around 30% smaller than the values in the C screen module over the full concentration range. The solid curves in Figure 8.3 are the model calculations developed using Equation 7.8 with $a = 2.5$ for the C screen module and $a = 1.9$ for the D screen module.

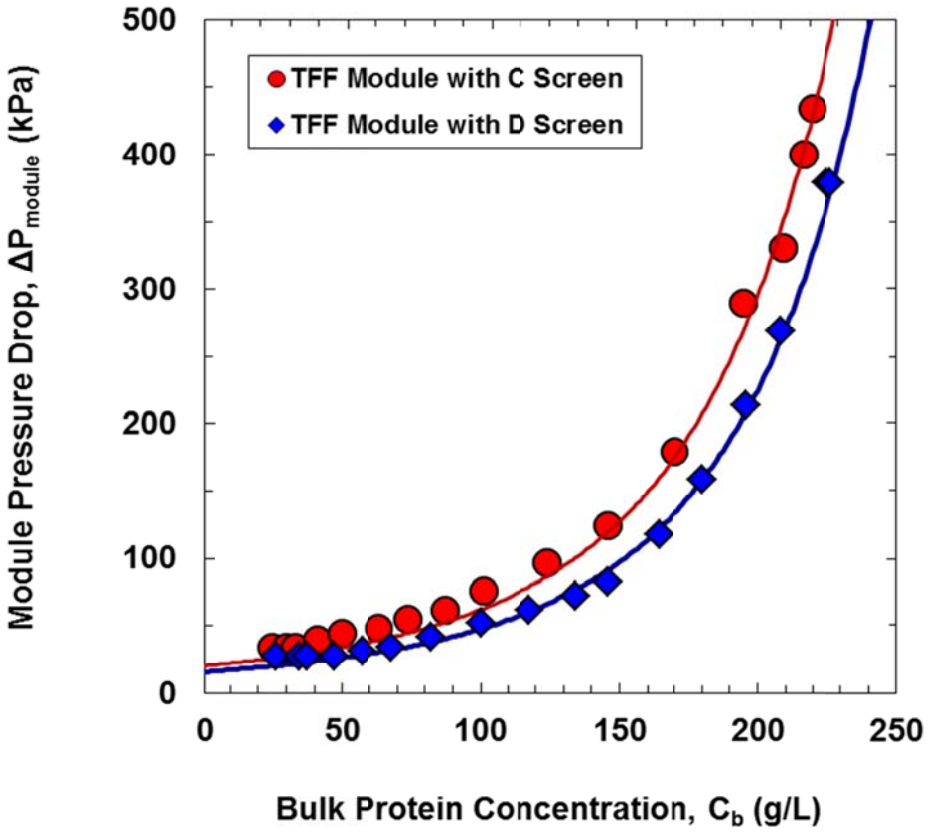

Figure 8.3. Module pressure drop for the C-screen and D-screen Pellicon 3 cassettes during batch antibody ultrafiltration. Data obtained with a 5 mM acetate buffer at pH 5 with 20 mM NaCl, using a feed flow rate of 45 mL/min. Solid curves given by Equation (7.8) using a=2.5 for C screen and a=1.9 for D screen.

8.3.3 Hollow Fiber Modules

Although antibody ultrafiltration is typically performed in screened cassettes, several companies do make hollow fiber ultrafiltration modules for antibody formulation. These hollow fiber modules are much lower cost than a TFF cassette, they can be cleaned by backflushing, and the absence of an internal screen leads to lower parasitic pressure

losses. Figure 8.4 shows a comparison of the filtrate flux data with a 20 cm long hollow fiber module with that of the C and D screen cassettes. The feed flow rate in the hollow fiber module was chosen to provide the same linear velocity as in the Pellicon 3 module channel ($Q/N\pi r^2 = Q/\varepsilon_0 wh$ = 0.20 m/s where r is the radius of the fiber lumen and N is the number of fibers and ε_0 = 0.7 is the void volume in the C screen cassette with w = 2.2 cm and h = 240 μm).

The filtrate flux in the hollow fiber module is much smaller than that in the Pellicon 3 cassettes at low antibody concentrations due to the absence of any mixing in the hollow fiber module (compared to that in the screened channels). The best fit value of k_0 for the hollow fiber module was only 0.59 μm/s, which is almost a factor of three smaller than that for both Pellicon 3 modules. However, the opposite behavior was observed at very high protein concentrations, with the maximum achievable antibody concentration in the hollow fiber module (C_{max} = 300 g/L) being significantly greater than that obtained with either the C screen or D screen modules. The solid curves in Figure 8.4 are the model calculations using the same values for b, B_2, B_3, and C_w in all three modules and are the same as what discussed in Chapter 7. The only difference in the calculations are the values of k_o and the evaluation of the pressure drop through the module, which was done using Equation (7.8) for the screened cassettes and the Hagen-Poiseuille equation for the hollow fiber module:

$$\Delta P = \frac{128 Q \eta L}{\pi N d^4} \tag{8.1}$$

where d is the diameter of the fiber lumen, N is the number of fibers, Q is the feed flowrate, L is the length of the module channel, and η is the solution viscosity. Equation

8.1 is missing the correction factor (as shown in Equation 7.8) since there is no screen in the hollow fiber module. The model calculations are in very good agreement with the data in both the screened and hollow fiber modules over the full range of antibody concentrations, properly capturing the differences in both the slope and the maximum achievable antibody concentration.

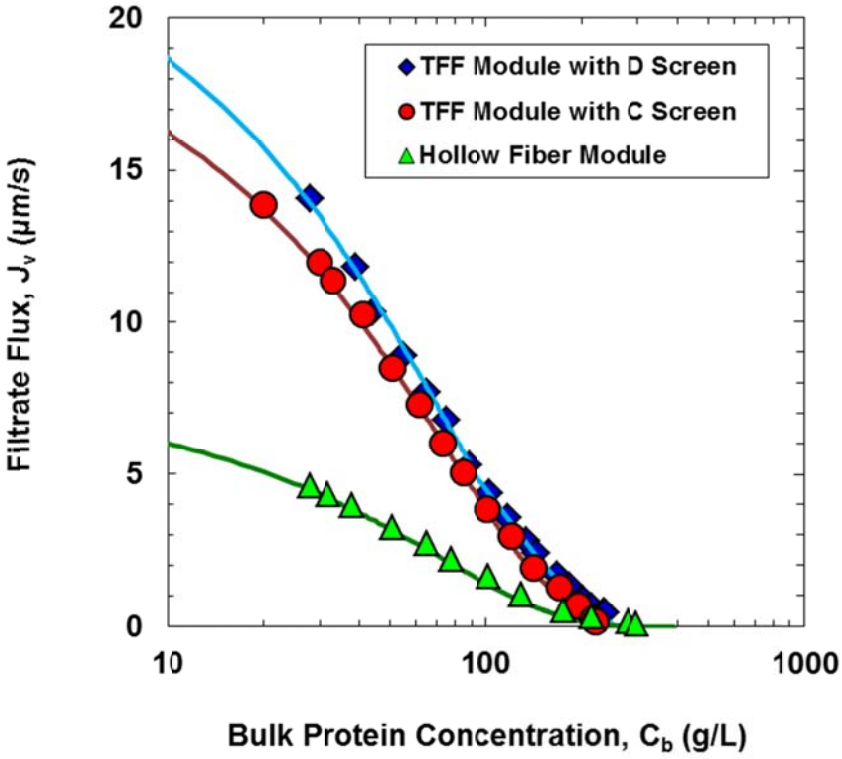

Figure 8.4. Filtrate flux in the hollow fiber module compared to that in the screened Pellicon 3 modules. Data obtained using a 5 mM acetate buffer with 20 mM NaCl. Solid curves are calculations using the modified polarization model with back-filtration

This increase in flux at high bulk protein concentrations is a direct result of the smaller pressure drop in the hollow fiber module as shown in Figure 8.5; the pressure drop in the hollow fiber module at an antibody concentration of 200 g/L was less than 100 kPa compared to values of 202 and 300 kPa in the D and C screen modules, respectively. This lower pressure drop significantly reduces the effects of back-filtration, allowing the maximum achievable protein concentration to more closely approach the C_w value for ultrafiltration in the hollow fiber module. The solid curves are model calculations given by Equations (7.8) and (8.1) for the screened and hollow fiber modules, respectively, using the same expression for the viscosity of the antibody solutions.

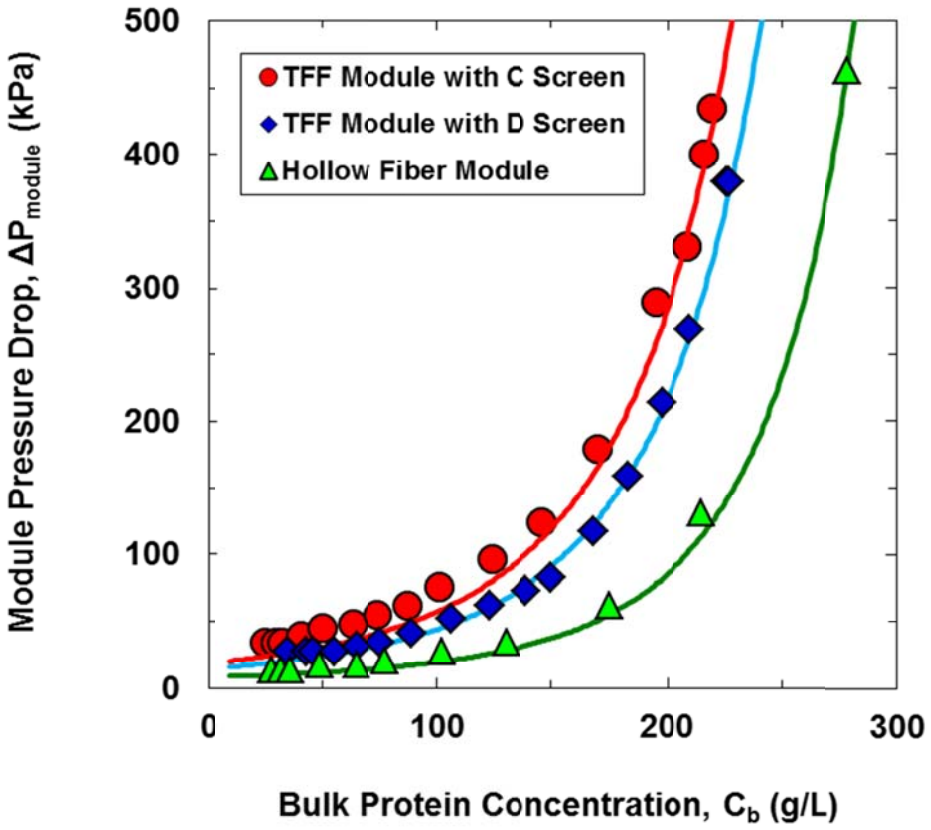

Figure 8.5. Module pressure drop during batch antibody ultrafiltration for the 20 cm hollow fiber module compared to screened Pellicon 3 cassettes. Data obtained with a 5 mM acetate buffer at pH 5 with 20 mM NaCl. Solid curves given by Equation (7.8) for the screened modules using a=2.5 for C screen and a=1.9 for D screen and using Equation (8.1) for the hollow fiber module.

In contrast to screened cassettes, which are only available with a fixed geometry (scale-up occurs by simply increasing the channel width and / or the number of parallel channels), hollow fiber modules are available with different fiber (membrane) length. The effect of fiber length on the axial pressure drop through the hollow fiber modules is shown in Figure 8.6. All of the data were obtained at a feed flow rate of 16 mL/min, corresponding to the same axial velocity in the different modules (all of which have 6

fibers with 500 μm inner diameter). The solid curves are the model calculations given by Equation (8.1); thus, the calculated values of the axial pressure drop are determined without any fitted parameters (beyond those used to evaluate the solution viscosity in Chapter 6). The predicted pressure drops are in very good agreement with the data over the full range of antibody concentrations. The axial pressure drop in the 65 cm module is more than 3 times as large as that in the 20 cm module, becoming greater than 300 kPa at an antibody protein concentration of only 180 g/L while this large pressure drop isn't obtained in the 20 cm module until an antibody concentration well above 250 g/L.

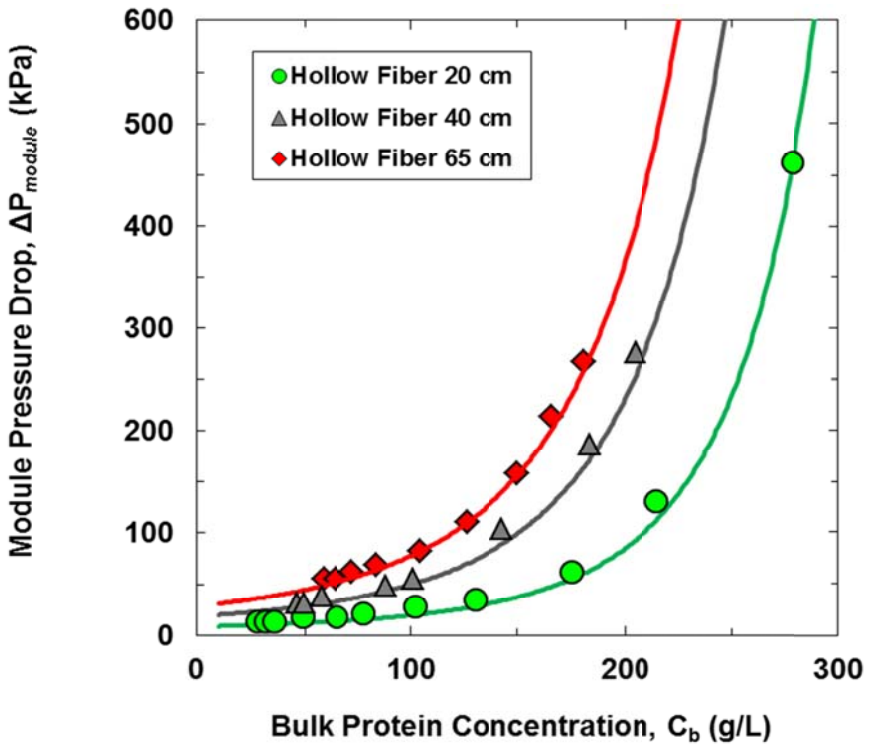

Figure 8.6. Axial pressure drop through different hollow fiber modules during batch ultrafiltration of the monoclonal antibody in a 5 mM acetate buffer with 20 mM NaCl at a feed flow rate of 16 mL/min. Solid curves are model calculations.

Figures 8.7 shows the effects of the fiber length on the filtrate flux. Model calculations were performed with the k_o values scaled as $L^{-1/3}$ based on results from the Graetz-Leveque equation [60]:

$$k = 0.538\left(\frac{D^2\gamma_w}{x}\right)^{1/3} \tag{8.2}$$

where k is the mass transfer coefficient, D is the diffusion coefficient, γ_w is the wall shear rate, and x is axial distance. The filtrate flux decreases with increasing fiber length, and the maximum achievable antibody concentration shifts to a smaller value. This latter effect is quite pronounced, with the maximum achievable wall concentration decreasing from slightly more than 300 g/L in the 20 cm fiber to around 210 g/L in the 40 cm fiber and to less than 190 g/L in the 65 cm module due to the large increase in the axial pressure drop (Figure 8.7).

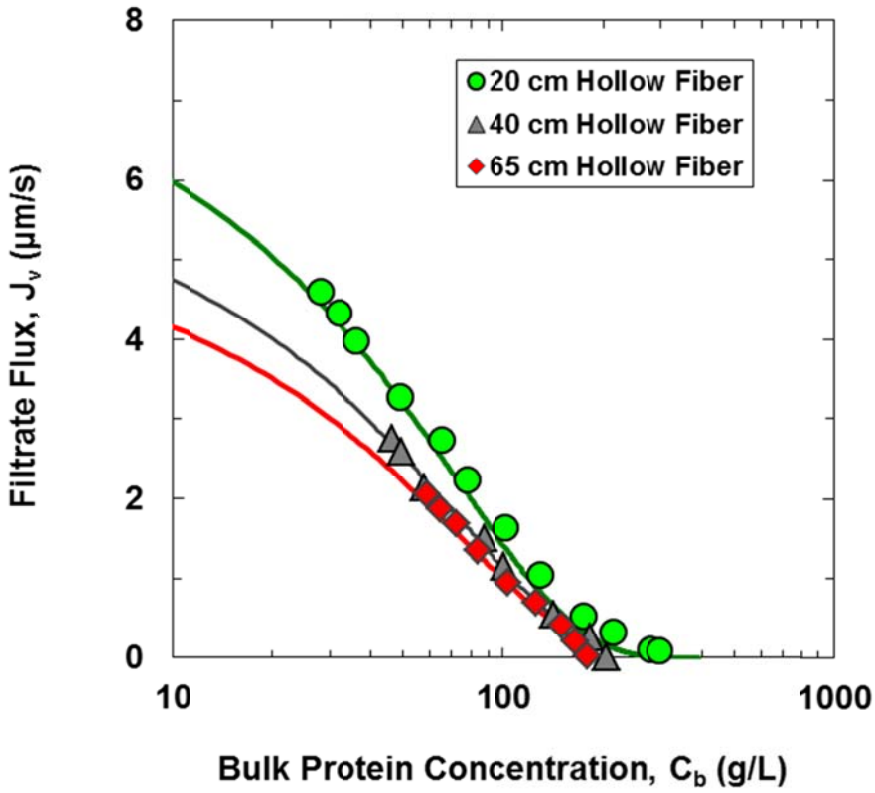

Figure 8.7. Experimental data for the filtrate flux as a function of the bulk protein concentration for the monoclonal antibody in 5 mM acetate buffer, pH 5 with 20 mM NaCl, in hollow fiber modules with different lengths and at constant average transmembrane pressure (typically around 120 kPa). Solid curves are model calculations developed using the modified polarization model accounting for back-filtration as discussed in Chapter 7.

The solid curves in Figures 8.7 are the model calculations given by the modified polarization model. All of the model parameters were identical in the different modules except for the k_o values given by Equation (8.2). The model calculations for the 40 cm and 65 cm fibers can thus be considered as predictions; the only fitted parameter in the analysis was the k_o value for the 20 cm fiber. The model predictions are in good agreement with the data for the filtrate flux, the maximum achievable concentration

8.3.4 Buffer Effects

Figure 8.9 compares experimental data for batch ultrafiltration of the monoclonal antibody at pH 5 (obtained using a 5 mM acetate buffer with 20 mM NaCl) with that at pH 6 and 7 (obtained using a 5 mM phosphate buffer with 20 mM NaCl). All experiments were performed using a Pellicon 3 module with C screen at constant average transmembrane pressure of 105 kPa (except for data at the highest bulk protein concentrations where the retentate valve was fully open).

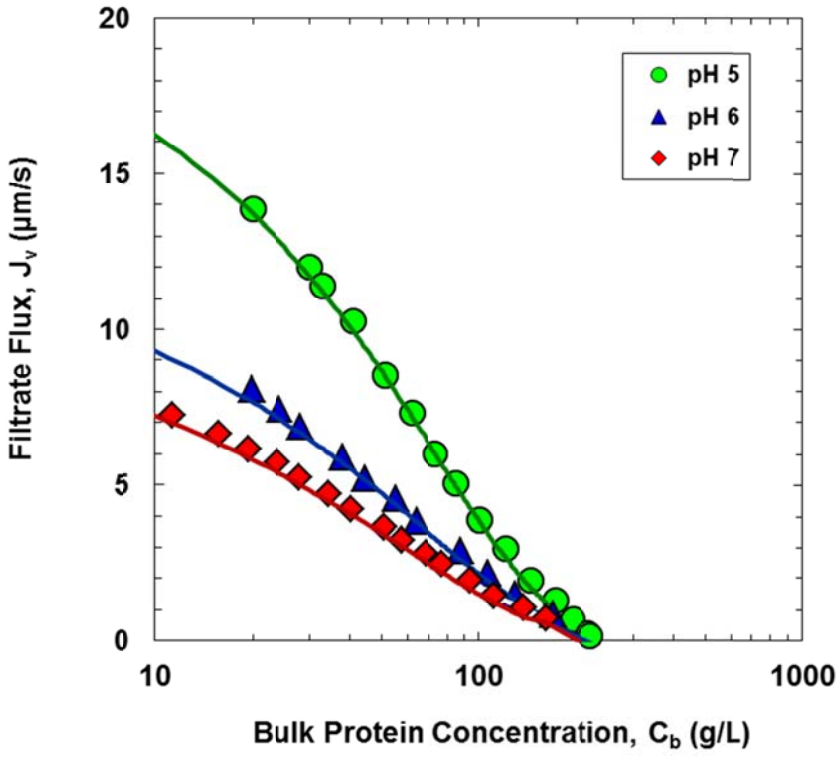

Figure 8.9. Experimental data for the filtrate flux as a function of the bulk protein concentration at pH 5, 6, and 7 during ultrafiltration of the monoclonal antibody solution through the Pellicon 3 model with C screen at a feed flow rate of 45 mL/min. Solid curves are model calculations developed using the modified polarization model accounting for back-filtration as described in Chapter 7.

The filtrate flux at any given antibody concentration decreased with increasing pH. This effect is quite dramatic in going from pH 5 to pH 6, with a much smaller reduction in flux for the data at pH 7. For example, the filtrate flux at C_b = 60 g/L decreased from 7.3 to 3.8 μm/s, i.e., by more than 50%, as the pH increased from pH 5 to pH 6. This reduction in filtrate flux occurs even though the osmotic pressure of the antibody solution is greatest at pH 5 (which would be expected to cause a lower flux due to the reduction in the effective pressure driving force as given by Equation 2.2). Instead, the reduction in filtrate flux with increasing pH is likely due to two main effects: (1) the reduction in the chemical potential gradient that drives back diffusion, and (2) the increase in solution viscosity with increasing pH (see Figure 6.3).

The solid curves in Figure 8.9 are the predicted values of the filtrate flux given by the modified concentration polarization model accounting for back-filtration developed in Chapter 7. In each case, the pressure drop due to flow through the Pellicon 3 module was calculated by integration of Equation (7.8) using the appropriate expression for the solution viscosity with a = 2.5 at all three pH. Model calculations were performed by numerical integration of Equation 7.15 using appropriate correlations for the protein osmotic pressure (Chapter 4) and solution viscosity (Chapter 6) at each pH. The wall concentration (C_w) was set to 330 g/L (identical to the value determined at pH 5 as discussed in Chapter 7) for the model calculations in the different buffer conditions due to difficulties encountered in extrapolating the osmotic pressure data up to the very high concentrations at which $\Delta\Pi_b$ = 105 kPa. Specifically, the virial expansion used to describe the osmotic pressure data was truncated after three terms (up to B_3), with the B_3 values being negative. This led to a maximum in the osmotic pressure at a bulk protein

concentration around 670 g/L at pH 6 and 330 g/L at pH 7, with the maximum value of Π being less than the mean transmembrane pressure. It is also worth mentioning that model calculations using different C_w values (in the range of 300 to 500 g/L) were practically identical showing that the choice of C_w will not dramatically influence the model predictions. The model calculations are in very good agreement with the filtrate flux data at all 3 pH using a single value of k_o = 1.6 μm/s, with all other model parameters determined from independent experimental measurements.

The effects of pH on the ultrafiltration behavior can be seen more clearly by explicitly evaluating the intermolecular interaction function, f (from Equation 7.14) for different pH values as shown in Figure 8.11. In each case the function starts at f = 1 for C_b = 0 and initially increases with increasing bulk protein concentration due to the increase in chemical potential gradient. The values of f are greatest at pH 5 due to the large osmotic pressure under these conditions arising from the strong intermolecular repulsive interactions (large positive value of B_2). The intermolecular interaction function goes through a maximum and then decays to zero at very high antibody concentrations due to the large (exponential) increase in the solution viscosity. The values of f at pH 5 drop below the values at pH 6 for antibody concentrations above 240 g/L due to the much stronger dependence of the solution viscosity on antibody concentration in the lower pH solution (larger value of b in the viscosity correlation).

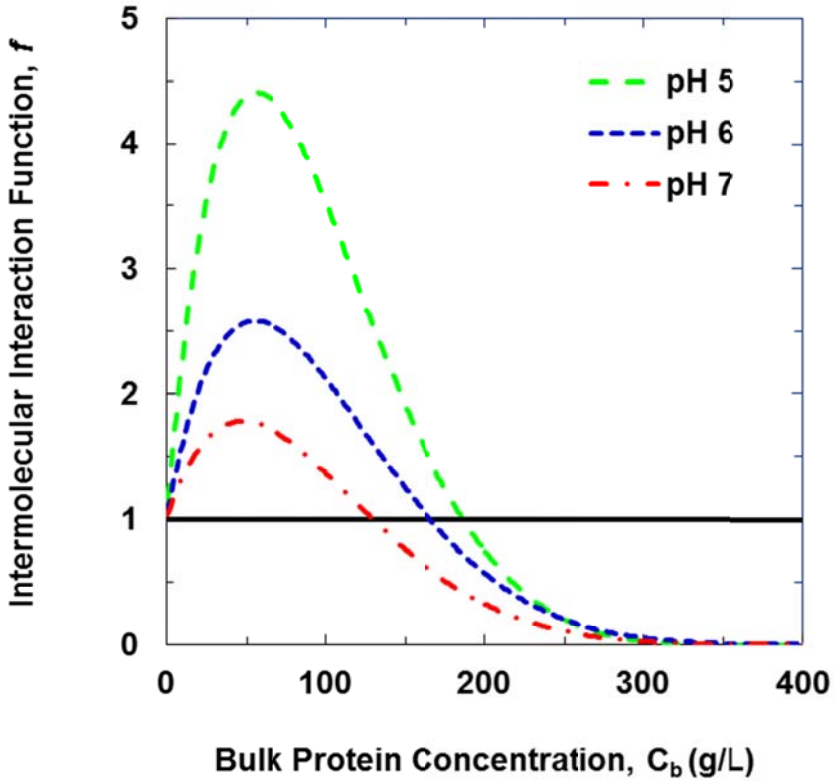

Figure 8.11. Intermolecular interaction function in Equation (7.7) as a function of bulk protein concentration for different pHs. Solid line is the stagnant film model prediction.

The effects of solution ionic strength on the filtrate flux are examined in Figure 8.11 for batch ultrafiltration experiments using a 5 mM acetate, pH 5 buffer with 10, 20, and 100 mM NaCl. Data were again obtained using the Pellicon 3 module with C screen at a feed flow rate of 45 mL/min and an average transmembrane pressure of 105 kPa. The filtrate flux and maximum achievable antibody concentration both decrease with increasing solution ionic strength, which is again opposite the behavior expected based on just the osmotic pressure (which decreases with increasing ionic strength and would thus be expected to increase the filtrate flux based on Equation 2.2). The solid curves in

Figure 8.12 are model calculations developed by numerical integration of the modified polarization model (Equation 7.15) using the correlations for the viscosity and osmotic pressure obtained from independent measurements (presented in Chapter 4 and 6). The model calculations are again in very good agreement with the experimental data over the full range of antibody concentrations and solution ionic strength.

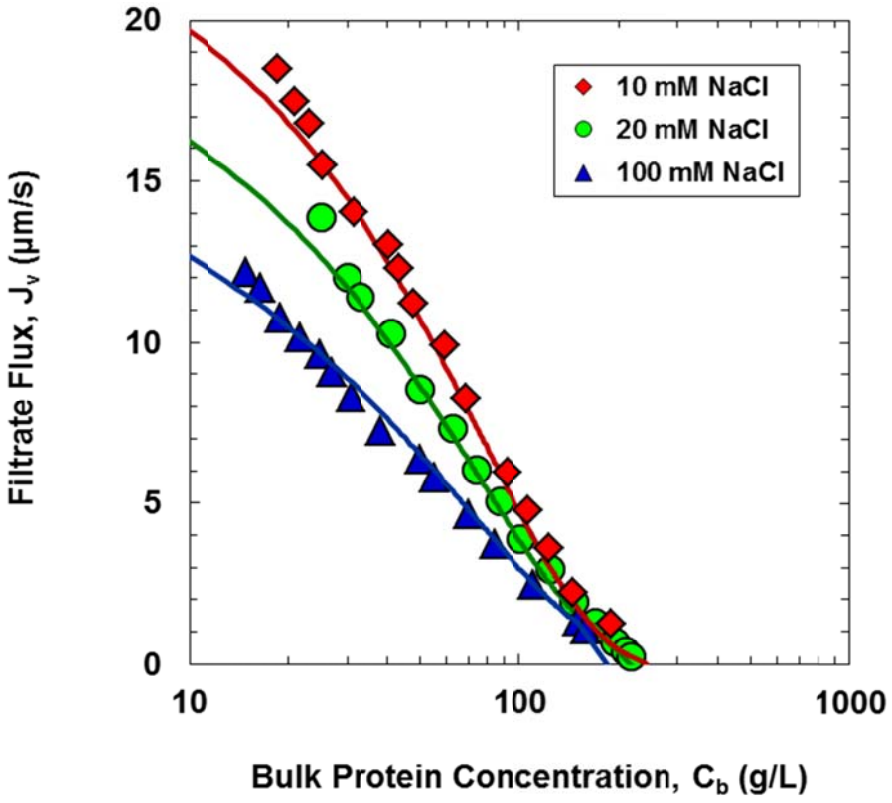

Figure 8.12. Experimental data for the filtrate flux as a function of bulk protein concentration for ultrafiltration of the monoclonal antibody in a 5 mM acetate buffer at pH 5 with 10, 20, and 100 mM NaCl. Data obtained in the Pellicon 3 module with C screen at an average transmembrane pressure of 105 kPa. Solid curves are model calculations developed using the modified polarization model accounting for back-filtration.

The reduction in the maximum achievable antibody concentration with increasing salt concentration (i.e. ionic strength) seen in Figure 8.12 is directly due to the increase in the extent of back-filtration associated with the higher viscosity under these conditions. This can be seen more clearly in Figure 8.13 which shows the pressure drop due to flow through the module as a function of the bulk antibody concentration. The pressure drop in the 10 mM NaCl solution is below 200 kPa at C_b = 180 g/L compared to a value above 300 kPa in the 100 mM NaCl at the same antibody concentration. The pressure drop in the 10 mM NaCl solution is sufficiently low that there is no back-filtration until the antibody concentration exceeds 220 g/L, leading to the larger value of the maximum achievable antibody concentration seen in Figure 8.12.

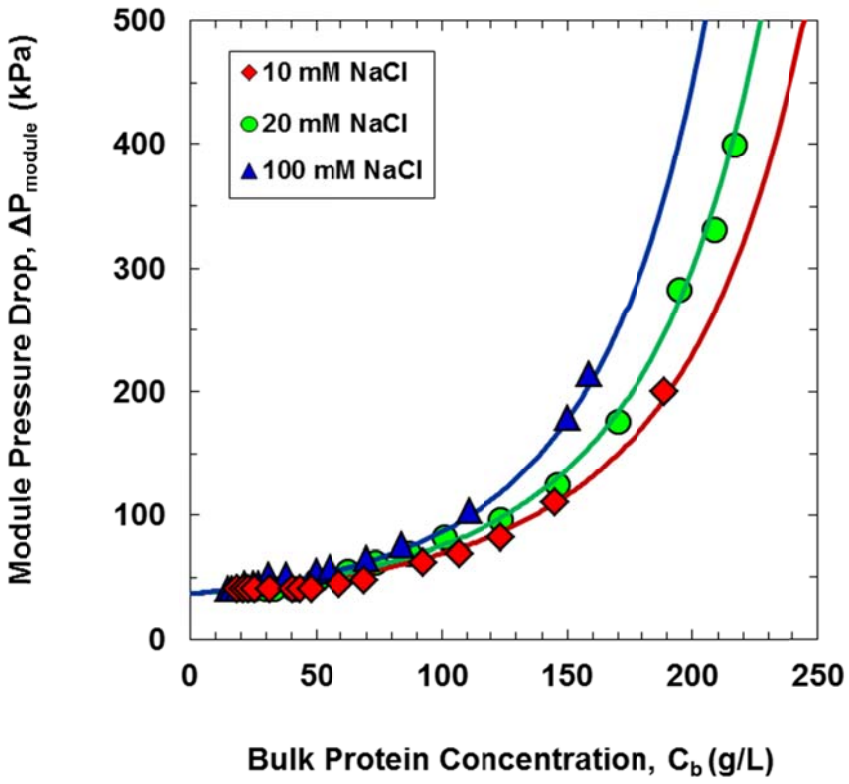

Figure 8.13. Experimental data for the pressure drop across the Pellicon 3 module as a function of the bulk protein concentration during batch ultrafiltration of the monoclonal antibody in a pH 5 acetate buffer with 10, 20, and 100 mM NaCl. Solid curves are the model calculations.

The effects of arginine-HCl, L-proline, and sucrose are shown in Figure 8.14. Although the excipients had a significant effect on the solution viscosity (and thus the pressure drop through the module), the effects on the filtrate flux were relatively small. At low bulk protein concentrations, the filtrate flux is lower in the presence of the excipients due largely to the small increase in the solution viscosity (due to the increase in η_o). The behavior at high protein concentrations is more complex – the viscosity is lower in the presence of the excipients, but this is balanced by the reduction in the chemical potential gradient (virial coefficients), which reduces the driving force for back

diffusion. The net result is that the filtrate flux and maximum achievable antibody concentration are very similar in the presence / absence of the different excipients. The solid curves in Figure 8.14 are the model calculations using the correlations for viscosity and osmotic pressure data obtained from independent measurements discussed in Chapters 4 and 6. The model is in good agreement with the experimental results for all 3 excipients.

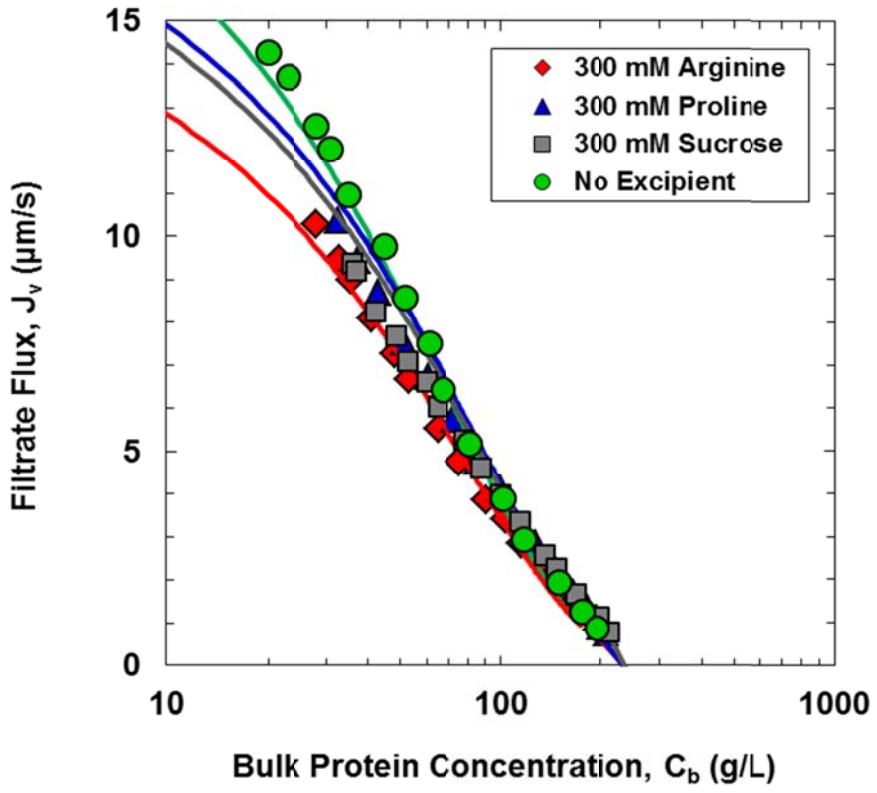

Figure 8.14. Experimental data for the filtrate flux as a function of the bulk protein concentration for the monoclonal antibody solution in the presence of different excipients. Data obtained at a feed flow rate of 45 mL/min in the Pellicon 3 module with C screen at an average transmembrane pressure of 105 kPa. Solid curves are model calculations developed using the modified polarization model accounting for back-filtration.

8.3 Conclusions

The data presented in this Chapter provide an extensive experimental investigation of the effects of solution conditions and module design on the ultrafiltration behavior of monoclonal antibodies, including results at the very high antibody concentrations required in current formulations. The filtrate flux was greater in the Pellicon 3 module with the more "open" D screen, which is specifically designed to handle more viscous solutions. The smaller pressure drop in the D screen module did reduce the extent of back-filtration, thereby increasing the maximum achievable antibody concentration. The D screen module also provided greater flux at low antibody concentrations, suggesting a larger value for the intrinsic mass transfer coefficient. The origin of this behavior is unclear; the more open D screen would have been expected to provide less mixing and thus a smaller value of the mass transfer coefficient.

The effects of back-filtration on the filtrate flux were very clearly seen in data obtained with a series of hollow fiber modules with different fiber length. Increasing the fiber length from 20 to 65 cm caused a large increase in the axial pressure drop due to flow through the module, increasing the amount of back-filtration and reducing the maximum achievable antibody concentration from more than 300 g/L to less than 190 g/L. The use of even shorter membrane modules would allow one to obtain even higher final formulation concentrations, although it would be difficult to achieve the required membrane area for large-scale commercial processes using such devices.

Decreasing solution pH or salt concentration both cause an increase in the osmotic pressure of the antibody solution, but this actually leads to an increase in the filtrate flux

due to the increase in the gradient in the chemical potential (i.e., the driving force for diffusion) and the reduction in solution viscosity (i.e., the resistance to protein motion). The decrease in solution viscosity with decreasing pH also leads to a reduction in back-filtration, increasing the maximum achievable antibody concentration at low pH and low ionic strength. The effect of excipients on ultrafiltration behavior was more complicated due to the combined changes in osmotic pressure, virial coefficients, and viscosity, although the net effect on the filtrate flux was relatively small under the conditions examined in this work.

The results presented in this chapter provide important insights into the key factors that determine the ultrafiltration behavior of highly concentrated monoclonal antibody solutions, including both the bulk mass transfer rate and the extent of back-filtration. The results and model calculations provide a framework for the development of new processes and / or modules to enhance the performance of ultrafiltration systems for the formulation of monoclonal antibodies and other important therapeutics in the biotechnology industry.

Chapter 9

Conclusions and Recommendations for Future Work

9.1 Introduction

The growing interest in the production of monoclonal antibody therapeutics and their need to be administered at high doses requires the use of highly concentrated final formulations. The current target for monoclonal antibody products is around 150 g/L; even higher concentrations must be achieved in ultrafiltration systems to accommodate the small dilution that occurs when product is recovered from the ultrafiltration module [17]. There are significant challenges in developing ultrafiltration systems to achieve the very high concentrations that will likely be required for future monoclonal antibody formulations [17].

The overall objective of this thesis was to provide a fundamental understanding of the key physical phenomena that control the filtrate flux during ultrafiltration of highly concentrated monoclonal antibody solutions with the goal of developing a theoretical framework that can predict the ultrafiltration behavior over the entire concentration range of interest. The next few subsections summarize some of the key experimental and

theoretical findings from these studies along with recommendations for future work in this area.

9.2 Osmotic Pressure of Highly Concentrated Monoclonal Antibody Solutions

The osmotic pressure of the highly concentrated antibody solutions that are formed at the membrane surface during ultrafiltration can severely limit the filtrate flux by reducing the effective pressure driving force. In addition, osmotic pressure data provide a very attractive approach for evaluating the virial coefficients in a polynomial expansion that describes the thermodynamics of these concentrated protein solutions.

Osmotic pressure data were obtained over a much wider range of protein concentrations and solution conditions than has previously been reported using a highly purified monoclonal antibody (provided by Amgen). The osmotic pressures at typical formulation conditions (e.g., pH 5 and 10 mM ionic strength) are substantially larger than those reported previously at higher pH and high ionic strength (Chapter 4). For example, the osmotic pressure at pH 5 and 10 mM ionic strength for a 230 g/L of the antibody was 45 kPa compared to a value of only 6.9 kPa from Yousef et al. [98] for serum IgG at a similar concentration but at pH 7.4 and 130 mM NaCl. These differences are likely due to a combination of the differences between serum IgG, a mixture of thousands of different antibodies have very different surface charge characteristics, and the monoclonal antibody examined in this work along with the strong electrostatic repulsion

that occurs at both low pH (away from the protein isoelectric point) and low ionic strength.

The osmotic pressure data were used to calculate the second and third virial coefficients after subtracting off the Donnan contribution arising from the unequal partitioning of the salt between the two sides of the membrane caused by the charged protein. The second virial coefficients determined from the osmotic pressure data were in relatively good agreement with independent measurements using a modified self-interaction chromatography method developed as part of this thesis to provide a more accurate estimate of the B_2 values based on results with a non-interacting dextran (Chapter 5). Self-interaction chromatography is a very attractive method for rapidly screening solution conditions to identify buffers / excipients with appropriate properties. The second virial coefficients were all positive and increased at low pH and low ionic strength due to the increase in intermolecular electrostatic repulsion. In contrast, the third virial coefficients were negative (for all buffer conditions examined in this thesis), which suggests that there are short-range attractive interactions in which local oppositely charged regions of different antibodies interact with high geometric complementarity. The data presented in this thesis provide the first extensive measurements of the third virial coefficient for monoclonal antibodies, providing important insights into the magnitude of these short range attractive interactions.

9.3 Rheology of Highly Concentrated Monoclonal Antibody Solutions

The rheological behavior of highly concentrated protein solutions has often been used to obtain insights into the magnitude of protein-protein interactions in these systems**.** The viscosity was therefore measured over a wide range of buffer conditions using the same antibody solutions used in the osmotic pressure experiments. The viscosity increased dramatically with increasing antibody concentration, with the data well-described using the semi-empirical model developed by Ross and Minton [135].

In contrast to the osmotic pressure, the viscosity decreased with decreasing pH (over the range from pH 5 to 7) and with decreasing salt concentration (at pH 5), conditions that would be expected to lead to greater intermolecular electrostatic repulsion between the proteins. The magnitude of the viscosity coefficient *b* was found to be well-correlated with the third osmotic virial coefficient, suggesting that the concentration dependence of the antibody viscosity is governed primarily by short-range attractive interactions, consistent with results in previous studies. The results presented in Chapter 6 provide the first evidence for a relationship between the viscosity of highly concentrated protein solutions and the magnitude of the third osmotic virial coefficient (due largely to the lack of available literature data for the third virial coefficient).

The addition of excipients such as proline, arginine, and sucrose had a complex effect on the solution viscosity. The excipients increased the viscosity of the fluid phase, leading to an increase in the viscosity of the antibody solution at low protein concentrations. However, the excipients dramatically altered the extent of intermolecular interactions, leading to a significant reduction in the viscosity at high antibody

concentrations (consistent with previous reports in the literature). This behavior could not be explained by changes in the osmotic virial coefficients; additional studies will be required to determine the underlying physical phenomena controlling the rheological behavior in the presence of different excipients.

9.4 Ultrafiltration Behavior

The ultrafiltration behavior of the monoclonal antibody was determined by the properties of the buffer solution (pH, ionic strength, and excipients), the design of the membrane module (spacer properties, fiber length), and the device operating conditions (feed flow rate and antibody concentration). The data obtained in this thesis provide the most extensive study of the filtrate flux during ultrafiltration of a highly purified monoclonal antibody, with a particular focus on the behavior at very high protein concentrations, approaching the concentration at which the filtrate flux decays to zero, which defines the maximum achievable protein concentration for the ultrafiltration system.

The filtrate flux was greatest at low pH and in low ionic strength solutions, in screened modules, and in short hollow fibers, consistent with previous experimental studies. More interestingly, the maximum achievable antibody concentration increased with decreasing fiber length and decreasing feed flow rate, and it was significantly greater in a 20 cm long hollow fiber module than in a screened cassette with similar length. This increase in the maximum achievable protein concentration was a direct result of the reduction in the pressure drop associated with flow through the module.

The filtrate flux data were analyzed using a modified concentration polarization model that includes: (1) the use of the chemical potential gradient as the appropriate driving force for back diffusion within the concentration polarization boundary layer, (2) the effects of solution viscosity on the protein mobility and in turn the protein diffusion coefficient (via the Stokes-Einstein equation), (3) the effect of the solution viscosity on the boundary layer thickness and in turn the mass transfer coefficient, and (4) the contribution of back-filtration when the local transmembrane pressure drops below the osmotic pressure difference across the membrane. Model calculations were in good agreement with experimental data for the filtrate flux, properly describing the complex variation of the slope, $dJ_v/d(\ln C_b)$, as a function of the bulk protein concentration. In addition, the model was able to accurately predict the increase in maximum achievable antibody concentration with decreasing feed flow rate and decreasing fiber length, which in both cases arises from the reduction in the extent of back-filtration due to the decrease in pressure drop caused by the feed flow through the module. This is the first published model to explicitly account for this back-filtration phenomenon during protein ultrafiltration.

9.5 Recommendations

The results presented in this thesis provide important insights into the key physical phenomena governing the ultrafiltration behavior of highly concentrated protein solutions. However, there are a number of important areas which would benefit from additional experimental and theoretical investigations.

First, all of the experimental data presented in this thesis were obtained using a single model monoclonal antibody provided by Amgen. It would be very desirable to extend this work to study the physical properties (osmotic pressure, virial coefficients, and viscosity) and ultrafiltration behavior of other monoclonal antibodies to determine the generalizability of the results obtained in this work. These studies could also shed light on the role of the antibody properties, e.g., the isoelectric point and net protein charge, on both the physical properties and ultrafiltration behavior of highly concentrated monoclonal antibody solutions. These data could be invaluable in developing initial estimates of antibody properties and in obtaining early identification of antibody molecules that may create unique challenges for downstream processing and final formulation.

It would also be highly desirable to extend the osmotic pressure measurements up to even higher antibody concentrations. This would provide more accurate values of the second and third virial coefficients, and it might even be possible to obtain initial estimates for the fourth virial coefficient. In addition, osmotic pressure data at higher protein concentrations would make it possible to more accurately estimate the wall concentration, which is determined by the equality between the applied transmembrane pressure and the osmotic pressure difference across the membrane. As mentioned previously, all of the third virial coefficients obtained in this work were negative, which corresponds to attractive short range electrostatic interactions even at buffer conditions where we would have anticipated strong electrostatic repulsion (as seen in the large positive values of B_2). Future studies with other monoclonal antibodies / proteins will

help better understand these short range electrostatic interactions and their effects on solution physiochemical properties.

The results presented in this thesis are the first experimental data to show the direct correlation between solution viscosity and short range electrostatic interactions which are estimated using third virial coefficients. It would be very interesting to confirm this direct correlation by conducting the viscosity and third virial coefficient measurements using other monoclonal antibodies. Such investigation would also help to better understand the effect of antibody properties on third virial coefficient and solution viscosity and to further determine the key structural properties controlling the rheological behavior of monoclonal antibody solutions.

Although the experimental results presented in Chapter 7 provide important insights into the ultrafiltration behavior of highly concentrated antibody solutions, it was difficult to accurately evaluate the slope values by numerical differentiation of the filtrate flux data due to the limited number of data points. Thus, it would be very useful to perform ultrafiltration experiments over a broader range of concentrations, with a particular focus on the behavior at low to moderate concentrations (e.g., from 1- 50 g/L) and at very high concentrations (e.g., from 150 – 250 g/L). Data points should be taken at short time intervals to minimize the potential errors in evaluating the slope by numerical differentiation. These data would provide important insights into the behavior of the slope plot over the full concentration range, including the local maximum around 50 g/L and the local minimum around 170 g/L.

The experimental studies described in this thesis focused on bulk mass transport within the concentration polarization boundary layer in the pressure-independent regime.

However, there are a number of other phenomena which can be important in ultrafiltration processes. In particular, future studies should examine membrane fouling during ultrafiltration of highly concentrated monoclonal antibody solutions, including the effects of device operating conditions and membrane properties (e.g., regenerated cellulose versus polyethersulfone versus novel electrically-charged membranes that have been shown to have very low fouling behavior). These studies should also provide a more detailed analysis of protein retention – the 30 kDa Ultracel membranes used in the current work were highly retentive to the monoclonal antibody (>99.5%), but even this small degree of protein leakage can become problematic in diafiltration (buffer exchange) due to the large volumes of filtrate that must be processed. It would also be interesting to examine the performance of the ultrafiltration systems at lower transmembrane pressures which are of interest in applications of high performance tangential flow filtration [33].

It would also be very interesting to extend the experimental studies to consider a much wider range of excipients used in the biotechnology industry to improve protein stability. This would include other sugars (like trehalose), sugar alcohols (like mannitol), and surfactants (like Polysorbate 80). Experimental studies should focus on the effects of these excipients on both the underlying physical properties of the monoclonal antibody (e.g., osmotic pressure, virial coefficients, and solution viscosity) as well as the ultrafiltration flux. The goal of these studies would be to identify excipients that can significantly improve the ultrafiltration behavior, e.g., by reducing the solution viscosity to a degree that eliminates back-filtration so that much higher antibody concentrations can be achieved during ultrafiltration.

The model calculations presented in Chapter 7 clearly indicate that the use of very short ultrafiltration modules would reduce the extent of back-filtration by reducing the pressure drop associated with feed flow through the module. It would be very interesting to confirm this experimentally by using modules with much shorter path length than current commercial modules (which are all on the order of 20 cm or more in length). This could be done using hollow fiber modules in which the individual fibers are potted by hand in custom cartridges or in small "plate-and-frame" modules with very short path length. It would also be very interesting to examine the behavior of non-traditional modules that operate without any significant pressure losses, e.g., the rotating cylinder (Couette) flow modules or the rotating disk modules (sold commercially under the tradename VSep).

A number of other approaches could also be examined to reduce the extent of back-filtration and thus increase the maximum achievable protein concentration. For example, the data obtained in Chapter 7 show that the use of low feed flow rates reduces back-filtration, although this also reduces the mass transfer coefficient and thus the filtrate flux. It might be possible to design an ultrafiltration process in which the feed flow rate changes during the process to maximize the flux (for more dilute solutions) while minimizing back-filtration (for more concentrated solutions).

Another approach for reducing back-filtration would be to use a co-flow configuration in which some of the filtrate is recirculated on the permeate-side of the membrane to generate a pressure drop that approximately balances the pressure losses in the feed channel. The magnitude of the recirculation flow would need to increase with increasing feed concentration to accommodate the increase in solution viscosity. The net

result would be a nearly uniform transmembrane pressure throughout the membrane module, with no back-filtration even at high feed concentrations.

Another approach that might be worth considering would be to use a two-step process in which the protein solution is first concentrated in a screened module (up to close to the maximum achievable concentration) and then transferred to a hollow fiber module to achieve the final desired concentration. This would take advantage of the high mass transfer coefficients (and thus high filtrate flux) in the screened channel with the very high formulation concentration achieved in the hollow fiber module due to its much lower axial pressure drop.

References

[1] D. Dimitrov, Therapeutic proteins, in: V. Voynov, J.A. Caravella (Eds.) Therapeutic Proteins, Humana Press, 2012, pp. 1-26.

[2] P.J. Carter, Introduction to current and future protein therapeutics: A protein engineering perspective, Experimental Cell Research, 317 (2011) 1261-1269.

[3] A.L. Zydney, Membrane technology for purification of therapeutic proteins, Biotechnology and Bioengineering, 103 (2009) 227-230.

[4] J.M. Reichert, C.J. Rosensweig, L.B. Faden, M.C. Dewitz, Monoclonal antibody successes in the clinic, Nat Biotech, 23 (2005) 1073-1078.

[5] J.M. Reichert, V.E. Valge-Archer, Development trends for monoclonal antibody cancer therapeutics, Nat Rev Drug Discov, 6 (2007) 349-356.

[6] J.M. Reichert, Monoclonal antibodies in drug and vaccine development, Drug Discovery Today (2013).

[7] H. Ledford, Monoclonal antibodies come of age, Nature, 455 (2008) 437.

[8] J.M. Reichert, Antibodies to watch in 2014, mAbs, 6 (2014) 5-14.

[9] J.M. Reichert, Monoclonal antibodies as innovative therapeutics, Current Pharmaceutical Biotechnology, 9 (2008) 423-430.

[10] G. Jagschies, A. Gronberg, T. Bjorkman, K. Lacki, H.J. Johansson, Technical and economical evaluation of downstream processing options for monoclonal antibody (MAb) production, Biopharm. Int., (2006) 10-+.

[11] B. Kelley, Very large scale monoclonal antibody purification: the case for conventional unit operations, Biotechnology Progress, 23 (2007) 995-1008.

[12] D.S. Clark, H.W. Blanch, Biochemical engineering, CRC Press, 1997.

[13] A. Jungbauer, Chromatographic media for bioseparation, Journal of Chromatography A, 1065 (2005) 3-12.

[14] M.R. Ladisch, Bioseparations engineering, (2001).

[15] S.J. Shire, Z. Shahrokh, J. Liu, Challenges in the development of high protein concentration formulations, Journal of Pharmaceutical Sciences, 93 (2004) 1390-1402.

[16] E. Rosenberg, S. Hepbildikler, W. Kuhne, G. Winter, Ultrafiltration concentration of monoclonal antibody solutions: Development of an optimized method minimizing aggregation, Journal of Membrane Science, 342 (2009) 50-59.

[17] S. Rao, E. Gefroh, O. Kaltenbrunner, Recovery modeling of tangential flow systems, Biotechnology and Bioengineering, 109 (2012) 3084-3092.

[18] R.J. Harris, S.J. Shire, C. Winter, Commercial manufacturing scale formulation and analytical characterization of therapeutic recombinant antibodies, Drug Development Research, 61 (2004) 137-154.

[19] R. van Reis, A. Zydney, Bioprocess membrane technology, Journal of Membrane Science, 297 (2007) 16-50.

[20] M.R. Ladisch, K.L. Kohlmann, Recombinant human insulin, Biotechnology Progress, 8 (1992) 469-478.

[21] J.A. Howell, V. Sanchez, R.W. Field, Membranes in bioprocessing, (1993).

[22] F.V. Kosikowski, Membrane separations in food processing, Membrane separations in biotechnology, 201 (1986).

[23] J.D. Ferry, Ultrafilter membranes and ultrafiltration, Chemical Reviews, 18 (1936) 373-455.

[24] C. Ratledge, B. Kristiansen, Basic biotechnology, Cambridge University Press, 2006.

[25] A. Shrivastava, S. Kumar, E.L. Cussler, Predicting the effect of membrane spacers on mass transfer, Journal of Membrane Science, 323 (2008) 247-256.

[26] R. van Reis, A.L. Zydney, Protein ultrafiltration, in: Encyclopedia of Bioprocess Technology, John Wiley & Sons, Inc., 2002.

[27] I.H. Huisman, P. Prádanos, A. Hernández, The effect of protein–protein and protein–membrane interactions on membrane fouling in ultrafiltration, Journal of Membrane Science, 179 (2000) 79-90.

[28] G. Subramanian, Bioseparation and bioprocessing, 2nd ed., Wiley-VCH: Weinheim, Germany, 1998.

[29] Y.-H. Kao, J. Bender, A. Hagewiesche, P. Wong, Y. Huang, M. Vanderlaan, Characterization of Filter Extractables by Proton NMR Spectroscopy: Studies on

Intact Filters with Process Buffers, PDA Journal of Pharmaceutical Science and Technology, 55 (2001) 268-277.

[30] R. van Reis, E.M. Goodrich, C.L. Yson, L.N. Frautschy, S. Dzengeleski, H. Lutz, Linear scale ultrafiltration, Biotechnology and Bioengineering, 55 (1997) 737-746.

[31] V.L. Vilker, C.K. Colton, K.A. Smith, The osmotic pressure of concentrated protein solutions: Effect of concentration and ph in saline solutions of bovine serum albumin, Journal of Colloid and Interface Science, 79 (1981) 548-566.

[32] E. Binabaji, S. Rao, A.L. Zydney, The osmotic pressure of highly concentrated monoclonal antibody solutions: Effect of solution conditions, Biotechnology and Bioengineering, 111 (2014) 529-536.

[33] L.J. Zeman, A.L. Zydney, Microfiltration and ultrafiltration: principles and applications, Marcel Dekker, New York, 1996.

[34] N.S. Pujar, Electrostatic and electrokinetic interactions during protein filtration using semi-permeable membranes, in, University of Delaware, 1997.

[35] S. Saito, J. Hasegawa, N. Kobayashi, N. Kishi, S. Uchiyama, K. Fukui, Behavior of monoclonal antibodies: relation between the second virial coefficient (B 2) at low concentrations and aggregation propensity and viscosity at high concentrations, Pharm Res, 29 (2012) 397-410.

[36] S. Saksena, Protein transport in selective membrane filtration., in, University of Delaware, Newark, DE, 1995.

[37] J.R. Molek, Ultrafiltration of pegylated proteins, in, The Pennsylvania State University, 2008.

[38] M.M. Rohani, Effect of electrostatic interactions during protein ultrafiltration: Effects of ligand chemistry and protein surface charge distribution, in, The Pennsylvania State University, 2011.

[39] W.S. Opong, U.o. Delaware, Protein transport and deposition during size-selective membrane filtration, in, University of Delaware, 1991.

[40] M.K. Menon, Effects of protein charge and electrostatic interactions in ultrafiltration and size exclusion chromatography, in, University of Delaware, Newark, DE, 1999.

[41] W.S. Opong, A.L. Zydney, Effect of membrane structure and protein concentration on the osmotic reflection coefficient, Journal of membrane science, 72 (1992) 277-292.

[42] O. Kedem, A. Katchalsky, Thermodynamic analysis of the permeability of biological membranes to non-electrolytes, Biochimica et Biophysica Acta, 27 (1958) 229-246.

[43] K.S. Spiegler, O. Kedem, Thermodynamics of hyperfiltration (reverse osmosis): criteria for efficient membranes, Desalination, 1 (1966) 311-326.

[44] A. Katzir-Katchalsky, P.F. Curran, Nonequilibrium thermodynamics in biophysics, (1965).

[45] A. Staverman, The theory of measurement of osmotic pressure, Recueil des Travaux Chimiques des Pays-Bas, 70 (1951) 344-352.

[46] G.A. Denisov, Theory of concentration polarization in cross-flow ultrafiltration: gel-layer model and osmotic-pressure model, Journal of Membrane Science, 91 (1994) 173-187.

[47] W.R. Bowen, F. Jenner, Dynamic ultrafiltration model for charged colloidal dispersions: A Wigner-Seitz cell approach, Chemical Engineering Science, 50 (1995) 1707-1736.

[48] A.L. Zydney, Stagnant film model for concentration polarization in membrane systems, Journal of Membrane Science, 130 (1997) 275-281.

[49] G.B. van den Berg, C.A. Smolders, Flux decline in ultrafiltration processes, Desalination, 77 (1990) 101-133.

[50] A.A. Kozinski, E.N. Lightfoot, Ultrafiltration of proteins in stagnation flow, AIChE Journal, 17 (1971) 81-85.

[51] V.L. Vilker, C.K. Colton, K.A. Smith, D.L. Green, The osmotic pressure of concentrated protein and lipoprotein solutions and its significance to ultrafiltration, Journal of Membrane Science, 20 (1984) 63-77.

[52] B.C. Robertson, A.L. Zydney, A Stefan-Maxwell analysis of protein transport in porous membranes, Separation Science and Technology, 23 (1988) 1799-1811.

[53] B.C. Robertson, A.L. Zydney, Protein adsorption in asymmetric ultrafiltration membranes with highly constricted pores, Journal of Colloid and Interface Science, 134 (1990) 563-575.

[54] J.J.S. Shen, R.F. Probstein, On the prediction of limiting flux in laminar ultrafiltration of macromolecular solutions, Industrial & Engineering Chemistry Fundamentals, 16 (1977) 459-465.

[55] M.C. Porter, Concentration polarization with membrane ultrafiltration, Industrial & Engineering Chemistry Product Research and Development, 11 (1972) 234-248.

[56] A.S. Michaels, New separation technique for CPI, Chemical Engineering Progress, 64 (1968) 31-&.

[57] F. Kochinke, H.v. Baeyer, R. Schnabel, M. Marx, R. Mohnhaupt, M. Kessel, Formation of a" hybrid membrane" in porous glass capillaries during hemofiltration (Hf), ASAIO Journal, 28 (1982) 488-493.

[58] R.F. Probstein, W.-F. Leung, Y. Alliance, Determination of diffusivity and gel concentration in macromolecular solutions by ultrafiltration, The Journal of Physical Chemistry, 83 (1979) 1228-1232.

[59] S.-I. Nakao, T. Nomura, S. Kimura, Characteristics of macromolecular gel layer formed on ultrafiltration tubular membrane, AIChE Journal, 25 (1979) 615-622.

[60] M.D. Lévêque, Les Lois de la transmission de chaleur par convection, Ann. Mines, 13 (1928) 201.

[61] P. Aimar, R. Field, Limiting flux in membrane separations: A model based on the viscosity dependency of the mass transfer coefficient, Chemical Engineering Science, 47 (1992) 579-586.

[62] V. Gekas, B. Hallström, Mass transfer in the membrane concentration polarization layer under turbulent cross flow : I. Critical literature review and adaptation of existing Sherwood correlations to membrane operations, Journal of Membrane Science, 30 (1987) 153-170.

[63] A.L. Zydney, Concentration effects on membrane sieving: Development of a stagnant filmmodel incorporating the effects of solute-solute interactions, Journal of Membrane Science, 68 (1992) 183-190.

[64] W.R. Bowen, A. Mongruel, P.M. Williams, Prediction of the rate of cross-flow membrane ultrafiltration: A colloidal interaction approach, Chemical Engineering Science, 51 (1996) 4321-4333.

[65] S. Saksena, A.L. Zydney, Influence of protein–protein interactions on bulk mass transport during ultrafiltration, Journal of Membrane Science, 125 (1997) 93-108.

[66] P.H. Wiersema, A.L. Loeb, J.T.G. Overbeek, Calculation of the electrophoretic mobility of a spherical colloid particle, Journal of Colloid and Interface Science, 22 (1966) 78-99.

[67] M.K. Menon, A.L. Zydney, Determination of Effective Protein Charge by Capillary Electrophoresis: Effects of Charge Regulation in the Analysis of Charge Ladders, Analytical Chemistry, 72 (2000) 5714-5717.

[68] U. Sharma, R.S. Negin, J.D. Carbeck, Effects of cooperativity in proton binding on the net charge of proteins in charge ladders, The Journal of Physical Chemistry B, 107 (2003) 4653-4666.

[69] M.K. Menon, A.L. Zydney, Effect of ion binding on protein transport through ultrafiltration membranes, Biotechnology and Bioengineering, 63 (1999) 298-307.

[70] J.H. Masliyah, S. Bhattacharjee, Electrokinetic and colloid transport phenomena, John Wiley & Sons, 2006.

[71] D.C. Henry, The cataphoresis of suspended particles. part I. the equation of cataphoresis, Proceedings of the Royal Society. A, Mathematical, physical, and engineering sciences, 133 (1931) 106-129.

[72] R.J. Beynon, J.S. Easterby, Buffer solutions, 1st edition ed., Oxford University Press Inc, New York, 1996.

[73] D.B. Burns, Electrostatic interactions in protein transport using ultrafiltration membranes: effects of solution conditions and membrane charge, in, University of Delaware, Newark, DE,, 2000.

[74] J.D. Oliver, S. Anderson, J.L. Troy, B.M. Brenner, W.H. Deen, Determination of glomerular size-selectivity in the normal rat with Ficoll, Journal of the American Society of Nephrology, 3 (1992) 214-228.

[75] A. Mehta, A.L. Zydney, Permeability and selectivity analysis for ultrafiltration membranes, Journal of Membrane Science, 249 (2005) 245-249.

[76] M. Bakhshayeshirad, Performance characteristics of virus filtration membranes: Protein fouling and virus retention, in, The Pennsylvania State University, University Park, PA, 2011.

[77] S.Y. Patro, T.M. Przybycien, Self-interaction chromatography: A tool for the study of protein–protein interactions in bioprocessing environments, Biotechnology and Bioengineering, 52 (1996) 193-203.

[78] P.M. Tessier, Fundamentals and applications of nanoparticle interactions and self-assembly, in, University of Delaware, 2004.

[79] O.H. Brekke, I. Sandlie, Therapeutic antibodies for human diseases at the dawn of the twenty-first century, Nat Rev Drug Discov, 2 (2003) 52-62.

[80] S.P. Palecek, A.L. Zydney, Intermolecular electrostatic interactions and their effect on flux and protein deposition during protein filtration, Biotechnology Progress, 10 (1994) 207-213.

[81] Y. Wang, V.G.J. Rodgers, Free-solvent model shows osmotic pressure is the dominant factor in limiting flux during protein ultrafiltration, Journal of Membrane Science, 320 (2008) 335-343.

[82] H. Nishi, M. Miyajima, H. Nakagami, M. Noda, S. Uchiyama, K. Fukui, Phase Separation of an IgG1 Antibody Solution under a Low Ionic Strength Condition, Pharm Res, 27 (2010) 1348-1360.

[83] J.J. Valente, R.W. Payne, M.C. Manning, W.W. Wilson, C.S. Henry, Colloidal behavior of proteins: effects of the second virial coefficient on solubility, crystallization and aggregation of proteins in aqueous solution, Current Pharmaceutical Biotechnology, 6 (2005) 427-436.

[84] A. Ducruix, J.P. Guilloteau, M. Riès-Kautt, A. Tardieu, Protein interactions as seen by solution X-ray scattering prior to crystallogenesis, Journal of Crystal Growth, 168 (1996) 28-39.

[85] H.V. Porschel, G. Damaschun, Determination of virial-coefficient of protein solutions by means of x-ray small-angle scattering and interpretations, Studia Biophysica 62 (1977) 69-69.

[86] J. Behlke, O. Ristau, Analysis of the thermodynamic non-ideality of proteins by sedimentation equilibrium experiments, Biophysical Chemistry, 76 (1999) 13-23.

[87] M. Jiménez, G. Rivas, A.P. Minton, Quantitative characterization of weak self-association in concentrated solutions of immunoglobulin G via the measurement of sedimentation equilibrium and osmotic pressure†, Biochemistry, 46 (2007) 8373-8378.

[88] A.A. Fodeke, A.P. Minton, Quantitative characterization of polymer−polymer, protein−protein, and polymer−protein interaction via tracer sedimentation equilibrium, The Journal of Physical Chemistry B, 114 (2010) 10876-10880.

[89] P.M. Tessier, A.M. Lenhoff, S.I. Sandler, Rapid measurement of protein osmotic second virial coefficients by self-interaction chromatography, Biophysical Journal, 82 (2002) 1620-1631.

[90] S. Kanai, J. Liu, T.W. Patapoff, S.J. Shire, Reversible self-association of a concentrated monoclonal antibody solution mediated by Fab–Fab interaction that impacts solution viscosity, Journal of Pharmaceutical Sciences, 97 (2008) 4219-4227.

[91] C.O. Anderson, J.F.M. Niesen, H.W. Blanch, J.M. Prausnitz, Interactions of proteins in aqueous electrolyte solutions from fluorescence anisotropy and circular-dichroism measurements, Biophysical Chemistry, 84 (2000) 177-188.

[92] L. Jin, Y.-X. Yu, G.-H. Gao, A molecular-thermodynamic model for the interactions between globular proteins in aqueous solutions: Applications to bovine serum albumin (BSA), lysozyme, α-chymotrypsin, and immuno-gamma-globulins (IgG) solutions, Journal of Colloid and Interface Science, 304 (2006) 77-83.

[93] J. Wu, J.M. Prausnitz, Osmotic pressures of aqueous bovine serum albumin solutions at high ionic strength, Fluid Phase Equilibria, 155 (1999) 139-154.

[94] Y.U. Moon, R.A. Curtis, C.O. Anderson, H.W. Blanch, J.M. Prausnitz, Protein—protein interactions in aqueous ammonium sulfate solutions. lysozyme and bovine serum albumin (BSA), Journal of Solution Chemistry, 29 (2000) 699-718.

[95] T.W. Perkins, S. Saksena, R. van Reis, A dynamic film model for ultrafiltration, Journal of Membrane Science, 158 (1999) 243-256.

[96] Y.U. Moon, C.O. Anderson, H.W. Blanch, J.M. Prausnitz, Osmotic pressures and second virial coefficients for aqueous saline solutions of lysozyme, Fluid Phase Equilibria, 168 (2000) 229-239.

[97] C.A. Haynes, K. Tamura, H.R. Korfer, H.W. Blanch, J.M. Prausnitz, Thermodynamic properties of aqueous .alpha.-chymotrypsin solution from membrane osmometry measurements, The Journal of Physical Chemistry, 96 (1992) 905-912.

[98] M.A. Yousef, R. Datta, V.G.J. Rodgers, Free-solvent model of osmotic pressure revisited: application to concentrated IgG solution under physiological conditions, Journal of Colloid and Interface Science, 197 (1998) 108-118.

[99] B.A. Salinas, H.A. Sathish, S.M. Bishop, N. Harn, J.F. Carpenter, T.W. Randolph, Understanding and modulating opalescence and viscosity in a monoclonal antibody formulation, Journal of Pharmaceutical Sciences, 99 (2010) 82-93.

[100] M.F. Ebersold, A.L. Zydney, Use of protein charge ladders to study electrostatic interactions during protein ultrafiltration, Biotechnology and Bioengineering, 85 (2004) 166-176.

[101] P.M. Tessier, Fundamentals and applications of nanoparticle interactions and self-assembly, in: Chemical Engineering, University of Delaware, Newark, DE, 2003.

[102] R.G. Mortimer, Physical Chemistry, 3rd ed., Elsevier Academic Press, 2008.

[103] E. Binabaji, S. Rao, A.L. Zydney, Improved Method for Evaluating Protein–Protein Interactions by Self-Interaction Chromatography, Analytical Chemistry, (2013) (under review).

[104] J. Feder, T. Jøssang, E. Rosenqvist, Scaling behavior and cluster fractal dimension determined by light scattering from aggregating proteins, Physical Review Letters, 53 (1984) 1403-1406.

[105] T.M. Scherer, J. Liu, S.J. Shire, A.P. Minton, Intermolecular interactions of IgG1 monoclonal antibodies at high concentrations characterized by light scattering, The Journal of Physical Chemistry B, 114 (2010) 12948-12957.

[106] W.G. McMillan, J.E. Mayer, The Statistical Thermodynamics of Multicomponent Systems, Journal of Chemical Physics, 13 (1945) 276-305.

[107] P. DePhillips, A.M. Lenhoff, Pore size distributions of cation-exchange adsorbents determined by inverse size-exclusion chromatography, Journal of Chromatography A, 883 (2000) 39-54.

[108] W. Maeder, P. Lieby, A. Sebald, M. Spycher, R. Pedrussio, R. Bolli, Local tolerance and stability up to 24 months of a new 20% proline-stabilized polyclonal immunoglobulin for subcutaneous administration, Biologicals, 39 (2011) 43-49.

[109] H.W. Blanch, J.M. Prausnitz, R.A. Curtis, D. Bratko, Molecular thermodynamics and bioprocessing: from intracellular events to bioseparations, Fluid Phase Equilibria, 194–197 (2002) 31-41.

[110] V. Le Brun, W. Friess, S. Bassarab, S. Mühlau, P. Garidel, A critical evaluation of self-interaction chromatography as a predictive tool for the assessment of protein–protein interactions in protein formulation development: A case study of a therapeutic monoclonal antibody, European Journal of Pharmaceutics and Biopharmaceutics, 75 (2010) 16-25.

[111] D. Johnson, A. Parupudi, W.W. Wilson, L. DeLucas, High-throughput self-interaction chromatography: applications in protein formulation prediction, Pharm Res, 26 (2009) 296-305.

[112] T. Ahamed, M. Ottens, G.W.K. van Dedem, L.A.M. van der Wielen, Design of self-interaction chromatography as an analytical tool for predicting protein phase behavior, Journal of Chromatography A, 1089 (2005) 111-124.

[113] R.A. Lewus, P.A. Darcy, A.M. Lenhoff, S.I. Sandler, Interactions and phase behavior of a monoclonal antibody, Biotechnology Progress, 27 (2011) 280-289.

[114] P.M. Tessier, A.M. Lenhoff, Measurements of protein self-association as a guide to crystallization, Current Opinion in Biotechnology, 14 (2003) 512-516.

[115] P.M. Tessier, S.D. Vandrey, B.W. Berger, R. Pazhianur, S.I. Sandler, A.M. Lenhoff, Self-interaction chromatography: a novel screening method for rational protein crystallization, Acta Crystallographica Section D, 58 (2002) 1531-1535.

[116] A. George, W.W. Wilson, Predicting protein crystallization from a dilute solution property, Acta Crystallographica Section D, 50 (1994) 361-365.

[117] K.S. Deshpande, T. Ahamed, J.H. ter Horst, P.J. Jansens, L.A.M. van der Wielen, M. Ottens, The use of self-interaction chromatography in stable formulation and crystallization of proteins, Biotechnology Journal, 4 (2009) 1266-1277.

[118] C.A. Teske, H.W. Blanch, J.M. Prausnitz, Measurement of Lysozyme−Lysozyme Interactions with Quantitative Affinity Chromatography, Journal of Physical Chemistry B, 108 (2004) 7437-7444.

[119] T. Ahamed, B.N.A. Esteban, M. Ottens, G.W.K. van Dedem, L.A.M. van der Wielen, M.A.T. Bisschops, A. Lee, C. Pham, J. Thömmes, Phase behavior of an intact monoclonal antibody, Biophysical Journal, 93 (2007) 610-619.

[120] M. Muschol, F. Rosenberger, Interactions in undersaturated and supersaturated lysozyme solutions: Static and dynamic light scattering results, Journal of Chemical Physics, 103 (1995) 10424-10432.

[121] F. Bonneté, S. Finet, A. Tardieu, Second virial coefficient: variations with lysozyme crystallization conditions, Journal of Crystal Growth, 196 (1999) 403-414.

[122] R.A. Curtis, J. Ulrich, A. Montaser, J.M. Prausnitz, H.W. Blanch, Protein–protein interactions in concentrated electrolyte solutions, Biotechnology and Bioengineering, 79 (2002) 367-380.

[123] R.A. Curtis, J.M. Prausnitz, H.W. Blanch, Protein-protein and protein-salt interactions in aqueous protein solutions containing concentrated electrolytes, Biotechnology and Bioengineering, 57 (1998) 11-21.

[124] J. Bloustine, V. Berejnov, S. Fraden, Measurements of Protein-Protein Interactions by Size Exclusion Chromatography, Biophysical Journal, 85 (2003) 2619-2623.

[125] N. Rakel, K. Schleining, F. Dismer, J. Hubbuch, Self-interaction chromatography in pre-packed columns: A critical evaluation of self-interaction chromatography methodology to determine the second virial coefficient, Journal of Chromatography A, 1293 (2013) 75-84.

[126] T.C. Laurent, The interaction between polysaccharides and other macromolecules. 5. The solubility of proteins in the presence of dextran, Biochemical Journal, 89 (1963) 253-257.

[127] J.A. Rupley, G. Careri, Protein hydration and function, in: F.M.R.J.T.E. C.B. Anfinsen, S.E. David (Eds.) Advances in Protein Chemistry, Academic Press, 1991, pp. 37-172.

[128] J. Liu, M.D.H. Nguyen, J.D. Andya, S.J. Shire, Reversible self-association increases the viscosity of a concentrated monoclonal antibody in aqueous solution, Journal of Pharmaceutical Sciences, 94 (2005) 1928-1940.

[129] R. Chari, K. Jerath, A. Badkar, D. Kalonia, Long- and short-range electrostatic interactions affect the rheology of highly concentrated antibody solutions, Pharm Res, 26 (2009) 2607-2618.

[130] W.B. Russel, The dynamics of colloidal systems, The University of Wisconsin Press, Madison, 1987.

[131] Prasad S. Sarangapani, Steven D. Hudson, Kalman B. Migler, Jai A. Pathak, The limitations of an exclusively colloidal view of protein solution hydrodynamics and rheology, Biophysical Journal, 105 (2013) 2418-2426.

[132] S. Yadav, T.M. Laue, D.S. Kalonia, S.N. Singh, S.J. Shire, The influence of charge distribution on self-association and viscosity behavior of monoclonal antibody solutions, Molecular Pharmaceutics, 9 (2012) 791-802.

[133] M.M. Castellanos, J.A. Pathak, R.H. Colby, Both protein adsorption and aggregation contribute to shear yielding and viscosity increase in protein solutions, Soft Matter, 10 (2014) 122-131.

[134] Brian D. Connolly, C. Petry, S. Yadav, B. Demeule, N. Ciaccio, Jamie M.R. Moore, Steven J. Shire, Yatin R. Gokarn, Weak interactions govern the viscosity of
concentrated antibody solutions: high-throughput analysis using the diffusion interaction parameter, Biophysical Journal, 103 (2012) 69-78.

[135] P.D. Ross, A.P. Minton, Hard quasispherical model for the viscosity of hemoglobin solutions, Biochemical and Biophysical Research Communications, 76 (1977) 971-976.

[136] T. Arakawa, D. Ejima, K. Tsumoto, N. Obeyama, Y. Tanaka, Y. Kita, S.N. Timasheff, Suppression of protein interactions by arginine: A proposed mechanism of the arginine effects, Biophysical Chemistry, 127 (2007) 1-8.

[137] J. Siddique, S. Naqvi, Viscosity behavior of α-amino acids in acetate salt solutions at temperatures (303.15 to 323.15) K, Int J Thermophys, 33 (2012) 47-57.

[138] M. Heinen, F. Zanini, F. Roosen-Runge, D. Fedunova, F. Zhang, M. Hennig, T. Seydel, R. Schweins, M. Sztucki, M. Antalik, F. Schreiber, G. Nagele, Viscosity and diffusion: crowding and salt effects in protein solutions, Soft Matter, 8 (2012) 1404-1419.

[139] W. Blatt, A. Dravid, A. Michaels, L. Nelsen, Solute polarization and cake formation in membrane ultrafiltration: causes, consequences, and control techniques, in: J.E. Flinn (Ed.) Membrane Science and Technology, Plenum Press, New York, 1970, pp. 47-97.

[140] A. Subramani, S. Kim, E.M.V. Hoek, Pressure, flow, and concentration profiles in open and spacer-filled membrane channels, Journal of Membrane Science, 277 (2006) 7-17.

[141] A.R. Da Costa, A.G. Fane, D.E. Wiley, Spacer characterization and pressure drop modelling in spacer-filled channels for ultrafiltration, Journal of Membrane Science, 87 (1994) 79-98.

[142] J. Schwinge, D.E. Wiley, A.G. Fane, Novel spacer design improves observed flux, Journal of Membrane Science, 229 (2004) 53-61.

[143] Pellicon 3 Cassettes, in, EMD Millipore, http://www.emdmillipore.com/US/en/product/Pellicon-3-Cassettes,MM_NF-C9947.

VITA
Elaheh Binabaji

EDUCATION

Doctor of Philosophy, Chemical Engineering May 2015
The Pennsylvania State University, University Park, Pennsylvania

Bachelor of Science (honors), Chemical Engineering September 2008
Sharif University of Technology, Tehran, Iran

RESEARCH AND WORK EXPERIENCE

Graduate Research Assistant (PhD Dissertation) August 2009 – January 2015
Department of Chemical Engineering, The Pennsylvania State University (University Park, Pennsylvania), Advisor: Dr. Andrew L. Zydney

Internship at MedImmune, Gaithersburg, MD May 2013 – August 2013
Supervisor: Arick Brown

- Developed a flow-through polishing chromatography step using CHT resin for downstream processing
- Design of experiments (DOE) for optimizing process conditions

Graduate Teaching Assistant January 2013 – May 2013
Department of Chemical Engineering, The Pennsylvania State University (University Park, Pennsylvania), under supervision of Dr. Themis Matsoukas

JOURNAL PUBLICATIONS

- Binabaji E, Rao S, Ma J, Zydney A.L. "Ultrafiltration behavior of highly concentrated monoclonal antibody solutions: Effect of physicochemical and operating conditions" (in prep).
- Binabaji E, Rao S, Ma J, Zydney A.L. "Theoretical analysis of the ultrafiltration behavior of highly concentrated protein solutions" (in prep).
- Binabaji E, Ma J, Zydney A.L. "Intermolecular interactions and the viscosity of highly concentrated monoclonal antibody solutions" (in prep).
- Binabaji E, Rao S, Zydney A.L. 'The osmotic pressure of highly concentrated monoclonal antibody solutions: Effect of solution conditions," *Biotech Bioeng*., 111: 529-536 (2013).
- Binabaji E, Rao S, Zydney A.L. "An improved method for evaluating the dead volume and protein–protein interactions by self-interaction chromatography," *Anal. Chem.,* 85: 9101–9106 (2013).

AWARDS

- ICOM 2014 Travel Award from North American Membrane Society.
- Safety Improvement Award, The Pennsylvania State University, 2014.
- Sharif University of Technology Award for Excellence, 2008.